Direct numerical simulation of turbulent heat transfer to fluids at supercritical pressures

Nemati, Hassan

DOI
10.4233/uuid:b3fcb3a0-28b1-4335-a7a1-3fa1629e03d9

Publication date
2016

Document Version
Final published version

Citation (APA)
Nemati, H. (2016). *Direct numerical simulation of turbulent heat transfer to fluids at supercritical pressures*. [Dissertation (TU Delft), Delft University of Technology]. https://doi.org/10.4233/uuid:b3fcb3a0-28b1-4335-a7a1-3fa1629e03d9

DIRECT NUMERICAL SIMULATION OF TURBULENT HEAT TRANSFER TO FLUIDS AT SUPERCRITICAL PRESSURES

Proefschrift

ter verkrijging van de graad van doctor
aan de Technische Universiteit Delft,
op gezag van de Rector Magnificus prof. ir. K.C.A.M. Luyben,
voorzitter van het College voor Promoties,
in het openbaar te verdedigen op donderdag 17 november 2016 om 10:00 uur.

door

Hassan Nemati

Master of Science in Mechanical Engineering,
Mazandaran University, Iran
geboren te Bojnord, Iran

Dit proefschrift is goedgekeurd door de promotor:

Prof. dr. ir. B. J. Boersma

en de copromotor:

Dipl.-Ing. Dr.techn. R. Pecnik

Samenstelling promotiecommissie:

Rector Magnificus	voorzitter
Prof. dr. ir. B.J. Boersma	Technische Universiteit Delft, promotor
Dipl.-Ing. Dr.techn. R. Pecnik	Technische Universiteit Delft, copromotor

Onafhankelijke leden:

Prof. Dr.-Ing. S. Hickel	Technische Universiteit Delft
Prof. Dr.-Ing. E. Laurien	Universität Stuttgart
Prof. dr. D.J.E.M. Roekaerts	Technische Universiteit Delft
Prof. dr. ir. T.H. van der Meer	Universiteit Twente
Dr. ir. J.A. van Oijen	Technische Universiteit Eindhoven

ISBN 978-94-6299-467-6

---

[1] Author e-mail address: hasan.nemati1985@gmail.com

Dedicated

to

the spirit of my father Alireza,

as well as my mother Senobar,

my father in law Ali,

my mother in law Golbas, and

my lovely wife Ameneh.

Contents

Summary

Renewable energy sources such as geothermal heat and solar radiation with low and medium-temperature solar collectors are referred to as low-grade heat sources. This is due to the fact that the maximum possible increase of temperature in these systems is much lower than in fossil fuel combustion chambers. When converting these low-grade thermal sources to power, the conventional power generation methods do not show a satisfactory performance, owing to their low thermal efficiency at low temperature ranges. As a consequence, different thermodynamic cycles have been proposed, among which the supercritical Rankine cycle has been accepted as a promising technology for future renewable energy systems. The heat addition process in such a supercritical Rankine cycle does not involve the working fluid crossing the two-phase region, thereby minimising exergy losses. This is one of the major advantages of a supercritical Rankine cycles.

The most important characteristic of fluids at supercritical pressures is the non-ideal behaviour of thermophysical properties. Due to these features, the dynamics of heated turbulent flows at supercritical pressures are much more complex than single-phase flows at subcritical pressures. In fact, the extreme thermophysical property variations of fluids close to the critical point make the momentum and internal energy highly coupled and alter the conventional behaviour of mean and turbulent motions.

This thesis presents the original results of a numerical investigation of heated turbulent flows at supercritical pressures, aiming at investigating the effects of large variations of thermophysical properties on turbulence statistics, studying the influence of buoyancy on heat transfer enhancement and deterioration, and understanding the impacts of fluctuating/non-fluctuating wall temperature on turbulence statistics.

The core of the results consists of two main parts, which are summarised as follows. The first part studies the contribution of significant property variations on the mean flow. As compared to ideal gas heat transfer, additional terms appear in the mean flow governing equations. These terms can significantly affect the energy balance, because they modify the averaged wall heat flux and the enthalpy diffusion close to the pipe wall. Furthermore, the averaged thermophysical properties deviate significantly from those evaluated using the mean temperature or enthalpy. This is due to an averaging artefact called Jensen's inequality, caused by enthalpy fluctuations and the non-linear dependence of thermophysical properties on the enthalpy. Turbulence statistics for forced convection and mixed convection cases with upward/downward flow are presented. Turbulence statistics are reported to highlight the effects on the observed wall temperature distribution and related heat transfer mechanisms.

In the second part, two different thermal wall boundary conditions are studied: one that does permit temperature fluctuations at the wall and one that does not (equivalent to cases where the thermal effusivity ratio approaches infinity and zero, respectively). Unlike for turbulent flows with constant thermophysical properties with Prandtl numbers above unity, where the effusivity ratio has a negligible influence on heat transfer, fluids at supercritical pressures show a strong dependency on the effusivity ratio. A reduction of 7% in the Nusselt number is observed when the temperature fluctuations at the wall are suppressed. On the other hand, if temperature fluctuations are permitted, large property variations are induced which cause an increase of wall-normal velocity fluctuations very close to the wall. This results in an increased overall heat flux and skin friction.

Samenvatting

Onder de hernieuwbare energiebronnen worden die met thermische bronnen, zoals geothermische energiecentrales en lage en gemiddelde temperatuur zonnecollectoren, laagwaardige warmtebronnen genoemd, aangezien het resulterende temperatuurbereik lager is in vergelijking met die van de verbranding van fossiele brandstoffen. Bij omzetting van deze laagwaardige thermische bronnen naar elektrisch vermogen vertonen de conventionele elektriciteitsopwekkingsmethoden geen bevredigende prestaties vanwege hun lage thermische efficiëntie bij lage temperaturen. Als gevolg daarvan zijn verschillende thermodynamische cycli voorgesteld, waarvan de superkritische Rankine cycli zijn geaccepteerd als veelbelovende technologie voor de toekomst van hernieuwbare energiebronnen. In het warmte toevoegingsproces van een dergelijke superkritische Rankine cyclus doorkruist het werkfluïdum de tweefase regio niet, waardoor het exergieverlies geminimaliseerd wordt. Dit is een van de belangrijkste voordelen van superkritische Rankine cycli.

Het belangrijkste kenmerk van fluïda bij superkritische druk is het non-ideale gedrag van de thermofysische eigenschappen. Door deze afwijkende eigenschappen zijn de dynamica van verwarmde turbulente stromingen bij superkritische druk veel complexer dan die van eenfase stromingen bij subkritische druk. Werkelijk, koppelt de extreme variatie in thermofysische eigenschappen van fluïda dichtbij het kritische punt de impuls sterk met de interne energie en verandert het conventionele gedrag van gemiddelde en turbulente bewegingen.

Dit proefschrift presenteert de originele resultaten van een numeriek onderzoek van verwarmde turbulente stromingen bij superkritische druk, met de focus op het onderzoeken van de effecten van grote schommelingen van thermofysische eigenschappen op turbulentiestatistieken, het bestuderen van de invloed van de drijfkracht op de verbetering en verslechtering van de warmteoverdracht en het begrijpen van de impact van fluctuerende of non-fluctuerende wandtemperatuur op turbulentiestatistieken.

De kern van de resultaten bestaat uit twee belangrijke delen, welke als volgt zijn samengevat. Het eerste deel bestudeert de bijdrage van significante schommelingen in de eigenschappen op de gemiddelde stroming. In vergelijking met de warmteoverdracht van ideale gassen verschijnen er extra termen in de vergelijkingen die gelden voor de gemiddelde stroming. Deze termen kunnen een significant effect op de energiebalans hebben, omdat zij de gemiddelde warmteflux over de wand en de enthalpiediffusie dichtbij de pijpwand veranderen. Bovendien wijken de gemiddelde thermofysiche eigenschappen aanzienlijk af van die geëvalueerd met de gemiddelde temperatuur of enthalpie. Dit komt door een middelingsartefact, de ongelijkheid van Jensen genaamd, dat wordt veroorzaakt door enthalpiefluctuaties en de non-lineaire afhankelijkheid van de thermofysiche eigenschappen op de enthalpie. Turbulentiestatistieken worden gepresenteerd voor geforceerde convectie en gemixte convectie met opwaartse/neerwaartse stroming. Turbulentiestatistieken worden gerapporteerd om het

effect op de geobserveerde distributie van de wandtemperatuur en het gerelateerde warmtetransportmechanisme te benadrukken.

In het tweede deel worden twee verschillende thermische wand randvoorwaarden bestudeerd. Een staat temperatuurfluctuaties toe en een staat geen temperatuurfluctuaties toe bij de wand (gelijk aan gevallen waar de ratio van de warmtepenetratiecoëfficiënten respectievelijk oneindig en nul nadert). Anders dan voor turbulente stromen met constante thermofysische eigenschappen en Prandtlgetallen groter dan een, waar de ratio van de warmtepenetratiecoëfficiënten een verwaarloosbare invloed heeft op de warmteoverdracht, tonen superkritische fluïda een grote afhankelijkheid van de ratio van de warmtepenetratiecoëfficiënten. Een verlaging van 7% van het Nusseltgetal is geobserveerd wanneer de temperatuurfluctuaties aan de wand worden onderdrukt. Anderzijds, als temperatuurfluctuaties zijn toegestaan, leidt dat tot grote schommelingen in eigenschappen, die heel dicht bij de wand een verhoging van de snelheidsfluctuaties normaal aan de wand veroorzaken en daarmee een verhoogde totale warmteflux en wrijving.

1

Introduction

Part of the contents of this chapter appeared in:

Nemati, H., Patel, A., Boersma, B.J. & Pecnik, R.
Int. J. Heat Mass Tran., **83**, 741-752 (2015)

1.1 Global warming and sustainable development

Global energy consumption has continuously increased over the last few decades in step with population growth and industrial development. Demand for energy is predicted to rise by at least one-third to 2040 (OECD, 2015*b*)[1], as developing countries like India, China and countries in Africa, the Middle East and South-east Asia seek to stoke up their rapid economic growth. The majority of global energy is supplied by fossil fuels (FFs), such as coal, oil and gas (33% oil, 30% coal and 24% natural gas in 2013 (British Petroleum (BP), 2014)) that formed millions of years ago from carbon-contain remains of dead flora and fauna. However, these are not renewable sources that will last forever. The report on world energy outlook by the International Energy Agency (IEA) estimates that Indian economy will grow to reach more than five-times its current size by 2040 and energy consumption will double to 1900 million tonnes of oil equivalent (mtoe) (OECD, 2015*a*). Although the increase in energy consumption is slower than the domestic economic growth, it is around one-quarter of the total increase in global energy consumption till 2040.

Over-consumption of fossil fuels can lead to catastrophic impacts on the environment. The biggest global threat to the environment in the 21^{st} century is global warming. Ice-melting at the poles (both Greenland and West Antarctica to the extent of around 350 billion tons each year (Shepherd *et al.*, 2012; Joughin *et al.*, 2008; Das *et al.*, 2008)), long-lasting heat waves (Kyselỳ, 2010; Meehl & Tebaldi, 2004), increasing wildfire, sea level rise (11.1 mm worldwide between 1992-2011) (Hansen *et al.*, 2005; Shepherd *et al.*, 2012; Rahmstorf *et al.*, 2007) and increase in extreme weather events are a few inevitable examples of the effects caused by anthropogenic greenhouse gas emissions into the atmosphere and rising global temperatures. For hundreds of years, the mean temperature of the earth surface increased at a rate of a few tenths of a degree per century (Houghton *et al.*, 2001). Due to the advent of the industrial revolution in the eighteenth century, the greenhouse effect was enhanced by anthropogenic emissions from fossil fuel combustion, thus led to thousands of times larger increase in mean earth surface temperature. A continuous increase of 0.2°C per decade (total increase of 0.8°C) has been recorded for the last four decades (Alexander *et al.*, 2013).

In order to effectively prevent future catastrophes due to global warming, a significant amount of political and scholarly attention is necessary to strengthen the cooperation between international research communities. The first international attempt to understand global warming was organised by the United Nations (UN) in 1992 at Rio de Janeiro, known as Rio Earth Summit. The agreement called "Climate Change Convention", which set out a framework to stabilise the concentrations of greenhouse gases in the atmosphere in the long-term at around today's levels. The international collaboration has been strengthened to coordinate national and institutional efforts so that research resources may be used with greater efficiency to obtain better results; e.g. the World Meteorological Organization (WMO), the United Nations Environment Programme (UNEP), and the United Nations Education, Scientific and Cultural

---

[1] Organization for Economic Co-operation and Development

Organization (UNESCO).

The commonly presented solution by different international organisations and research institutes is to focus on global energy transformation and emphasis on changing the major part of the power generation capacity from fossil fuels to renewable and carbon-free alternatives such as wind power, solar energy, hydropower, wave and tidal power, biomass and geothermal energy. Based on the report by Renewable Energy Policy Network for the 21^{st} Century (REN21), renewable energy covers 19% of global energy consumption and 22% of generated electricity in 2012 and 2013 (Sawin *et al.*, 2014). Norway is the leader in renewable energy production and over 99% of electricity generation is covered by hydropower plants, while it also has a significant potential in offshore wind and wave power. Many countries have put substantial financial supports to reach 100% renewable energy in the future. For example, the Danish government has targeted to produce electricity and energy needed for transportation to be covered 100% by renewables by 2050 (Mathiesen *et al.*, 2015).

1.2 Thermal energy

Renewable thermal energy sources including geothermal and solar thermal, are potentially auspicious energy sources capable of meeting the increasing world electricity demand. However, the low and moderate temperature heat, also called low-grade heat, from these sources cannot be converted efficiently to electrical power by conventional steam cycles. In this context, different thermodynamic cycles have been proposed, among which the supercritical Rankine cycles (Chen *et al.*, 2006; Chen, 2006; Zhang *et al.*, 2007*b*, 2006, 2007*a*) have been accepted as a promising technology. The idea of using supercritical Rankine cycles was drawn from the subcritical organic Rankine cycles (figure 1.1), which are usually used to convert waste heat from a gas turbine or other low-grade heat sources into useful electrical power (Hung *et al.*, 1997; Hung, 2001). The main drawback of subcritical organic Rankine cycle is the constant temperature process during heat addition which is not efficient for low-grade heat sources (Chen *et al.*, 2010). The major difference between subcritical organic Rankine cycles and supercritical Rankine cycles is the heat addition. For subcritical organic Rankine cycles, the working fluid experiences a constant temperature phase-change from liquid to gas phase, while in supercritical Rankine cycles the fluid does not cross the two-phase region, which results in less exergy loss (see figure 1.2).

Among the working fluids for supercritical power cycles, carbon dioxide CO_2 is one of the favourable fluids, because of its low critical pressure and temperature, and also because it is classified as a non-flammable and non-toxic fluid. In addition supercritical CO_2 power cycles offer a number of benefits over conventional power cycles including, compact design, lower capital cost and lower operation and maintenance costs.

However, fluids at supercritical pressures have a non-ideal behaviour of their thermophysical properties (will be discussed in the next chapter). Thermodynamic properties like density, isobaric heat capacity and speed of sound and transport properties such as viscosity and thermal conductivity show abrupt but continuous changes–as

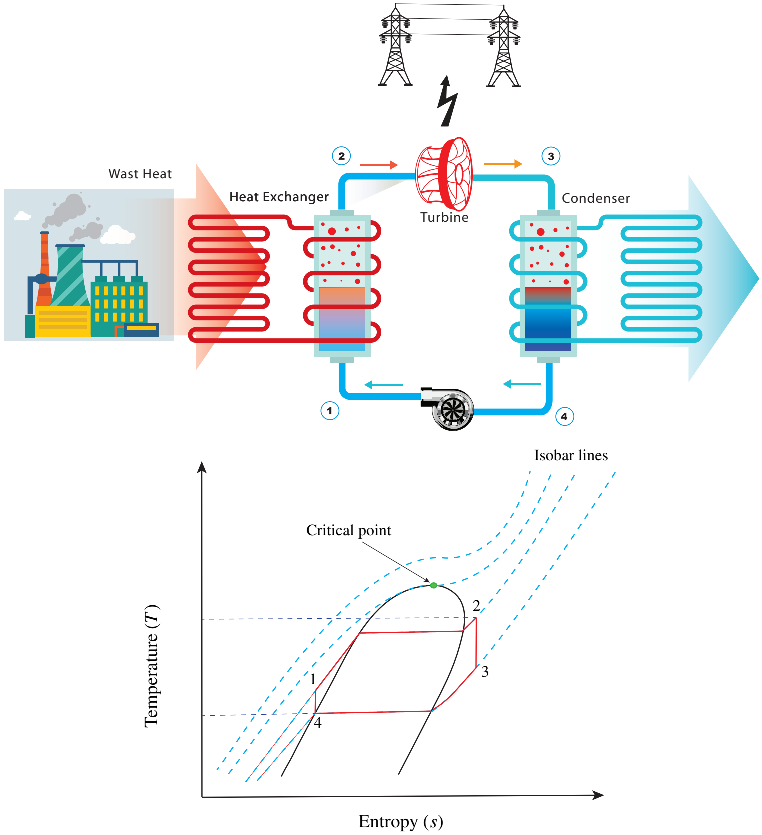

Figure 1.1: A schema of typical subcritical organic Rankine cycle.

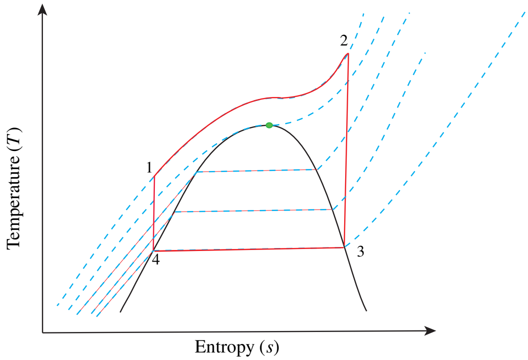

Figure 1.2: A schema of supercritical Rankine cycles.

Table 1.1: Critical properties of various substances (Lemmon *et al.*, 2002).

substance	P_{cr} (bar)	T_{cr} (K)	ρ_{cr} (kg/m^3)
CO_2	73.77	304.13	466.6
H_2O	220.65	647.01	322.4
CH_4	45.99	190.57	161.4
NH_3	113.33	405.40	193.7
O_2	50.43	154.58	460.6
H_2	12.97	33.15	29.6

opposed to phase change–of thermophysical changes in a small range of temperatures. Figure 1.3 shows the contour plots of different thermophysical properties for CO_2 (see table 1.1 for critical properties) based on NIST REFPROP database (Lemmon *et al.*, 2002). These changes become more extreme and occur in a smaller temperature range, when approaching the critical point; e.g. speed of sound becomes zero (Smith Jr *et al.*, 2013) and isobaric heat capacity diverges to infinity at the critical point. The pseudo-critical temperature T_{pc} is the location where the heat capacity attains its peak at constant pressure.

Due to these unusual features, the dynamics of heated turbulent flows at supercritical pressures are much more complex than those of single-phase flows at subcritical regions and do not comply with the ideal gas model. In fact, the extreme thermophysical property variations of fluids close to the critical point make the momentum and internal energy highly coupled and alter the conventional behaviour of mean and turbulent motions. These features can also be observed in heat transfer in subcritical regions, but they manifest themselves more dynamically at supercritical pressures. Research in the field of turbulent heat transfer to supercritical fluids has been active since the 1950's to increase the thermal efficiency of power plants operating at supercritical pressures. In the 1990's, by advancement in modern nuclear power plants, the interest in turbulent heat transfer to supercritical fluids research regained momentum due to their potential to enhance the thermal efficiency (Pioro *et al.*, 2004*b*). Several review papers, experimental and numerical studies have been published since then, to understand heat transfer to fluids at supercritical pressures to understand the influence of large thermophysical property variations on turbulent heat transfer mechanisms.

1.3 Literature review

The first review, to our knowledge, on heat transfer to supercritical fluids has been published by Petukhov (1968). He did a comparative study between available

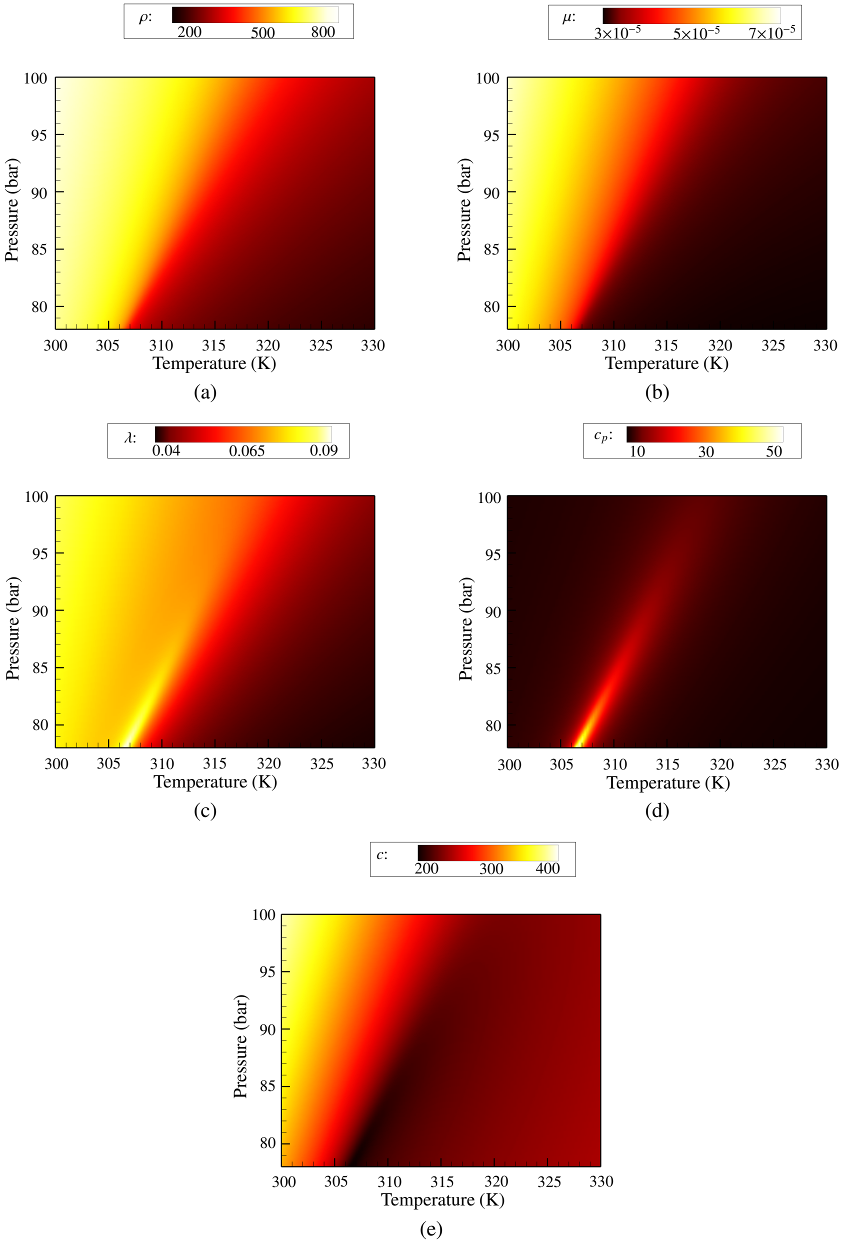

Figure 1.3: Variation of thermophysical properties of CO_2 with pressure and temperature (Lemmon *et al.*, 2002). (a) Density ρ, (b) dynamic viscosity μ, (c) thermal conductivity λ, (d) isobaric heat capacity c_p and (e) speed of sound c.

experimental data of sub- and supercritical pressure flows (water and CO_2) and some available correlations for skin friction and Nusselt number. He observed a considerable disagreement between numerical and experimental results, particularly in cases with substantial changes in thermophysical properties (supercritical fluid) and reported that it may be attributed to inaccuracies in estimating the effect of the thermophysical property variations on the correlations. In the same year, Hall *et al.* (1968) conducted a critical review of the literature on this subject, mainly those that were carried out between 1963 and 1966. They performed a comparative study of available empirical correlation coefficients of heat transfer coefficient (Miropolskii & Shitsman, 1957; Petukhov *et al.*, 1961; Bishop *et al.*, 1964; Swenson *et al.*, 1965) for a case of supercritical water at pressure 254 bar (see table 1.1 for critical properties of water). They showed that available empirical correlation coefficients are unable to predict heat transfer coefficient above the critical pressure. Accordingly, a suggestions were give to properly include effects of buoyancy and strong non-uniformity in thermophysical properties by taking into account detailed measurements. Another review paper was published by Polyakov (1991). He provided information on the results of investigations conducted in the 1970's and 1980's and attempted to address the problems mentioned in Petukhov (1968) and Hall *et al.* (1968) via solutions of Navier-Stokes equations using turbulence modelling. More recently, an increasing interest in heat transfer to fluids at supercritical pressures has resulted in several publications, which have been summarised in the following review articles: Pitla *et al.* (1998); Kirillov (2000); Pioro *et al.* (2004*b*,*a*); Duffey & Pioro (2005) and more recently by Yoo (2013); Shen & Zhang (2013).

1.3.1 Experimental studies

One of the first experiments was carried out by Shitsman (1963) on upward flowing heated supercritical water with low flow rates and different wall heat fluxes. For a small wall heat flux, a localised decrease in wall temperature was observed (heat transfer enhancement). He noticed that with increasing heat flux, a deterioration in heat transfer occurs that is followed by recovery further downstream. During the experiment, pressure pulsations were observed when the bulk temperature approached the pseudo-critical temperature T_{pc}. A similar experiment was performed by Yamagata *et al.* (1972) to investigate a larger range of wall heat flux and higher mass flow rates for supercritical water. They found that the heat transfer coefficient reaches a local maximum when the bulk temperature approaches the pseudo-critical temperature. They also observed that the peak reduces with increasing heat flux.

A comprehensive experimental study on heat transfer to water at supercritical pressures was performed by Ackerman (1970) for a wide range of pressure, mass flux, heat flux, and buoyancy forces. Based on this work, the author reported that for some cases, an unpredictable heat transfer deterioration occurs when the pseudo-critical temperature is located in the thermal boundary layer between the heated surface and the bulk fluid. He explained that with the occurrence of a pseudo-boiling phenomenon (abrupt reduction in density) in the near wall region results in a sudden deterioration of the heat transfer coefficient. However, the validity of this reasoning was not supported by many other studies (see (Yoo, 2013)). Hall and Jackson performed extensive experimental and theoretical studies on turbulent heat transfer at supercritical pressures to explain the phenomenon of heat transfer and deterioration. By comparing experimental results from horizontal flows with those for upward/downward flows under the same conditions, they proposed that the effects of buoyancy and flow acceleration due to thermal expansion is more justifiable (Hall & Jackson, 1969; Hall, 1971; Jackson & Hall, 1979*a*,*b*; Jackson *et al.*, 2003). The theoretical analysis exhibited that the flow acceleration (due to thermal expansion) only results in deterioration (independent of flow direction). Regarding the buoyancy effects, it was found that it could cause both, heat transfer deterioration and recovery in upward flows (depending on the magnitude of buoyancy), while for downward flows it only promotes or enhances turbulent heat transfer. Later, Kurganov & Kaptilnyi (1993) conducted some experiments with CO_2 at supercritical pressure to examine the effects of buoyancy on flow structure, heat transfer and drag force at high Reynolds numbers. They observed the deformation of the stream-wise velocity to an M-shaped profile, due to high buoyancy forces in upward flows, which favours the recovery of heat transfer. Experimental studies on this subject have been active during last decade to further develop more accurate and universal heat transfer correlations (Jiang *et al.*, 2004; Kim *et al.*, 2006, 2007; Song *et al.*, 2008; Licht *et al.*, 2008; Kim *et al.*, 2008*a*; Bae & Kim, 2009; Licht *et al.*, 2009; Bae *et al.*, 2010).

1.3.2 Numerical studies

Besides the experiments, a few computational studies on turbulent heat transfer to supercritical fluids have been carried out by different researchers in the past; i.e., in the early days, only the Reynolds Averaged Navier-Stokes (RANS) calculations were possible. Koshizuka *et al.* (1995) performed a numerical analysis to study heat transfer deterioration using a $k-\epsilon$ turbulence model and compared the results with experimental data of Yamagata *et al.* (1972). Despite a good qualitative agreement with experimental data, the model failed to predict deterioration. He *et al.* (2005) compared the performance of the Launder and Sharma $k-\epsilon$ turbulence model to predict convective heat transfer to CO_2 at supercritical pressures in a vertical mini tube (Jiang *et al.*, 2004). The agreement regarding the level of accuracy was very poor. He *et al.* (2008*b*) examined the performance of the v^2-f (Behnia *et al.*, 1998) and the Abe-Kondoh-Nagano (AKN) (Abe *et al.*, 1994) $k-\epsilon$ turbulence models by comparing their results with experimental data of supercritical CO_2 in heated upward and downward flows in tubes (Fewster, 1976). Both models were able to show a qualitative agreement of heat transfer deterioration. However, significant inconsistency was observed in wall temperature distributions. Several other turbulence models have been tested by different researchers, e.g. (Wen & Gu, 2010; Kim *et al.*, 2008*b*; Jiang *et al.*, 2008; Sharabi & Ambrosini, 2009; Sharabi *et al.*, 2008), to find a universal model to predict the important features of turbulent heat transfer at supercritical pressures. It can be concluded that available turbulence models are inadequate as a means of accurately predicting heat transfer to supercritical flows. Hence, numerical research in this field has drawn considerable attention worldwide.

Fortunately, developments in computing power have allowed Computational Fluid Dynamics (CFD) to use Large-eddy Simulation (LES) and Direct Numerical Simulation (DNS) that permit experiments to be performed numerically. DNS provides an accurate quantitative measurement of flow and thermal structures. To the best of the authors knowledge, the first DNS was carried out by Bae *et al.* (2005), to investigate turbulent heat transfer to CO_2 at supercritical pressure in a developing heated pipe at an inlet Reynolds number Re_{0b}=5400. The inlet and wall thermal boundary condition were applied such that the pseudo-critical temperature (where large variations in thermophysical properties occur) is located between the wall and pipe centerline. Various buoyancy conditions in both upward and downward flows were investigated to understand the physical mechanism behind heat transfer deterioration and recovery. The analysis of mean quantities, Reynolds stresses, turbulent heat fluxes, and their transport equations indicates that they are directly/indirectly affected by their respective buoyancy production. The deformation of the mean velocity distribution into an M-shaped profile was observed in upward flows with moderate and high buoyancy, which was identified as the onset of heat transfer recovery. Unlike in upward flows, only enhancement of turbulence was observed in downward flows. A good qualitative agreement was found with experimental data (very large Reynolds numbers) and the observations made by Hall (1971). A similar DNS study was done by Bae *et al.* (2008) in a vertical annulus (inner-pipe heating) where they made a comparison with flows with constant property fluids. Recently Ničeno & Sharabi (2013) performed an LES to study the details of turbulent heat transfer for flows of supercritical water in a tube and compared the results with experimental data (relatively high Reynolds number) from Pis'menny *et al.* (2006). The simulations were run on a computer program called PSI-BOIL which was developed for channel geometry. Instead of solving the governing equations in a cylindrical domain, a channel flow between parallel walls with the same hydraulic diameter was considered. The wall temperature showed reasonable agreement with experiments. However, the simulation was not able to reproduce the peak values of wall temperature in the deterioration-recovery region for the upward flow.

1.4 Heat transfer mechanisms in variable property flows

Given the review above, the influencing factors on heat transfer to fluids at supercritical pressures can be summarised. We start by considering heat transfer mechanisms observed for flows with variable properties. In a heated flow, the fluid density ρ decreases, whereby the reduction depends on the thermodynamic state of the fluid. For instance, at sub-critical states the density changes are small and gradual, whereas at supercritical states the changes in density are sharp and large. The decrease in density causes two effects: (i) buoyancy and (ii) flow acceleration due to thermal expansion. Additionally, the variations of thermophysical properties, such as specific heat c_p, thermal conductivity λ and viscosity μ also affect the heat transfer mechanism. These three effects are discussed in more detail below. Although, the main focus will be on heat transfer to supercritical turbulent flows, attention will also be drawn to similar effects in laminar and sub-critical flows wherever necessary.

1.4.1 Influence of variation in specific heat c_p, thermal conductivity λ and viscosity μ

In 1972, Yamagata *et al.* (1972) experimentally investigated the effect of thermophysical property variations on heat transfer to supercritical water in heated tube geometries. For low heat to mass flux ratios, where buoyancy and thermal expansion effects are small, they observed an enhancement in heat transfer, which can be explained using the empirically obtained Dittus-Boelter correlation (Bergman *et al.*, 2011). The heat transfer coefficient H can then be expressed as a function of thermophysical properties

$$H \propto \lambda_b^{0.6} \mu_b^{-0.4} c_{p,b}^{0.4}. \tag{1.1}$$

The subscript $_b$ represents the bulk quantities. Given the thermophysical property variations–for example, CO_2 at a constant pressure line (see figure 1.3)–it can be seen that the increase in c_p and the decrease in μ are dominant as compared to the decrease in λ. This is causing the heat transfer coefficient to increase. A sound physical explanation is given by Licht *et al.* (2008) to explain the results obtained by Yamagata *et al.* (1972). They state that at low heat flux values the energy input is not large enough to overcome the large values of specific heat close to the wall and thus a low wall to bulk temperature gradient is obtained. By increasing the wall heat flux, the energy input will be large enough to overcome the large specific heat values at the wall, causing an increased temperature gradient at the wall and more localised region of large c_p away from the wall. This results in a higher wall to the bulk temperature gradient and hence impairs the heat transfer (Licht *et al.*, 2008).

1.4.2 Influence of flow acceleration

Flow acceleration is caused due to thermal expansion, and in upward flows also due to buoyancy. However, the net acceleration of buoyancy on the total cross-section is zero, whereas thermal expansion causes net acceleration because the bulk velocity increases. In laminar flows the thermal expansion, and in upward flows also buoyancy, increases convective heat transfer because of flow acceleration. In downward flows, the heat transfer is deteriorated when deceleration due to buoyancy is larger than the acceleration due to thermal expansion. In turbulent convection the effects are opposite (Kim *et al.*, 2008*b*). Although flow acceleration increases the velocity close to the wall, it reduces turbulence production. The wall normal velocity gradient in the viscous dominant region increases, where it has a small influence on the turbulence production. On the other hand, the velocity gradient further away from the wall decreases, thus decreasing the turbulence production. Similar observations were made by Kline *et al.* (1967), where for accelerating turbulent boundary layers, they observed a reduction in bursting frequency which is the primary mechanism for turbulence production. Since mixing dominates the heat transfer mechanism in turbulent flows, the heat transfer effectiveness decreases. In downward flows with buoyancy, turbulence production increases, when deceleration due to buoyancy is larger than the acceleration due to thermal expansion, thereby enhancing heat transfer.

1.4.3 Influence of buoyancy

The effect of buoyancy plays an interesting role regarding heat transfer recovery (after deterioration) for turbulent flows and usually dominates the flow behaviour. Buoyancy causing local flow acceleration or deceleration, depending on flow direction, is sometimes referred to as the external or indirect effect. However, it also has another role called structural or direct effect (Petukhov *et al.*, 1988), and will be discussed hereafter.

1.4.3.1 External effect

The external - or sometimes referred to as indirect - effect is essentially the response of turbulence to distortions of the mean velocity profile caused by local flow acceleration or deceleration. In upward flows, buoyancy aids the flow in the sense that due to density decrease (in the case of heating) the gravity force is lower close to the wall. This increases the velocity close to the wall, causing local flow acceleration. In downward flows, buoyancy opposes the flow, causing the fluid close to the wall to decelerate. Buoyancy is a result of a radial density gradient and does not change the bulk velocity. Therefore, the local flow acceleration close to the wall is compensated by a velocity reduction in the core to satisfy the integral mass flux balance. The higher the buoyancy, the higher the velocity decreases in the core, such that an 'M-shaped' velocity profile can occur. In contrast to this, flow acceleration due to thermal expansion close to the wall is limited by the thermal expansion coefficient, and the velocity reduction (to satisfy mass flux balance) in the core is counteracted by the increase of the bulk velocity.

1.4.3.2 Structural effect

The structural - or sometimes referred to as direct effect - refers to turbulence production or destruction due to density fluctuations. It is quantified by the buoyancy production term in the turbulent kinetic energy equation. Any destabilising phenomena will act as a source of turbulence. For example, when a fluid inside a horizontal channel is heated from below and cooled from above, an unstable stratification is obtained. A stable stratification is obtained when the heating and cooling walls are interchanged.

Depending on the stability of the stratification, the buoyant turbulent production can act as a source (positive) or as a sink (negative). The buoyant turbulent production term is given as $B_k = \mp Ri_{0z}\overline{\rho' w'}$, where ρ' is the density fluctuation, w' is the stream-wise velocity fluctuation and Ri_{0z} is reference Richardson number. If in a stably stratified flow ($\partial\rho/\partial z < 0$) a fluid particle is displaced from a lower to a higher position (due to velocity fluctuations), where the density of the surrounding fluid is lower, then the buoyancy force will push the higher density particle back to its original position. This damps the turbulent fluctuations and the buoyancy production acts as a sink for stably stratified flows. In an unstably stratified flow ($\partial\rho/\partial z > 0$), the opposite occurs, thus enhancing the vertical turbulent fluctuations. The buoyancy production term acts as a source for unstably stratified flows.

Note, downward heated flows are always unstably stratified (density gradient $\partial\rho/\partial z$ and gravity are opposed), while upward heated flows can be both stably and unstably stratified. After turbulence recovery, the radial density distribution strongly changes in stream-wise direction. This can cause a stream-wise density gradient, such that an unstably stratified flow occurs. Therefore, both the external and the structural effects of buoyancy contribute to the recovery process in upward flows.

1.5 Motivation

From the experimental and computational studies reviewed above, it is clear that turbulent heat transfer at supercritical pressures will play an important role in the design of future energy systems. Therefore, the ability to reliably predict heat transfer to supercritical fluids is of utmost importance in the design of such systems. In contrast to experiments, which pose limitations in terms of the accuracy in measuring turbulence in supercritical fluids, DNS is capable of providing a full physical understanding turbulent flows. The advent of supercomputers and high performance computing numerical methods has facilitated this process by enabling us to achieve the high resolution necessary for analysing all the scales present in turbulent flows. Thus, DNS also overcomes the constraints imposed by the modeling assumptions present in empirical turbulence models. The work documented in this thesis aims to use DNS to study the effects of the peculiar behaviour of thermophysical properties on turbulent heat transfer at supercritical pressures. Moreover, a detailed discussion on the effects of buoyancy and thermal wall boundary conditions will be given.

1.6 Thesis Outline

This thesis consists of 5 chapters. A detailed description of the numerical scheme and the flow domain used in the simulation is given in **chapter 2**. It presents the low-Mach number approximation of the Navier-Stokes equations in cylindrical coordinates. Afterwards, the numerical details such as spatial and temporal discretization and boundary conditions are given. Next, different equations of state to compute the thermodynamic properties, and equations to compute the transport properties at supercritical pressures will be reviewed. Finally, a short description on the implementation of the thermophysical properties of CO_2 is presented.

The objective of **chapter 3** is to further investigate the turbulent heat transfer mechanisms to supercritical fluids in pipe flows using detailed turbulent flow statistics. The turbulent statistics, such as turbulent shear stress, radial turbulent heat flux, turbulent kinetic energy and its production rates (shear and buoyant production) for different flow configurations are presented. Additionally, the interaction of the highly non-linear thermophysical property variations (density ρ, viscosity μ, thermal conductivity λ and isobaric heat capacity c_p) with turbulent fluctuations in the flow field will be discussed.

In **chapter 4** the influence of fluctuating wall temperature and nonfluctuating wall temperature on heat transfer to fluids with large property variations and high Prandtl numbers is investigated.

Chapter 5 presents the summary of the investigated supercritical cases in chapters 3 and 4.

2

Governing equations and computational details

Part of the contents of this chapter appeared in:

Nemati, H., Patel, A., Boersma, B.J. & Pecnik, R.
Int. J. Heat Mass Tran., **83**, 741-752 (2015)

2.1 Introduction

In fluid dynamics, the full compressible Navier-Stokes equations are considered to be the complete mathematical description of the fluid motion. These equations represent the conservation of mass, momentum, and energy. They are closed with the equation of state (EOS), which prescribes the density ρ as a function of pressure P and temperature T. One of the major difficulty in numerical simulations of full compressible Navier-Stokes is linked to the severe limitation of the time step due to the large value of the sound velocity (small values of Mach number M); i.e. the sound waves travels much faster than the fluid particles when $M \ll 1$. Two approaches have been developed to alleviate the limitation on the time step: 1- the low-Mach number approximation of the Navier-Stokes equations and 2- incompressible Navier-Stokes equations. In the former approach, the effects associated with density changes in response to pressure variations, regarded as compressibility effects, are neglected, while variable inertia effects associated with changes in density due to heat transfer are present (Lele, 1994). In the case of incompressible Navier-Stokes equations, both these effects are neglected.

This thesis considers turbulent flows at low Mach numbers, subjected to significant thermophysical property variations at supercritical pressures, which are described by the compressible Navier-Stokes equations in the low-Mach number limit. The low-Mach number equations presented here have the same mathematical structure as the incompressible Navier-Stokes equations, in the sense that the thermodynamic pressure is assumed constant and the hydrodynamic pressure is determined from the mass conservation constraint.

In this chapter, we first present the detailed low-Mach number (also known as anelastic) approximation of the Navier-Stokes equations in cylindrical coordinates. Details of the numerical implementation in cylindrical coordinates and the specification of boundary conditions are also discussed. Next, we introduce different equation of state and models for transport properties. Finally, some information about the in-house code is presented.

2.2 Governing equations

To derive the low-Mach number approximation, we start from the fully compressible Navier-Stokes equations (Cook & Riley, 1996; Birken & Meister, 2005)

$$\frac{\partial \hat{\rho}}{\partial \hat{t}} + \frac{\partial \hat{\rho}\hat{u}_i}{\partial \hat{x}_i} = 0, \tag{2.1}$$

$$\frac{\partial \hat{\rho}\hat{u}_i}{\partial \hat{t}} + \frac{\partial \hat{\rho}\hat{u}_i\hat{u}_j}{\partial \hat{x}_j} = -\frac{\partial \hat{p}}{\partial \hat{x}_i} + \frac{\partial \hat{\tau}_{ij}}{\partial \hat{x}_j} + \hat{\rho}\hat{g}_i, \tag{2.2}$$

$$\frac{\partial \hat{\rho}\hat{h}}{\partial \hat{t}} + \frac{\partial \hat{\rho}\hat{u}_i\hat{h}}{\partial \hat{x}_i} = \frac{\partial \hat{p}}{\partial \hat{t}} + \hat{u}_i\frac{\partial \hat{p}}{\partial \hat{x}_i} - \frac{\partial q_i}{\partial x_i} + \hat{\tau}_{ij}\frac{\partial \hat{u}_i}{\partial \hat{x}_j} + \rho\hat{u}_i\hat{g}_i, \tag{2.3}$$

with the stress tensor

$$\hat{\tau}_{ij} = \hat{\mu}\hat{S}_{ij} = \hat{\mu}\left(\frac{\partial \hat{u}_i}{\partial \hat{x}_j} + \frac{\partial \hat{u}_j}{\partial \hat{x}_i} - \frac{2}{3}\left(\frac{\hat{\mu}_b}{\hat{\mu}} + 1\right)\frac{\partial \hat{u}_k}{\partial \hat{x}_k}\delta_{ij}\right),$$

and the Fourier law for the heat conduction

$$q_i = -\hat{\lambda}\frac{\partial \hat{T}}{\partial \hat{x}_i} \quad \xRightarrow{d\hat{h}=\hat{c}_p d\hat{T}} \quad q_i = -\frac{\hat{\lambda}}{\hat{c}_p}\frac{\partial \hat{h}}{\partial \hat{x}_i} = -\hat{\alpha}\frac{\partial \hat{h}}{\partial \hat{x}_i}.$$

In these equations the hat sign ˆ denotes the dimensional quantities and the terms $\hat{t}$, $\hat{x}_i$, $\hat{\rho}$, $\hat{\mu}$, $\hat{\mu}_b$, $\hat{\lambda}$, $\hat{c}_p$, $\hat{u}_i$, $\hat{T}$, $\hat{p}$, $\hat{h}$ and $\hat{g}_i$ are the time, coordinates, density, dynamic viscosity, bulk viscosity, thermal conductivity, isobaric heat capacity, velocity components, temperature, pressure, enthalpy and gravitational acceleration, respectively.

In computational fluid dynamics, it is convenient to work with the non-dimensional form of Navier-Stokes since, it simplifies the analysis of the problem and reduces the number of free parameters. Thus, by choosing an appropriate reference value denoted by subscript $_0$, the non-dimensional form of Eqs. (2.1)-(2.3) are as follows:

$$\frac{\partial \rho}{\partial t} + \frac{\partial \rho u_i}{\partial x_i} = 0, \tag{2.4}$$

$$\frac{\partial \rho u_i}{\partial t} + \frac{\partial \rho u_i u_j}{\partial x_j} = -\frac{1}{M_0^2}\frac{\partial p}{\partial x_i} + \frac{1}{Re_0}\frac{\partial \tau_{ij}}{\partial x_j} + \rho Ri_{0i}, \tag{2.5}$$

$$\frac{\partial \rho h}{\partial t} + \frac{\partial \rho u_i h}{\partial x_i} = \frac{\partial p}{\partial t} + u_i\frac{\partial p}{\partial x_i} - \frac{1}{Re_0 Pr_0}\frac{\partial q_i}{\partial x_i} + M_0^2\tau_{ij}\frac{\partial u_i}{\partial x_j} + \rho M_0^2 Ri_{0i}, \tag{2.6}$$

where the non-dimensional variable are defined as,

$$t = \frac{\hat{t}}{\hat{L}/\hat{U}_0}, \quad x_i = \frac{\hat{x}_i}{\hat{L}}, \quad \rho = \frac{\hat{\rho}}{\hat{\rho}_0}, \quad \mu = \frac{\hat{\mu}}{\hat{\mu}_0}, \quad \lambda = \frac{\hat{\lambda}}{\hat{\lambda}_0},$$

$$c_p = \frac{\hat{c_p}}{\hat{c}_{p0}}, \quad u_i = \frac{\hat{u}_i}{\hat{U}_0}, \quad T = \frac{\hat{T}\hat{c}_p}{\hat{c}^2}, \quad p = \frac{\hat{P}}{\hat{\rho}_0\hat{c}_0^2}, \quad h = \frac{\hat{h} - \hat{h}_0}{\hat{c}_0^2}. \tag{2.7}$$

The non-dimensional parameters shown in the above equations are written as,

Reynolds number $Re_0 = \hat{\rho}_0\hat{U}_0\hat{L}/\hat{\mu}_0$,

Richardson number $Ri_{0i} = \hat{g}_i\hat{L}/\hat{U}_0^2$,

Prandtl number $Pr_0 = \hat{c}_{p0}\hat{\mu}_0/\hat{\lambda}_0$, and

Mach number $M_0 = \hat{U}_0/\hat{c}_0$.

Note that the pressure and the enthalpy are scaled by the speed of sound $\hat{c}$.
Next, the mathematical analysis of the low Mach number limit is performed using the

asymptotic expansion of the flow variables Majda & Sethian (1985) in terms of reference Mach number M_0,

$$f(x_i,t) = f^{(0)}(x_i,t) + M_0 f^{(1)}(x_i,t) + M_0^2 f^{(2)}(x_i,t) + ... + M_0^k f^{(k)}(x_i,t), \tag{2.8}$$

where f is a generic quantity. The conservation equations for mass, momentum and enthalpy can then be written as

$$\frac{\partial \rho^{(0)}}{\partial t} + \frac{\partial (\rho u_i)^{(0)}}{\partial x_i} + O\left(M_0, M_0^2, ...\right) = 0, \tag{2.9}$$

$$\frac{\partial (\rho u_i)^{(0)}}{\partial t} + \frac{\partial (\rho u_i u_j)^{(0)}}{\partial x_j} = -\frac{1}{M_0^2}\frac{\partial p^{(0)}}{\partial x_i} - \frac{1}{M_0}\frac{\partial p^{(1)}}{\partial x_i} - \frac{\partial p^{(2)}}{\partial x_i} + \frac{1}{Re_0}\frac{\partial \tau_{ij}^{(0)}}{\partial x_j} + \rho^{(0)} Ri_{0i} + O\left(M_0, M_0^2, ...\right), \tag{2.10}$$

$$\frac{\partial (\rho h)^{(0)}}{\partial t} + \frac{\partial (\rho u_i h)^{(0)}}{\partial x_i} = \frac{\partial p^{(0)}}{\partial t} + u_i^{(0)}\frac{\partial p^{(0)}}{\partial x_i} - \frac{1}{Re_0 Pr_0}\frac{\partial q_i^{(0)}}{\partial x_i} + O\left(M_0, M_0^2, ...\right). \tag{2.11}$$

The terms of order $O\left(M_0^k\right)$ for integers $k \geq 1$, as a result of the asymptotic expansion, are lumped together and can be neglected for low Mach number flows. Note, also the viscous heating term in the energy equation is of $O\left(M_0^2\right)$ and not shown explicitly. Since Eqs. (2.9)-(2.11) are supposed to hold for arbitrary values of M_0 (i.e. $M_0 << 1$), the coefficients of the monomial $M_0^k (k = -2, -1, 0)$ must be equal. Equating powers of M_0^{-2} and M_0^{-1} in the momentum equations, shows that the spatial gradient of $p^{(0)}$ and $p^{(1)}$ (first and second term on the right-hand side of Eq. (2.10)) are zero in the low Mach number limit. Therefore, also the second term on the right-hand side in the enthalpy equation can be omitted. If the system under study is closed, then the total mass is constant over time and by integrating the equation of state over the total volume the time-dependent expression for the thermodynamic pressure $p^{(0)}(t)$ can be obtained. This expression is zero for open systems; see Nicoud (1998); Najm *et al.* (1998). Now, the pressure field is decomposed into its thermodynamic $p^{(0)}$ and hydrodynamic $p^{(2)}$ part and one can determine all thermodynamic state variables, such as density, enthalpy, etc., independently of the hydrodynamic pressure variations.

Scaling the velocity with the inlet friction velocity $\hat{u}_{\tau 0} = \sqrt{\hat{\tau}_w / \hat{\rho}}$, the pressure with $\hat{\rho}_0 \hat{u}_{\tau 0}^2$, the enthalpy as $h = \left(\hat{h} - \hat{h}_0\right) / \left(\hat{c}_{p0} \hat{T}_0\right)$ and coordinates with pipe diameter $\hat{D}$ the final set of conservative equations in cylindrical coordinates are as follows (the superscript numbers are omitted for simplicity):
Conservation of mass,

$$\frac{\partial \rho}{\partial t} + \frac{1}{r}\frac{\partial r \rho u}{\partial r} + \frac{1}{r}\frac{\partial \rho v}{\partial \theta} + \frac{\partial \rho w}{\partial z} = 0. \tag{2.12}$$

Conservation of momentum in radial direction r,

$$\begin{aligned}\frac{\partial \rho u}{\partial t} + \frac{1}{r}\frac{\partial r\rho uu}{\partial r} + \frac{1}{r}\frac{\partial \rho uv}{\partial \theta} + \frac{\partial \rho uw}{\partial z} - \frac{\rho vv}{r} &= -\frac{\partial p}{\partial r} + \frac{1}{Re_{\tau 0}}\left[\frac{1}{r}\frac{\partial r\tau_{rr}}{\partial r}\right.\\ &\left. + \frac{1}{r}\frac{\partial \tau_{r\theta}}{\partial \theta} - \frac{\tau_{\theta\theta}}{r} + \frac{\partial \tau_{rz}}{\partial z}\right] + \rho Ri_{0r}. \end{aligned} \tag{2.13}$$

Conservation of momentum in circumferential direction θ,

$$\begin{aligned}\frac{\partial \rho v}{\partial t} + \frac{1}{r}\frac{\partial r\rho vu}{\partial r} + \frac{1}{r}\frac{\partial \rho vv}{\partial \theta} + \frac{\partial \rho vw}{\partial z} + \frac{\rho vu}{r} &= -\frac{1}{r}\frac{\partial p}{\partial \theta} + \frac{1}{Re_{\tau 0}}\left[\frac{1}{r}\frac{\partial r\tau_{\theta r}}{\partial r}\right.\\ &\left. + \frac{\tau_{\theta r}}{r} + \frac{1}{r}\frac{\partial \tau_{\theta\theta}}{\partial \theta} + \frac{\partial \tau_{\theta z}}{\partial z}\right] + \rho Ri_{0\theta}. \end{aligned} \tag{2.14}$$

Conservation of momentum in axial direction z,

$$\begin{aligned}\frac{\partial \rho w}{\partial t} + \frac{1}{r}\frac{\partial r\rho wu}{\partial r} + \frac{1}{r}\frac{\partial \rho wv}{\partial \theta} + \frac{\partial \rho ww}{\partial z} &= -\frac{\partial p}{\partial z} + \frac{1}{Re_{\tau 0}}\left[\frac{1}{r}\frac{\partial r\tau_{zr}}{\partial r} + \frac{1}{r}\frac{\partial \tau_{z\theta}}{\partial \theta}\right.\\ &\left. + \frac{\partial \tau_{zz}}{\partial z}\right] + \rho Ri_{0z}. \end{aligned} \tag{2.15}$$

Conservation of energy,

$$\begin{aligned}\frac{\partial \rho h}{\partial t} + \frac{1}{r}\frac{\partial r\rho hu}{\partial r} + \frac{1}{r}\frac{\partial \rho hv}{\partial \theta} + \frac{\partial \rho hw}{\partial z} &= \frac{1}{Re_{\tau 0}Pr_0}\left[\frac{1}{r}\frac{\partial}{\partial r}\left(r\alpha\frac{\partial h}{\partial r}\right)\right.\\ &\left. + \frac{1}{r}\frac{\partial}{\partial \theta}\left(\frac{\alpha}{r}\frac{\partial h}{\partial \theta}\right) + \frac{\partial}{\partial z}\left(\alpha\frac{\partial h}{\partial z}\right)\right]. \end{aligned} \tag{2.16}$$

The stress tensors in the momentum equations are given as,

$$\tau_{rr} = \mu\left(2\frac{\partial u}{\partial r} + \left(\frac{\mu_b}{\mu} - \frac{2}{3}\right)\nabla\cdot\mathbf{u}\right), \tag{2.17}$$

$$\tau_{\theta\theta} = \mu\left(2\left(\frac{1}{r}\frac{\partial v}{\partial \theta} + \frac{u}{r}\right) + \left(\frac{\mu_b}{\mu} - \frac{2}{3}\right)\nabla\cdot\mathbf{u}\right), \tag{2.18}$$

$$\tau_{zz} = \mu\left(2\frac{\partial w}{\partial z} + \left(\frac{\mu_b}{\mu} - \frac{2}{3}\right)\nabla\cdot\mathbf{u}\right), \tag{2.19}$$

$$\tau_{r\theta} = \tau_{\theta r} = \mu\left(r\frac{\partial}{\partial r}\left(\frac{v}{r}\right) + \frac{1}{r}\frac{\partial u}{\partial \theta}\right), \tag{2.20}$$

$$\tau_{rz} = \tau_{zr} = \mu\left(\frac{\partial w}{\partial r} + \frac{\partial u}{\partial z}\right), \tag{2.21}$$

$$\tau_{z\theta} = \tau_{\theta z} = \mu\left(\frac{\partial v}{\partial z} + \frac{1}{r}\frac{\partial w}{\partial \theta}\right), \tag{2.22}$$

where,

$$\nabla \cdot \mathbf{u} = \frac{1}{r}\frac{\partial ru}{\partial r} + \frac{1}{r}\frac{\partial v}{\partial \theta} + \frac{\partial w}{\partial z}. \tag{2.23}$$

The non-dimensional numbers are then given as

$$Re_{\tau 0} = \frac{\hat{\rho}_0 \hat{u}_{\tau 0} \hat{D}}{\hat{\mu}_0}, \quad Pr_0 = \frac{\hat{\mu}_0 \hat{c}_{p0}}{\hat{\lambda}_0}, \quad Ri_{0i} = \frac{\hat{g}_i \hat{D}}{\hat{u}_{\tau 0}^2} = \frac{Gr_{0i}}{\hat{\beta}_0 \hat{T}_0 Re_{\tau 0}^2 Q} \tag{2.24}$$

$$Q = \frac{\hat{q}_w \hat{D}}{\hat{\lambda}_0 \hat{T}_0} = Re_{\tau 0} Pr_0 q, \quad Gr_{0i} = \frac{\hat{\rho}_0^2 \hat{g}_i \hat{\beta}_0 \hat{q}_w \hat{D}^4}{\hat{\mu}_0^2 \hat{\lambda}_0}, \tag{2.25}$$

where $Re_{\tau 0}$ is the reference Reynolds number, based on the reference friction velocity and the pipe diameter $\hat{D}$, Pr_0 is the reference Prandtl number, Ri_{0i} is the reference Richardson number, Gr_{0i} is the reference Grashof number, Q is the non-dimensional constant wall heat flux, and $\hat{q}_w$ is dimensional the constant wall heat flux.

2.3 Numerical scheme

The details of numerical techniques, which are employed to solve the governing equations using DNS are discussed. The spatial and temporal discretization, numerical solution procedure, boundary and initial conditions are presented.

2.3.1 Spatial discretization

The spatial discretization of the Navier-Stokes equations is carried out using the second-order central difference method. In this technique, first, the flow domain is decomposed into a finite number of sub-domains, called control volumes, as shown in 2.1 for cylindrical coordinates. A staggered grid is applied in which the hydrodynamic pressure p, enthalpy h and all thermophysical properties are located at the center of each control volume, while velocity components are defined at the faces. Next, the discretized continuity and energy equations are integrated over the volume around the center and the momentum equations for each velocity component are integrated over the volume around the volume faces (shifted forward in each direction for half of the CV). Finally, we apply surface integrals to the control volume for each variable using numerical integration methods. To find the variables at locations of control volume that are not defined, an interpolation method is applied.

The interpolation operators for each velocity component and any arbitrary scalar are written as:

$$u_{i,j,k} = \frac{u_{i+1/2,j,k} + u_{i-1/2,j,k}}{2}, \quad v_{i,j,k} = \frac{u_{i,j+1/2,k} + u_{i,j-1/2,k}}{2},$$

$$w_{i,j,k} = \frac{u_{i,j,k+1/2} + u_{i,j,k-1/2}}{2} \tag{2.26}$$

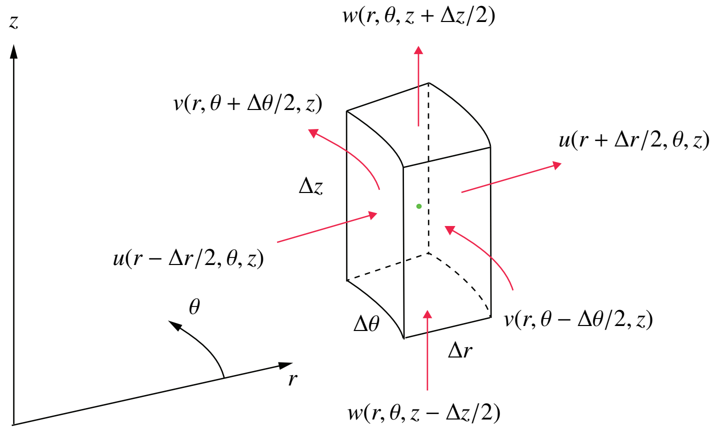

Figure 2.1: Instant control volume in cylindrical coordinates.

and the differencing operators,

$$\left.\frac{\partial u}{\partial r}\right|_{i,j,k} = \frac{u_{i+1/2,j,k} - u_{i-1/2,j,k}}{\Delta r}, \qquad \left.\frac{1}{r}\frac{\partial v}{\partial \theta}\right|_{i,j,k} = \frac{v_{i,j+1/2,k} - v_{i,j-1/2,k}}{r\Delta\theta},$$

$$\left.\frac{\partial w}{\partial z}\right|_{i,j,k} = \frac{w_{i,j,k+1/2} - w_{i,j,k-1/2}}{\Delta z} \tag{2.27}$$

For the discretization of the advection term in the energy equation, a different scheme is applied. To reduce oscillations due to the sharp gradients in enthalpy, the Koren slope limiter (Koren, 1993), which is third-order accurate, is used to approximate the undefined enthalpy values at the cell faces. The Koren slope limiter is defined as follows:

$$h_{i+1/2,j,k} = h_{i,j,k} - \phi(r_i)\left[h_{i+1,j,k} - h_{i,j,k}\right], \quad r_i = \frac{h_{i,j,k} - h_{i-1,j,k}}{h_{i+1,j,k} - h_{i,j,k}}, \tag{2.28}$$

$$h_{i,j+1/2,k} = h_{i,j,k} - \phi(r_j)\left[h_{i,j+1,k} - h_{i,j,k}\right], \quad r_j = \frac{h_{i,j,k} - h_{i,j-1,k}}{h_{i,j+1,k} - h_{i,j,k}}, \tag{2.29}$$

$$h_{i,j,k+1/2} = h_{i,j,k} - \phi(r_k)\left[h_{i,j,k+1} - h_{i,j,k}\right], \quad r_k = \frac{h_{i,j,k} - h_{i,j,k-1}}{h_{i,j,k+1} - h_{i,j,k}}, \tag{2.30}$$

where ϕ is the slope limiter function $\phi = max\,[0, min(2r,(2+r)/3, 2)]$.

2.3.2 Temporal discretization

To solve the low-Mach number or incompressible form of Navier-Stokes equations, the fractional-step method is used, where the pressure field is computed by solving a Poisson equation with the time derivative of the density as a part of the source term. It has been observed that in flows with large density ratios, the discrete approximation of the density time derivative (Eq. (2.12)) is a potential source of instability and needs careful treatment. Among the different approximations for the density time derivative, the even-ordered explicit approximations have been found to be more stable. However, for density ratios larger than 3 they were found to be unstable (Nicoud, 2000; Cook & Riley, 1996). Najm *et al.* (1998) developed a two-sub-step predictor-corrector algorithm for chemically reacting flows at the low-Mach number, in which the predictor sub-step uses a second-order Adams-Bashforth time integration scheme and the corrector sub-step applies a quasi-Crank-Nicolson integration. They showed that this approach is stable for very large density ratios.

In this work, to tackle the instability due to very large density ratios at supercritical pressures, the time integration of Eqs. (2.12) to (2.16) is performed using a similar approach. Note, to approximate the density in the first sub-step, we use first-order approximation. To predict the velocity and enthalpy fields, a second-order Adams-Bashforth method is used to correct the pressure to satisfy the continuity equation. In corrector sub-step, a second-order Adams-Moulton method is applied. In both sub-steps, a Poisson equation is solved using fast Fourier transforms (FFT) to predict the pressure. It is important to note that the diffusion terms in circumferential directions for both momentum and energy equations are treated implicitly; because the circumferential grid size near the centerline ($r\Delta\theta \approx \Delta r\Delta\theta$) is the term that severely limits the time-step. The remaining terms are treated explicitly. The procedure in the present study is summarised below.

Note that, the superscripts ^{n}, $^{n+1/2}$ and $^{n+1}$ refer to the values at the previous, intermediate and next time step, respectively. The superscripts * and ** corresponds to the predicted values.

Sub-step 1 (predictor):

1. The predicted value for the density is approximated by

$$\frac{\rho^{*}-\rho^{n}}{\Delta t}=\left.\frac{\partial\rho}{\partial t}\right|^{n}. \tag{2.31}$$

Using a linear extrapolation in time for the right-hand side of this equation, leads to

$$\frac{\rho^{*}-\rho^{n}}{\Delta t}=\frac{\rho^{n}-\rho^{n-1}}{\Delta t}, \tag{2.32}$$

$$\rho^{*}=2\rho^{n}-\rho^{n-1}. \tag{2.33}$$

2. The intermediate enthalpy is advanced in time by solving the energy as follows,

$$\frac{(\rho h)^{n+1/2}-(\rho h)^{n}}{\Delta t}-\frac{1}{Re_{\tau 0}Pr_{0}}\frac{1}{r}\frac{\partial}{\partial\theta}\left(\frac{\alpha}{r}\frac{\partial h}{\partial\theta}\right)\Bigg|^{n+1/2}=\frac{3}{2}RHS_{h}^{n}-\frac{1}{2}RHS_{h}^{n-1}, \tag{2.34}$$

where RHS_h is the discretized form of

$$RHS_h = -\frac{1}{r}\frac{\partial r\rho h u}{\partial r} - \frac{1}{r}\frac{\partial \rho h v}{\partial \theta} - \frac{\partial \rho h w}{\partial z} + \frac{1}{Re_{\tau 0}Pr_0}\left[\frac{1}{r}\frac{\partial}{\partial r}\left(r\alpha\frac{\partial h}{\partial r}\right) + \frac{\partial}{\partial z}\left(\alpha\frac{\partial h}{\partial z}\right)\right], \tag{2.35}$$

and the enthalpy is $h^{n+1/2} = (\rho h)^{n+1/2}/\rho^*$.

3. The thermophysical properties of the fluid are updated based on intermediate enthalpy from the table using a cubic spline interpolation $\phi^{n+1/2} = \phi\left(h^{n+1/2}\right)$.

4. Next, the velocity field is calculated using a fractional-step method developed by Kim & Moin (1985). First, the intermediate velocity field is approximated by splitting the pressure from the momentum equation

$$\frac{(\rho u)^* - (\rho u)^n}{\Delta t} - \frac{1}{Re_{\tau 0}}\frac{1}{r}\frac{\partial}{\partial \theta}\left(\frac{\mu}{r}\frac{\partial u^*}{\partial \theta}\right) = \frac{3}{2}RHS_u^n - \frac{1}{2}RHS_u^{n-1}, \tag{2.36}$$

$$\frac{(\rho v)^* - (\rho v)^n}{\Delta t} - \frac{2}{Re_{\tau 0}}\frac{1}{r}\frac{\partial}{\partial \theta}\left(\frac{\mu}{r}\frac{\partial v^*}{\partial \theta}\right) = \frac{3}{2}RHS_v^n - \frac{1}{2}RHS_v^{n-1}, \tag{2.37}$$

$$\frac{(\rho w)^* - (\rho w)^n}{\Delta t} - \frac{1}{Re_{\tau 0}}\frac{1}{r}\frac{\partial}{\partial \theta}\left(\frac{\mu}{r}\frac{\partial w^*}{\partial \theta}\right) = \frac{3}{2}RHS_w^n - \frac{1}{2}RHS_w^{n-1}, \tag{2.38}$$

where

$$\begin{aligned} RHS_u = &-\frac{1}{r}\frac{\partial r\rho uu}{\partial r} - \frac{1}{r}\frac{\partial \rho uv}{\partial \theta} - \frac{\partial \rho uw}{\partial z} + \frac{\rho vv}{r} + \frac{1}{Re_{\tau 0}}\left[\frac{1}{r}\frac{\partial r\tau_{rr}}{\partial r}\right. \\ &\left. + \frac{1}{r}\frac{\partial}{\partial \theta}\left(\mu r\frac{\partial}{\partial r}\left(\frac{v}{r}\right)\right) - \frac{\tau_{\theta\theta}}{r} + \frac{\partial \tau_{rz}}{\partial z}\right] + \rho Ri_{0r}, \end{aligned} \tag{2.39}$$

$$\begin{aligned} RHS_v = &-\frac{1}{r}\frac{\partial r\rho vu}{\partial r} - \frac{1}{r}\frac{\partial \rho vv}{\partial \theta} - \frac{\partial \rho vw}{\partial z} - \frac{\rho vu}{r} + \frac{1}{Re_{\tau 0}}\left[\frac{1}{r^2}\frac{\partial r^2\tau_{\theta r}}{\partial r}\right. \\ &\left. + \frac{1}{r}\frac{\partial}{\partial \theta}\left(2\mu\left(\frac{u}{r} - \frac{1}{3}\nabla\cdot\mathbf{u}\right)\right) + \frac{\partial \tau_{\theta z}}{\partial z}\right] + \rho Ri_{0\theta}, \end{aligned} \tag{2.40}$$

$$\begin{aligned} RHS_w = &-\frac{1}{r}\frac{\partial r\rho wu}{\partial r} - \frac{1}{r}\frac{\partial \rho wv}{\partial \theta} - \frac{\partial \rho ww}{\partial z} + \frac{1}{Re_{\tau 0}}\left[\frac{1}{r}\frac{\partial r\tau_{zr}}{\partial r} + \frac{1}{r}\frac{\partial}{\partial \theta}\left(\mu\frac{\partial v}{\partial z}\right)\right. \\ &\left. + \frac{\partial \tau_{zz}}{\partial z}\right] + \rho Ri_{0z}. \end{aligned} \tag{2.41}$$

5. A Poisson equation is solved to determine the pressure field, which is required to satisfy the continuity equation

$$\nabla^2 p^{n+1/2} = \frac{1}{\Delta t}\left(\nabla \cdot (\rho \mathbf{u})^* + \left.\frac{\partial \rho}{\partial t}\right|^*\right), \tag{2.42}$$

   where $\partial\rho/\partial t|^*$ is discretized with second-order approximation,

$$\left.\frac{\partial \rho}{\partial t}\right|^* = \frac{\rho^{n+1/2} - 2\rho^n + \rho^{n-1}}{\Delta t}. \tag{2.43}$$

6. We then obtain the velocity field with the predicted pressure field as follows,

$$(\rho u)^{n+1/2} = (\rho u)^* - \Delta t \frac{\partial p^{n+1/2}}{\partial r}, \quad u^{n+1/2} = \frac{(\rho u)^{n+1/2}}{\rho^{n+1/2}} \tag{2.44}$$

$$(\rho v)^{n+1/2} = (\rho v)^* - \Delta t \frac{1}{r}\frac{\partial p^{n+1/2}}{\partial \theta}, \quad v^{n+1/2} = \frac{(\rho v)^{n+1/2}}{\rho^{n+1/2}} \tag{2.45}$$

$$(\rho w)^{n+1/2} = (\rho w)^* - \Delta t \frac{\partial p^{n+1/2}}{\partial z}, \quad w^{n+1/2} = \frac{(\rho w)^{n+1/2}}{\rho^{n+1/2}}. \tag{2.46}$$

Sub-step 2 (corrector):

1. The corrected values for the density and enthalpy (at time step $n+1$) are obtained using a second-order Adams-Moulton integration

$$\frac{\rho^{**} - \rho^n}{\Delta t} = \frac{1}{2}\left.\frac{\partial \rho}{\partial t}\right|^{**} + \frac{1}{2}\left.\frac{\partial \rho}{\partial t}\right|^{n}. \tag{2.47}$$

   Similar to the predictor sub-step, using linear extrapolation in time for the right-hand side of this equation gives

$$\rho^{**} = \frac{1}{2}\rho^{n+1/2} + \rho^n - \frac{1}{2}\rho^{n-1}. \tag{2.48}$$

2. The enthalpy at the next step is approximated by time advancement of the energy equation as

$$\frac{(\rho h)^{n+1} - (\rho h)^n}{\Delta t} - \left.\frac{1}{Re_{\tau 0} Pr_0}\frac{1}{r}\frac{\partial}{\partial \theta}\left(\frac{\alpha}{r}\frac{\partial h}{\partial \theta}\right)\right|^{n+1} = \frac{1}{2}RHS_h^{n+1/2} + \frac{1}{2}RHS_h^n, \tag{2.49}$$

   where the enthalpy at new time step is $h^{n+1} = (rhoh)^{n+1}/\rho^{**}$.

3. The thermophysical properties of the fluid at the new time step are updated based on the enthalpy at new time step $\phi^{n+1} = \phi\left(h^{n+1}\right)$.

4. To obtain the velocity field, we first calculate the intermediate velocity field,

$$\frac{(\rho u)^{**}-(\rho u)^{n}}{\Delta t}-\frac{1}{Re_{\tau 0}}\frac{1}{r}\frac{\partial}{\partial\theta}\left(\frac{\mu}{r}\frac{\partial u^{**}}{\partial\theta}\right)=\frac{3}{2}RHS_{u}^{n}-\frac{1}{2}RHS_{u}^{n-1}, \tag{2.50}$$

$$\frac{(\rho v)^{**}-(\rho v)^{n}}{\Delta t}-\frac{2}{Re_{\tau 0}}\frac{1}{r}\frac{\partial}{\partial\theta}\left(\frac{\mu}{r}\frac{\partial v^{**}}{\partial\theta}\right)=\frac{3}{2}RHS_{v}^{n}-\frac{1}{2}RHS_{v}^{n-1}, \tag{2.51}$$

$$\frac{(\rho w)^{**}-(\rho w)^{n}}{\Delta t}-\frac{1}{Re_{\tau 0}}\frac{1}{r}\frac{\partial}{\partial\theta}\left(\frac{\mu}{r}\frac{\partial w^{**}}{\partial\theta}\right)=\frac{3}{2}RHS_{w}^{n}-\frac{1}{2}RHS_{w}^{n-1}. \tag{2.52}$$

5. Similar to the predicted pressure, the pressure field at the new time step is obtained by solving the Poisson equation

$$\nabla^{2}p^{n+1}=\frac{1}{\Delta t}\left(\nabla\cdot(\rho\mathbf{u})^{**}+\left.\frac{\partial\rho}{\partial t}\right|^{n+1}\right), \tag{2.53}$$

where $\partial\rho/\partial t|^{n+1}$ is discretized with second-order approximation.

$$\left.\frac{\partial\rho}{\partial t}\right|^{n+1}=\frac{\rho^{n+1}-2\rho^{n}+\rho^{n-1}}{\Delta t}. \tag{2.54}$$

6. The velocity field at the new time step is

$$(\rho u)^{n+1}=(\rho u)^{**}-\Delta t\frac{\partial p^{n+1}}{\partial r},\quad u^{n+1}=\frac{(\rho u)^{n+1}}{\rho^{n+1}} \tag{2.55}$$

$$(\rho v)^{n+1}=(\rho v)^{**}-\Delta t\frac{1}{r}\frac{\partial p^{n+1}}{\partial\theta},\quad v^{n+1}=\frac{(\rho v)^{n+1}}{\rho^{n+1}} \tag{2.56}$$

$$(\rho w)^{n+1}=(\rho w)^{**}-\Delta t\frac{\partial p^{n+1}}{\partial z},\quad w^{n+1}=\frac{(\rho w)^{n+1}}{\rho^{n+1}}. \tag{2.57}$$

2.3.3 Boundary conditions

Boundary conditions must be specified to complete the time advancement at each time step. We now introduce four different types of boundary conditions for inlet, outlet, wall and centerline.

2.3.3.1 Inlet boundary condition

Generating realistic inlet boundary conditions for DNS of spatially developing flows is a challenging task. Effective and efficient turbulent inlet boundary conditions for DNS should reflect the unsteady nature of turbulence. Different methods for generating inflow boundary conditions have been developed by different researchers. A complete review of these methods can be found in Tabor & Baba-Ahmadi (2010). They classified the existing

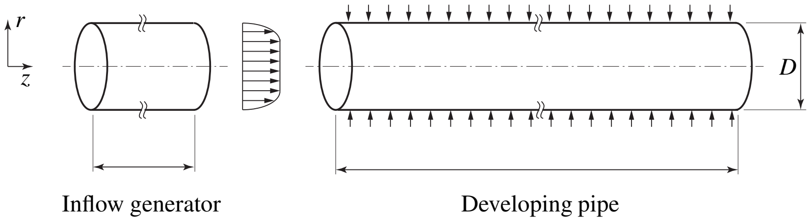

Figure 2.2: Geometry of the simulation domain.

methods into two main categories, (1) synthetic generation of turbulence and (2) precursor simulation method. The synthetic generation of turbulence is based on the principles of superposition of random fluctuations on the mean flow at the inlet using some spatial and temporal correlations. In this work, we use the precursor simulation method, which is the most accurate way of inflow turbulence generation (Tabor & Baba-Ahmadi, 2010). In this case, a separate periodic simulation is performed to generate a database of turbulence data to provide for the inflow of the spatially developing simulation. As it can be seen from Fig. 2.2, the simulation setup for the supercritical fluid heat transfer simulations consists of two parts, namely the precursor simulation (inflow generator) and the simulation of the developing pipe flow. First, the precursor simulation is performed, and the library of turbulence data is generated by sampling and storing the velocity. The stored library of turbulence data is fed into the spatially developing pipe with the same inlet *Re*, mesh resolution and time step as the for the simulation of the inlet flow field. As for the thermal inlet boundary condition, we assumed that the fluid enters the domain with a uniform enthalpy distribution.

2.3.3.2 Outlet boundary condition

A convective condition is used to model the outflow, where the details of the flow velocity, pressure and temperature are not known prior to the solution of the flow problem. Mathematically, this boundary condition is written as

$$\frac{\partial \eta}{\partial t} + C\frac{\partial \eta}{\partial z} = 0, \tag{2.58}$$

where η can be any velocity components or enthalpy and C is convective outflow velocity, which in this case is the outlet bulk velocity. It is evident that, the total mass must be balanced for the entire domain. In order to check that, the net of inlet and outlet flow and the net changes in mass in the interior of the domain is calculated:

$$\omega = \iiint\limits_{V} \frac{\partial \rho}{\partial t}\, r dr\, d\theta\, dz + \iint\limits_{outlet} \rho w\, r dr\, d\theta - \iint\limits_{inlet} \rho w\, r dr\, d\theta. \tag{2.59}$$

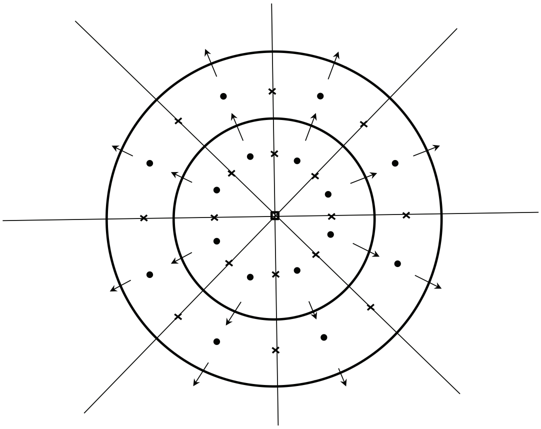

Figure 2.3: Staggered grid in cylindrical coordinates close to centreline. Arrows are the position of wall-normal velocity component u.

This value is being added to the outflow to satisfy the global mass conservation at each time step; note that $\omega \leq (10^{-3})$.

2.3.3.3 Wall boundary condition

Standard no-slip wall boundary conditions are used for the velocity and Neumann conditions (constant heat flux) for enthalpy. To set the boundary condition, an iterative Newton approach is used to solve the heat balance at the wall ($\alpha \partial h / \partial r|_w = q$) to calculate the wall enthalpy. This is due to the non-linear coupling of wall enthalpy h_w and wall fluid properties α_w.

2.3.3.4 Centreline boundary condition

The wall-normal velocity component u needs a special treatment at the centerline. Referring to the figure 2.3, it can be seen that the wall-normal velocity u is collocated with the centerline $r = 0$. The analysis of the discrete equations shows that center-line condition is only needed for wall-normal velocity component u at first grid point located at $r = \Delta r$. In order to approximate the value of u at $r = 0$, a linear interpolation across the centerline is used Akselvoll & Moin (1995),

$$u(0, \theta, z) = \frac{u(\Delta r, \theta, z) - u(\Delta r, \theta + \pi, z)}{2}. \tag{2.60}$$

2.4 Equations of state

The state of a thermodynamic system is described by a variety of state variables, such as pressure P, volume V, temperature T and entropy S. An EOS represents a functional relationship between the state variables, such that $F(P, V, T, S, ...) = 0$. Most of the equation of state used today are written to express mathematical relationships between P, T and V. They are semi-empirical in nature and are fitted to data that are available from experiments. In this part, we give an overview on different equations of state, which are available and widely used.

2.4.1 Ideal gas equation of state

The simplest equation of state is known as the ideal gas law and defined as

$$PV = nRT, \tag{2.61}$$

where n and R are the number of moles and the universal gas constant, respectively. The ideal gas equation of state is reliable for non-polar gases at low pressures and high temperatures (Moran *et al.*, 2010). The main flaw in the ideal gas equation of state is the assumption that intermolecular interactions are insignificant. These interactions are negligible when the distance between molecules becomes large and kinetic energy of particles is high (low pressures and high temperatures), but they do become important as the distance between molecules decrease and kinetic energy of particles is low (high pressures and low temperatures). In this conditions, intermolecular interactions cannot be neglected, and one can obviously see the inaccurately predicted states by the ideal gas equation of state. Many gases, such as Hydrogen, Nitrogen and noble gases like Helium He and Neon Ne show ideal gas behaviour at ambient pressure.

2.4.2 Cubic equation of state

Cubic equations of state are the simplest equations to accurately represent the relation between pressure P, volume V, and temperature T, of both gas and liquid, in a wide range of temperatures and pressures. The general form of any cubic equation of state has the first, second, and third power of specific volume or density. These equations of state are simple, require only a few number of parameters and are computationally relatively inexpensive. Among the cubic equations of state, three equations that have been widely used are van der Waals, Soave-Redlich-Kwong and Peng-Robinson equations - they and briefly described below.

- The **van der Waals** equation of state, derived by Johannes Diderik van der Waals in 1873, modifies the ideal gas law. It approximates the properties of real gases by considering the force interaction between molecules and their size via

$$\left(P + \frac{a}{V_m^2}\right)(V_m - b) - RT = 0, \tag{2.62}$$

where $V_m = V/n$ is the molar volume. The constant a involves the intermolecular forces and b is related to the size of molecules. A higher the value of a corresponds to a stronger attraction between molecules, which results in a decrease of the real gas pressure. As it can be seen from Eq. (2.62), the constant b represents the excluded volume occupied by the gas molecules. The van der Waals equation was the first equation, which was able to work around the gas-liquid coexistence line. The constants a and b, known as the van der Waals constants, are generally calculated from critical properties P_{cr},V_{cr} and T_{cr} as

$$a = \frac{27\,(RT_{cr})^2}{64P_{cr}}, \quad b = \frac{RT_{cr}}{8P_{cr}}. \tag{2.63}$$

Usually, the van der Waals equation is expressed in non-dimensional form with reduced state variables $P_r = P/P_{cr}$, $V_r = V_m/V_{cr}$ and $T_r = T/T_{cr}$, as follows

$$\left(P_r + \frac{3}{V_r^2}\right)(3V_r - 1) - 8T_r = 0. \tag{2.64}$$

In order to compute the deviation of thermodynamic properties with respect to an ideal gas, departure functions are defined. Departure functions are usually defined for enthalpy H, entropy S, Internal Energy U, Helmholtz energy A and Gibbs free energy G. For enthalpy and entropy these departure functions are as follows

$$\frac{H - H_{ig}}{RT} = -\int_{V_m}^{\infty} \left[T\left(\frac{\partial Z}{\partial T}\right)_{V_m}\right] \frac{dV_m}{V_m} + Z - 1, \tag{2.65}$$

$$\frac{S - S_{ig}}{R} = -\int_{V_m}^{\infty} \left[T\left(\frac{\partial Z}{\partial T}\right)_{V_m} + 1 - Z\right] \frac{dV_m}{V_m} + \ln(Z), \tag{2.66}$$

where the subscript $_{ig}$ stands for ideal state and $Z = PV_m/RT$ is the compressibility factor. The departure functions for the van der Waals equation of state are

$$\frac{H - H_{ig}}{RT} = -\frac{2a}{V_m RT} + \frac{b}{V_m - b}, \tag{2.67}$$

$$\frac{S - S_{ig}}{R} = -\frac{2a}{V_m RT} + \ln\left(\frac{b}{V_m - b}\right) + \ln(Z). \tag{2.68}$$

Thermodynamic properties are computed using these departure functions. For instance, isobaric heat capacity for van der Waals equation of state is calculated using

$$C_P = \left(\frac{\partial H}{\partial T}\right)_P. \tag{2.69}$$

A drawback of these models is that in reality the constants a and b do not remain constant over the entire ranges of T and P; the intermolecular force interaction constant a shows temperature dependency and the constant b seems to be density-dependent. Another flaw of the van der Waals equation of state is its inability in complex mixtures, where several interaction parameters are required.

- The **Soave-Redlich-Kwong** equation of state was formulated first by Otto Redlich and Joseph Neng Shun Kwong (Redlich-Kwong) in 1949, to make the intermolecular force constant a temperature-dependent, which showed significant improvement over the van der Waals equation. The Redlich-Kwong equation of state performs relatively well for the simple fluids such as Argon and Xenon, for which the acentric factor (is the measure of the non-sphericity or centricity of molecules) is zero. However, for complex fluids with non-zero acentric factors the results were not in good agreement with experiments. Soave (1972) in 1972 modified the Redlich-Kwong equation of state to involve the non-sphericity of molecules as follows,

  $$\left(P + \frac{\kappa a}{V_m\left(V_m + b\right)}\right) - \frac{RT}{V_m - b} = 0, \tag{2.70}$$

  with

  $$a = 0.4275\frac{(RT_{cr})^2}{P_{cr}}, \quad b = 0.08664\frac{RT_{cr}}{P_{cr}}.$$

  $$\kappa = \left[1 + \psi\left(1 - T_r^{0.5}\right)\right]^2. \tag{2.71}$$

  $$\psi = 0.48508 + 1.55171\omega - 0.15613\omega^2. \tag{2.72}$$

  ω is the acentric factor which is a standard for the phase characterization of single and pure components, along with critical temperature, pressure, and volume and molecular weight. The enthalpy departure function for the Soave-Redlich-Kwong equation of state is (Mak, 1988)

  $$\frac{H - H_{ig}}{RT} = Z - 1 - 4.9284\left(1 + \psi\right)\frac{\sqrt{\kappa}}{T_r}\ln\left(1 + \frac{0.08664P_r/T_r}{Z}\right), \tag{2.73}$$

  $$\frac{S - S_{ig}}{R} = 4.9284\left(\frac{2\kappa}{T_r} - \frac{\partial\kappa}{\partial T_r}\right)\ln\left(\frac{Z}{Z + 0.08664P_r/T_r}\right) \tag{2.74}$$

  $$+\ln\left(\frac{Z}{Z - 0.08664P_r/T_r}\right) + \ln\left(Z\right), \tag{2.75}$$

  Soave's modification was able to predict the phase behaviour of complex fluids in comparison with the original Redlich-Kwong equation of state.

- The **Peng-Robinson** equation of state was developed in 1976 by Peng and Robinson. The temperature dependency of the attractive term a and the acentric factor ω introduced by Soave is preserved, however, they presented various parameters to describe this dependency and further manipulated the pressure correction term as follows,

$$P + \frac{\kappa a}{V_m^2 + 2V_m b - b^2} - \frac{RT}{V_m - b} = 0, \tag{2.76}$$

with

$$a = 0.4572\frac{(RT_{cr})^2}{P_{cr}}, \quad b = 0.0778\frac{RT_{cr}}{P_{cr}},$$

$$\kappa = \left[1 + \psi\left(1 - T_r^{0.5}\right)\right]^2. \tag{2.77}$$

$$\psi = 0.37464 + 1.54226\omega - 0.26992\omega^2 \tag{2.78}$$

The departure functions for Peng-Robinson equation of state are (Mak, 1988)

$$\frac{H - H_{ig}}{RT} = Z - 1 - 2.078\frac{(1+\psi)\sqrt{\kappa}}{T_r}\ln\left(\frac{Z + 0.1878P_r/T_r}{Z - 0.0322P_r/T_r}\right), \tag{2.79}$$

$$\frac{S - S_{ig}}{R} = \ln\left(Z - 0.0778\frac{P_r}{T_r}\right) - 2.078\psi\left(\frac{1+\psi}{\sqrt{T_r}} - \psi\right)\ln\left(\frac{Z + 0.1878P_r/T_r}{Z - 0.0322P_r/T_r}\right). \tag{2.80}$$

Although the Peng-Robinson equation of state is generally superior in predicting the liquid phase density of many materials, it exhibits a performance similar to the Soave-Redlich-Kwong equation.

2.4.3 Multi-parameter equation of state

Advanced equations of state are formulated to describe the real fluid properties for entire range of fluid states, and often expressed using the reduced form of the Helmholtz energy as a function of reduced density and temperature,

$$\frac{a(\rho,T)}{RT} = \frac{a^i(\rho,T)}{RT} + \frac{a^r(\rho,T)}{RT} = \alpha^i(\rho_r,T_r) + \alpha^r(\rho_r,T_r), \tag{2.81}$$

where a and α are the dimensional and non-dimensional form of the Helmholtz energy. $\alpha^i(\rho,T)$ and $\alpha^r(\rho,T)$ are the ideal and non-ideal part of the Helmholtz energy, respectively. All thermodynamic properties can be calculated using this relation. For instance, pressure and its derivatives (Span, 2000) are calculated as follows,

$$p(\rho,T) = \rho^2\left(\frac{\partial a}{\partial \rho}\right)_T, \quad \frac{p}{\rho RT} = 1 + \rho_r\left(\frac{\partial \alpha^r}{\partial \rho_r}\right)_{T_r},$$

$$\left(\frac{\partial p}{\partial \rho}\right)_T = RT\left(1 + 2\rho_r\left(\frac{\partial \alpha^r}{\partial \rho_r}\right)_{T_r} + \rho_r^2\left(\frac{\partial^2 \alpha^r}{\partial \rho_r^2}\right)_{T_r}\right),$$

$$\left(\frac{\partial p}{\partial T}\right)_\rho = R\rho\left(1+\rho_r\left(\frac{\partial \alpha^r}{\partial \rho_r}\right)_{T_r}+\rho_r T_r\left(\frac{\partial^2\alpha^r}{\partial\rho_r\partial T_r}\right)\right). \tag{2.82}$$

The ideal gas contribution to the Helmholtz energy is given by Span (2000)

$$a^i = h_0^i + \int_{T_0}^{T} c_p^i dT - RT - T\left(s_0^i + \int_{T_0}^{T}\frac{c_p^i}{T}dT - R\ln\left(\frac{\rho T}{\rho_0 T_0}\right)\right), \tag{2.83}$$

where the subscripts $_0$ stands for reference values. The reduced form of the ideal gas contribution to the Helmholtz energy can be written as follows,

$$\alpha^i = -1 + \frac{h_0^i}{RT} - \frac{s_0^i}{R} + \ln\frac{\rho_r T_r}{\rho_{r0}T_{r0}} + \frac{1}{RT_r}\int_{T_{r0}}^{T_r}\frac{c_p^i}{T_r}dT_r - \frac{1}{R}\int_{T_{r0}}^{T_r}\frac{c_p^i}{T_r}dT_r. \tag{2.84}$$

As it was shown, the ideal gas contribution to the Helmholtz energy is supported by theory. However, the non-ideal behaviour is usually computed using real fluid data and empirical models. The approach, which is required to formulate the $\alpha^r(\rho_r, T_r)$, uses optimisation to derive the parameter estimates, taking the reduced temperature T_r and the reduced density ρ_r as the independent variables. The general functional form of the reduced non-ideal part of Helmholtz energy reads

$$\alpha^r(\rho_r, T_r) = \sum_{k=1}^{K_{Pol}} N_k\rho_r^{d_k}\left(\frac{1}{T_r}\right)^{l_k} + \sum_{k=K_{Pol}+1}^{K_{Pol}+K_{Exp}} N_k\rho_r^{d_k}\left(\frac{1}{T_r}\right)^{l_k} e^{-\rho_r^{t_k}}, \tag{2.85}$$

where N_k are the coefficient for each term and d_k, l_k and t_k are the exponents for ρ_r, T_r and exponential ρ_r. The values of K_{Pol} and K_{Exp} have been chosen differently by different authors and represent varied levels of accuracy and numerical stability, e.g., Span & Wagner (2003*a*,*b*) and Kunz & Wagner (2012). More detailed descriptions on α^r formulation are provided by Kunz & Wagner (2012). Currently, multi-parameter equations of state are the most accurate equations of state in the thermodynamic region close to the critical point. Thermodynamic properties are derived from the different cubic equations of state and are compared to the ones obtained from the NIST database (Lemmon *et al.*, 2002) using the multi-parameter equation of state. Figures 2.4 and 2.5 show the comparison of predicted density ρ and isobaric heat capacity c_p, respectively. It can be seen that the agreement of the thermodynamic properties derived from cubic equations with those derived from the multi-parameter equation of state decreases in the following order: Peng-Robinson, Soave-Redlich-Kwong and van der Waals.

2.5 Transport properties

2.5.1 Dynamic viscosity and thermal conductivity

In the supercritical region the transport properties such as conductivity λ and viscosity μ show a peculiar behaviour with changes in pressure and temperature (for a review see

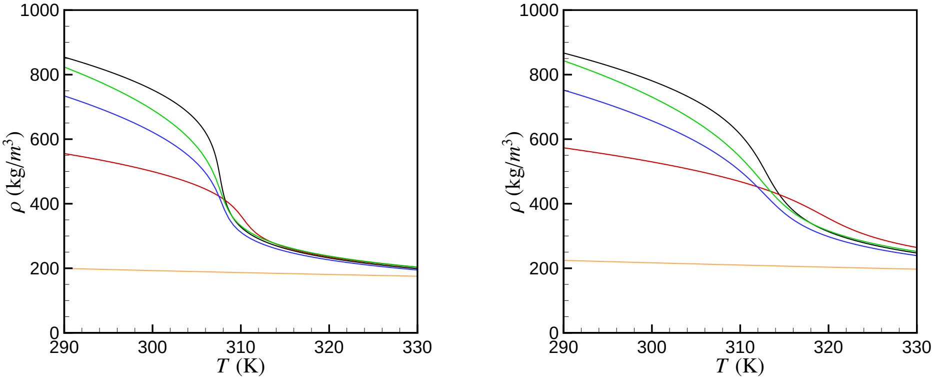

(a) 80 bar

(b) 90 bar

Figure 2.4: Variation of density of carbon-dioxide CO_2 with temperature T at pressures of P_0 = 80 and 90 bar in different equations of state. Orange - ideal gas; red - van der Waals; blue - Soave-Redlich-Kwong; green - Peng-Robinson; black - NIST database (Lemmon *et al.*, 2002).

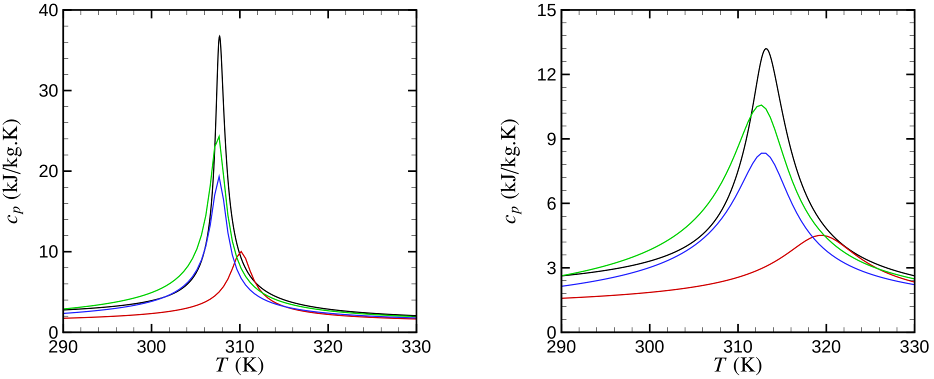

(a) 80 bar

(b) 90 bar

Figure 2.5: Variation of specific heat capacity of carbon-dioxide CO_2 with temperature T at pressures of P_0 = 80 and 90 bar in different equations of state. Red - van der Waals; blue - Soave-Redlich-Kwong; green - Peng-Robinson; black - NIST database (Lemmon *et al.*, 2002).

Millat *et al.* (1996)). To analyse the behaviour of these transport coefficients in the supercritical region, there has been models for the viscosity and thermal conductivity, which were developed by Vesovic *et al.* (1990). Their model has been widely used as a benchmark for transport properties. The functional form of their model is as follows

$$X(\rho, T) = X(0, T) + \Delta_c X(\rho, T) + \Delta X(\rho, T). \tag{2.86}$$

The first term is the contribution to the transport property stems from the pure molecular interaction in the limit of zero density. The second term represents the contributions of long-range fluctuations near critical point to the divergence of both the viscosity and thermal conductivity. The last term arises from the effects such as multibody collisions, molecular velocity correlations, and collisional transfer. They applied this model to predict the transport properties of CO_2 and showed that the model is valid for the temperature range of $100K \leq T \leq 1000K$ for viscosity and $100K \leq T \leq 1500K$ for thermal conductivity and pressures up to $100MPa$. They found a deviation of $< 5\%$ for the viscosity for gas phases, while for liquid phase the deviation was 7%. They reported that the large deviation for the liquid phase was due to the inconsistencies between the available experimental data. Later on, Fenghour *et al.* (1998) used the same model with more accurate experimental data and reported a large validity range for temperature ($100K \leq T \leq 1500K$) and pressure (up to $300MPa$) for viscosity. Figures 2.6 and 2.7 show the comparison of transport properties of CO_2 obtained from two widely used databases, NIST REFPROP (Lemmon *et al.*, 2002) and PROPATH (PROPATH Group, 1999). It can be seen that the main discrepancy between two databases is the prediction of the thermal conductivity.

2.5.2 Bulk viscosity

The classical compressible form of Navier-Stokes equations are usually used by considering the Stokes hypothesis (Stokes, 1849), which relates the bulk viscosity to the dynamic and second viscosity as $\mu_b = \mu' + 2\mu/3 = 0$. Even though the Stokes hypothesis was assumed for incompressible ($\nabla.\boldsymbol{u} = 0$) and weakly compressible flows ($\nabla.\boldsymbol{u} \approx 0$), this hypothesis has been used in many compressible flows and flows with variable density simulation. Recently, there have been a few studies on the importance of the bulk viscosity in compressible flow simulations (Chikitkin *et al.*, 2015; Cramer & Bahmani, 2014), and property variable flows (Hasan & Farouk, 2012). Chikitkin *et al.* (2015) studied the effect of bulk viscosity on the supersonic flow past spacecraft. Their results show that even small values of bulk viscosity $\mu_b/\mu \approx O(1)$ changes the structure of the shock wave. They observed that the shock thickness increases and that the obtained density profiles are closer to experiments. Hasan & Farouk (2012) used a set of analytical equations proposed by Onuki (2002) to calculate the bulk viscosity of near-critical CO_2 as a function of pressure and temperature (this set of equations are valid only for $T \geq T_{cr}$). They showed that near critical point ($P_0 = 73.8$ bar) the $\mu_b/\mu \approx O(10^4) - O(1)$ in temperature range of 304-314K. In this work, we use the same approach (Onuki, 2002) to compute the bulk viscosity for temperatures above the critical

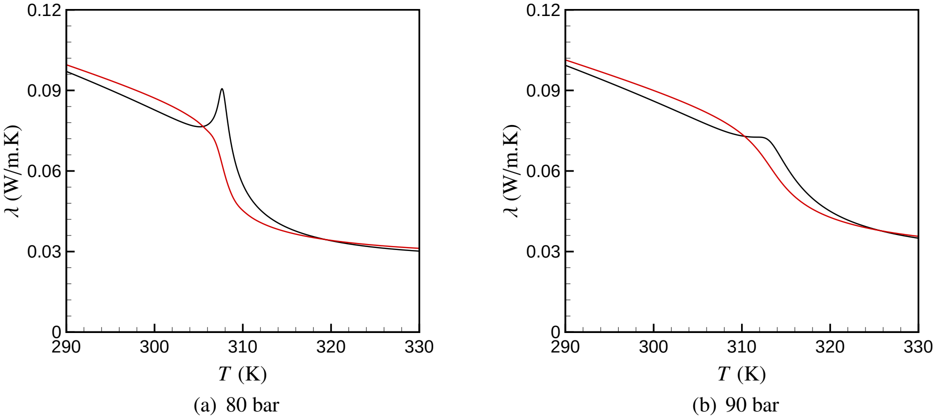

(a) 80 bar

(b) 90 bar

Figure 2.6: Variation of thermal conductivity of carbon-dioxide CO_2 with temperature T and pressure with different models. Black - NIST REFPROP database (Lemmon *et al.*, 2002) using model developed by Vesovic *et al.* (1990) for thermal conductivity; red - database of PROPATH version 13.1 (PROPATH Group, 1999).

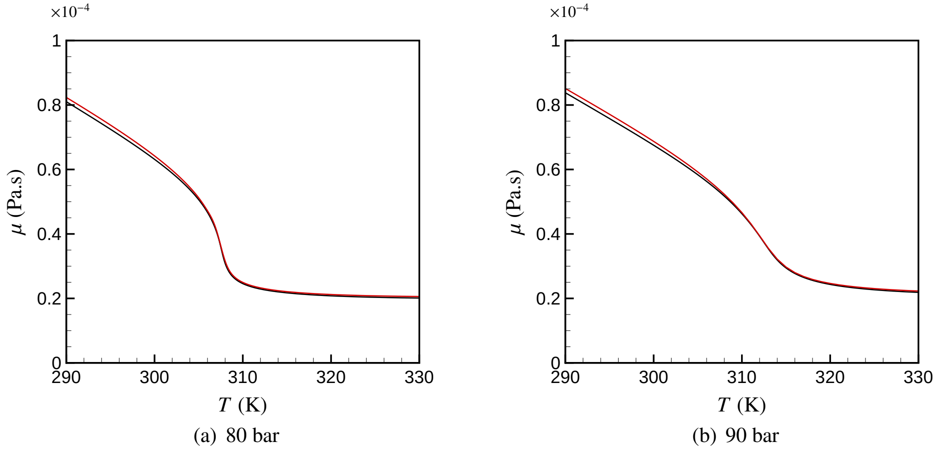

(a) 80 bar

(b) 90 bar

Figure 2.7: Variation of dynamic viscosity of carbon-dioxide CO_2 with temperature T and pressure with different models. Black - NIST REFPROP database (Lemmon *et al.*, 2002) using model developed by Fenghour *et al.* (1998) for viscosity; red - database of PROPATH version 13.1 (PROPATH Group, 1999).

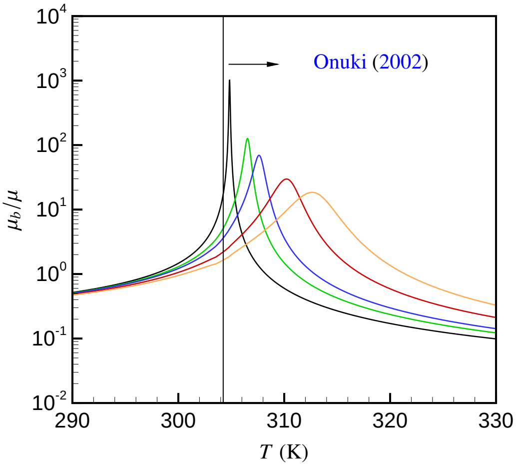

Figure 2.8: Variation of bulk viscosity of carbon-dioxide CO_2 with temperature T at different pressures. Orange - P_0= 74.5 bar; red - P_0= 75 bar; blue - P_0= 80 bar; green - P_0= 85 bar; black - P_0= 90 bar.

point $T \geq T_{critical}$ (right side of figure 2.8). To estimate the bulk viscosity at temperatures below the critical point $T < T_{cr}$ an analytical scaling is applied. As it can be seen, the bulk viscosity shows a similar behaviour as isobaric heat capacity and attains a peak at the pseudo-critical temperature, which tends to infinity at pressures close to the critical point. The simulations were performed using these results for the conditions discussed in chapter 3, however, no changes in heat transfer were observed. Therefore, for the results discussed in this thesis no bulk viscosity was considered. We expect that for conditions closer to the critical point, or for flows with stronger dilation the bulk viscosity will have stronger effects on the overall results.

2.6 Implementation of thermophysical properties of fluid in the computer program

In the previous sections, we introduced several equations of state and models for transport properties that can be used to approximate the real gas behaviour of fluids. Currently, the most accurate equations of state in the thermodynamic region close to the critical point are multi-parameter equations of state (Kunz & Wagner, 2012) and the relations for the viscosity and thermal conductivity are given in Fenghour *et al.* (1998) and Vesovic *et al.* (1990), respectively. These multi-parameter equations of state and the models for the transport properties are implemented in the NIST REFPROP database (Lemmon *et al.*, 2002) for pure fluids, pseudo-pure fluids (such as air), and mixtures with up to 20 components. In this work we use this database for the thermopyhsical properties of supercritical carbon-dioxide CO_2. Different properties of carbon-dioxide CO_2 as a function of enthalpy for different pressures P_0 are plotted in figure 2.9. Because the thermodynamic pressure is constant in time and space, the density, dynamic viscosity, thermal conductivity, etc. are tabulated as a function of enthalpy and then calculated using a third-order spline interpolation along an isobar line.

2.6.1 Computer program

The computer program that solves Eqs. (2.12)-(2.16) is written in Fortran 90 and parallelised using message passing interface (MPI) and the 2DECOMP&FFT library for two dimensional pencil decomposition (Li & Laizet, 2010). Figure 2.10 shows how the 3D pipe is partitioned in two dimensions.

Some operations performed in the simulations require the full sweep of data points in a specific direction. For instance, the derivatives in θ and z directions in the Poisson solver for pressure are calculated using forward-backward FFT algorithm. In order to evaluate these derivatives along a particular direction, we need the full sweep of the pencil decompositions of the data points in that direction. This is achieved as follows (see figure 2.10):

- transpose from r to θ: $A \rightarrow B$
- transpose from θ to z: $B \rightarrow C$
- transpose from r to z: $A \rightarrow B \rightarrow C$
- transpose from z to θ: $C \rightarrow B$
- transpose from z to r: $C \rightarrow B \rightarrow A$.

The simulations are preformed using 1152 (4 pencils in circumferential direction N_θ and 288 pencils in axial direction N_z) processors on 48 bullx B720 nodes on Cartesius surfsara (Dutch supercomputer). The time step for both inflow generator and developing pipe simulations was set to $\Delta t = 2 \times 10^{-5}$ and the corresponding maximum CFL number was 0.15. Statistics were sampled after 10 time units $5 \times 10^5 \Delta t$ for each simulation. The time-averages were taken over 20 time units, which correspond to 10 and 5 flow through times for simulations with $L = 30D$ and $L = 60D$, respectively. The samples were taken at an interval of 500 time steps.

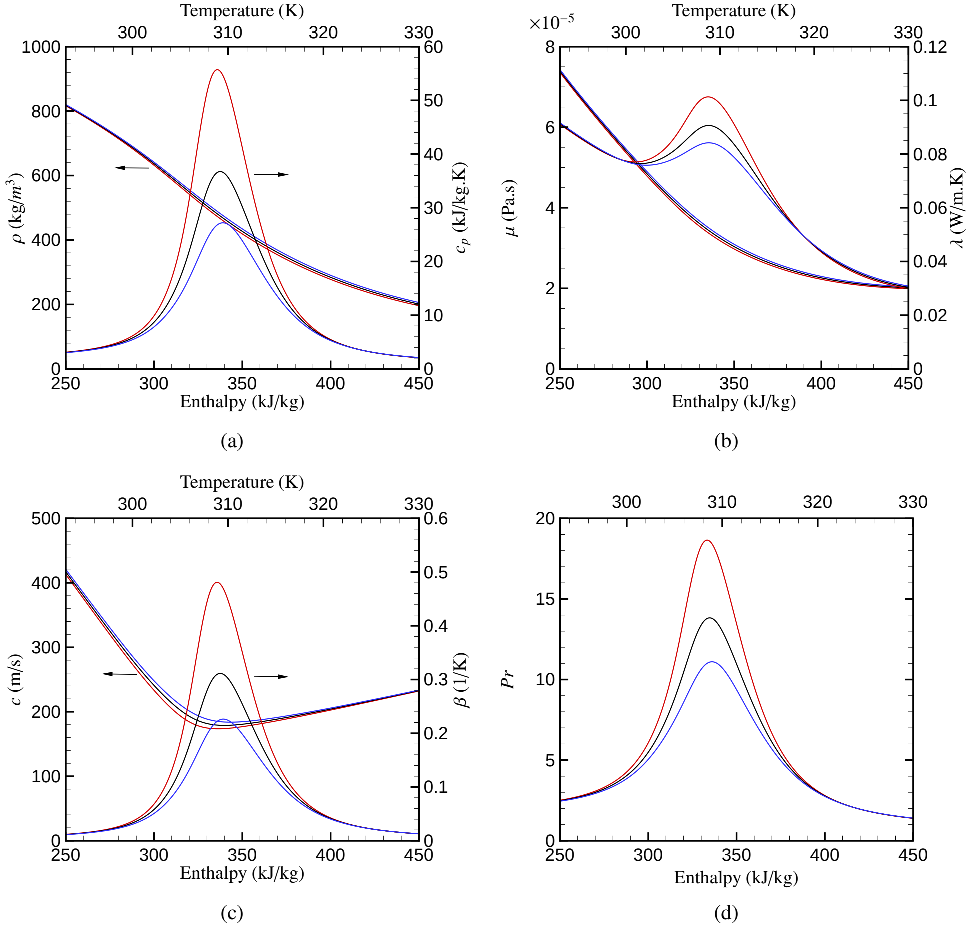

(a)

(b)

(c)

(d)

Figure 2.9: Property variations of carbon-dioxide CO_2 vs. enthalpy/temperature for pressures P_0 = 78, 80 and 82 bar based on NIST database (Lemmon *et al.*, 2002) (a) Density ρ and isobaric heat capacity c_p (b) Dynamic viscosity μ and thermal conductivity λ (—·—) (c) Speed of sound c and thermal expansion coefficient β(d) Prandtl numbers Pr. The peak of the heat capacity at constant pressure indicates the location of the pseudo-critical temperature T_{pc}; red - P_0 = 78; black - P_0 = 80; blue - P_0 = 82.

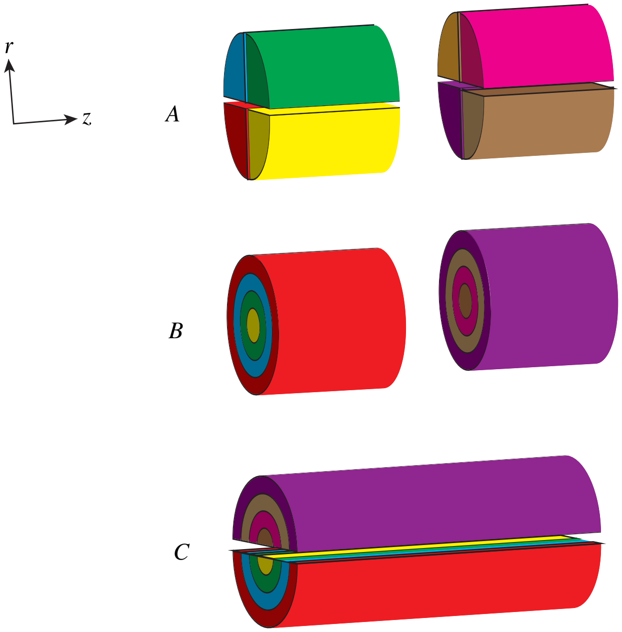

Figure 2.10: 2D decomposition of the geometry

3

Turbulent heat transfer flow at supercritical pressures

Part of the contents of this chapter appeared in:

Nemati, H., Patel, A., Boersma, B.J. & Pecnik, R.
Int. J. Heat Mass Tran., **83**, 741-752 (2015)
© Elsevier 2015
AND
Nemati, H., Patel, A., Boersma B.J. & Pecnik, R.
J. Fluid Mech., **800**, 531-556 (2016)
© Cambridge University Press 2016

DNS of heated turbulent pipe flows with a fluid at supercritical pressures are performed at a Reynolds number of $Re_{\tau 0} = 360$, in order to study the effect of buoyancy and large variations of thermophysical properties on turbulent statistics. A constant wall heat flux is applied and the temperature range within the flow domain incorporates the thermodynamic region where large variations in thermophysical properties occur. The contribution of these property variations on the mean flow is studied. As compared to ideal gas heat transfer, additional terms appear in the mean flow governing equations. These terms can significantly affect the energy balance because they modify the averaged wall heat flux and the enthalpy diffusion close to the pipe wall. Furthermore, the averaged thermophysical properties, especially the isobaric heat capacity c_p, deviate significantly from those evaluated using the mean temperature or enthalpy. This is due to an averaging artefact called the Jensen inequality, caused by the enthalpy fluctuations and the non-linear dependence of thermophysical properties with respect to the enthalpy. Turbulent statistics for different forced convection and mixed convection cases with the upward/downward flow are discussed. A decrease in turbulent kinetic energy is observed for the forced convection and the low buoyancy case, which causes heat transfer deterioration indicated by high wall temperatures. For the moderate and high buoyancy cases, the turbulence activity first reduces (heat transfer deterioration) and then increases due to turbulence recovery. In the case of downward flow, turbulence activity continuously increases, which results in enhancement of heat transfer for the entire pipe. Turbulent statistics are reported to highlight the effect on the observed wall temperature distribution and related heat transfer mechanisms.

3.1 Introduction

It was shown that fluids at supercritical pressure do not undergo a distinct liquid to gas phase transitions when heated from a liquid state. However, the continuous transition form a liquid-like to a gas-like phase still exhibits significant deviations from ideal gas behaviour. During the continuous transition the thermophysical properties of the fluid vary significantly within a narrow temperature range across the pseudo-critical temperature (T_{pc}). Experimental and previous numerical studies of heat transfer characteristics of flows at supercritical pressure have shown that these large thermophysical property variations alter the conventional behaviour and statistical properties of turbulence and turbulent heat transfer. Yoo (2013) presented a comprehensive review of turbulent flows at supercritical pressure and their characteristics. A detailed turbulent statistics containing second-order moments for Reynolds stresses and turbulent heat flux obtained from DNS using the low-Mach number approximation of the Navier-Stokes equations are given in Bae *et al.* (2005, 2008). Fully compressible DNS of turbulent mixing layers with supercritical fluids are given in Taskinoglu & Bellan (2010); Masi *et al.* (2013). The effect of viscosity fluctuations on the turbulent kinetic energy budgets in heated boundary layers with temperature dependent viscosity was studied by Lee *et al.* (2013) using DNS. They found that the turbulence energy increases near the wall due to enhanced energy transfer

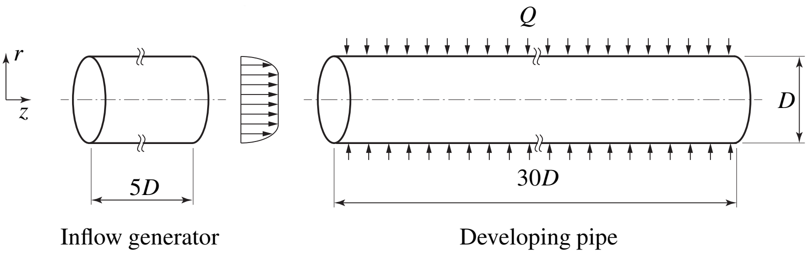

Figure 3.1: Geometry of the simulation domain.

via additional diffusion-like terms caused by viscosity stratification. The role of turbulent statistics due to viscosity and thermal conductivity fluctuations in an isothermal compressible flow were discussed by Huang *et al.* (1995).

The objective of this chapter is to further investigate the turbulent heat transfer mechanisms to supercritical fluids in pipe flows using detailed turbulent flow statistics. The simulation conditions correspond to different forced and mixed convection cases in upward and downward flows. We discuss turbulent statistics, not discussed previously, such as turbulent shear stress, radial turbulent heat flux, turbulent kinetic energy and its production rates (shear and buoyant production). Additionally, we show the interaction of highly non-linear thermophysical property variations (viscosity μ, thermal conductivity λ, isobaric heat capacity c_p and density ρ) with turbulent fluctuations in the flow field. These interactions generate additional second-order moments related to the viscosity-velocity-gradients and thermal conductivity-temperature-gradients in the mean flow governing equations. We show that these correlations significantly alter the mean enthalpy distribution (and the related temperature) within the flow field and the resulting mean enthalpy at the wall. We further show that the properties evaluated at the mean enthalpy strongly deviate from their corresponding Reynolds or Favre averaged mean value. This can be explained using the Jensen inequality. These findings can help to improve present turbulence models, which currently fail to predict turbulent heat transfer to fluids at supercritical pressures (He *et al.*, 2008*a*).

3.1.1 Flow domain, boundary and simulation conditions

The simulation setup for the supercritical fluid heat transfer simulations consists of two parts, namely the inflow generator and the simulation of the developing pipe flow Figure 3.1 (discussed in chapter 2).

A periodic adiabatic pipe flow simulation with a pipe length equal to five times the pipe diameter ($L/D = 5$) and a bulk Reynolds number of $Re_b \approx 5300$ is used to generate the inflow condition for the developing pipe. The mesh has a resolution of 126×288×288 points along the radial (r), circumferential (θ) and axial direction (z), respectively. The mesh for developing pipe is 126×288×1728 and has a length of $L/D = 30$. Two simulations have been done for longer pipe with the length of $L/D = 60$ and mesh of

Table 3.1: Flow conditions for the supercritical fluid flow simulations

Case	Type	Flow dir.	L/D	Ri_0	Q
A	Forced	-	30	0	2.4
B	Mixed	up	30	9.96	2.4
C	Mixed	up	30	79.67	2.4
D	Mixed	up	30	268.89	2.4
E	Mixed	down	30	99.59	2.4
F	Forced	-	30	0	4.8
G	Mixed	up	30	48.94	4.8
A_{60}	Forced	-	60	0	2.4
C_{60}	Mixed	up	60	79.67	2.4

126×288×3456. A uniform grid spacing is used in the axial and circumferential directions, while the radial grid is non-uniform and finer close to the wall. The corresponding grid resolutions for the dynamic scales are $0.55 \text{ (wall)} \leq \triangle r^+ \leq 4.31 \text{ (centre)}$, $(D/2\triangle\theta)^+ = 3.93$ and $\triangle z^+ = 6.25$ in wall units based on $Re_\tau = 360$. Nine cases with different buoyancy values, pipe lengths and flow directions are simulated. For all simulations the inflow conditions correspond to $P_0 = 80$ bar and $T_0 = 301.15$ K; table 3.1 summarises the flow conditions in terms of non-dimensional parameters.

3.2 Validation cases

The numerical scheme developed in this work is validated for four cases. These correspond to one fully developed adiabatic pipe (no heating), one developing and two fully developed pipe flows with constant heat flux. The root-mean-square (rms) velocity profiles are shown in Figure 3.2 and compared with the data from Wu & Moin (2008). An excellent agreement is obtained with a mesh that is almost twice as coarse in each direction as compared to the mesh used by Wu & Moin (2008) (256×512×512 grid points). The developing heated pipe flow is validated using experimental results of Shehata & McEligot (1998) for a strongly heated air flow with strong properties variations. The case used in this work corresponds to Run635 ($Re_b = 6025$ and $q = 0.0035$) in Shehata & McEligot (1998). The constitutive relations for the thermophysical properties are based on Perkins & McEligot (1975). Figure 3.3 shows the comparison of the temperature distribution along the pipe wall. A good agreement with the experimental data is obtained. The comparison of the radial temperature profile with the experiments at three different cross-sections is shown in Figure 3.4, again showing good agreement.

The two fully developed turbulent pipe simulations with constant heat flux are validated using experimental data for upward mixed convection of air as given in

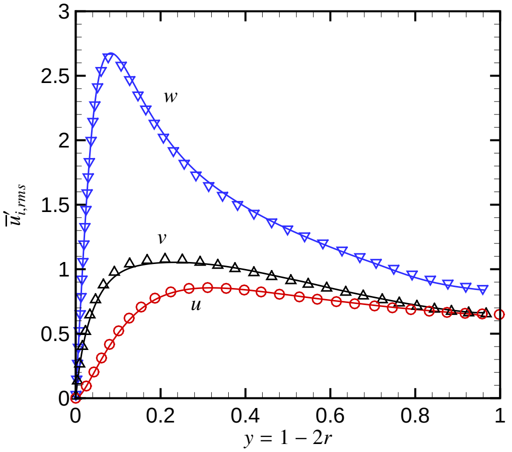

Figure 3.2: Root-mean-square velocity fluctuations for the inflow generator. Lines - present study; symbols - Wu & Moin (2008).

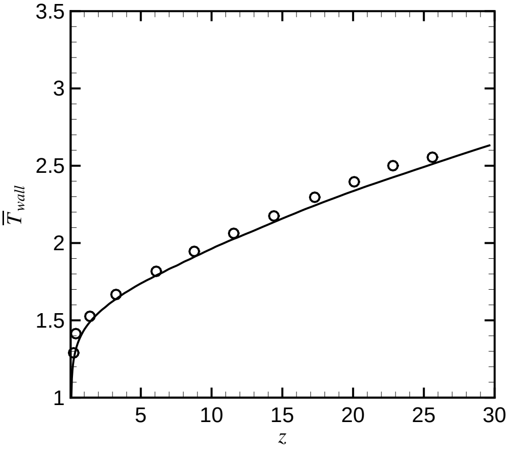

Figure 3.3: Wall temperature distribution for the developing strongly heated pipe flow. Lines - present study; symbols - Shehata & McEligot (1998).

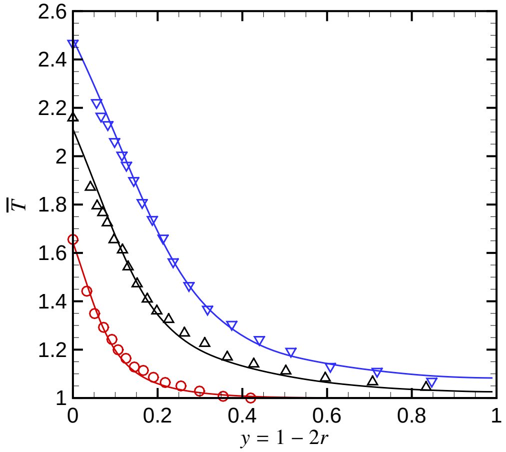

Figure 3.4: Radial temperature profiles at three streamwise locations. Lines - present study; symbols - Shehata & McEligot (1998); red - $z = 3.2$; black - $z = 14.2$; blue - $z = 24.5$.

Carr *et al.* (1973). The cases considered are N11 with $Re_b = 5300$ and $Gr = 22.4 \times 10^6$ and N13 with $Re_b = 5000$ and $Gr = 15.3 \times 10^6$. For both cases the Prandtl number is $Pr = 0.71$. Figures 3.5 and 3.6 shows the comparison of the streamwise velocity and the total heat flux profile for cases N11 and N13. Also here a good agreement is observed for both cases.

3.3 Supercritical heat transfer results and discussion

In the results discussed, the mean quantities are obtained by taking a statistical average over time and the homogeneous circumferential direction using Reynolds and Favre averaging. Velocity components and enthalpy are Favre averaged (mass weighted), whereas pressure, density and transport properties are Reynolds averaged. For a generic variable γ, Reynolds averaged mean $\overline{\gamma}$ and its fluctuation γ' are defined as $\gamma = \overline{\gamma} + \gamma'$, with $\overline{\gamma'} = 0$. Favre averaged mean $\tilde{\gamma}$ and its fluctuation γ'' are defined as $\gamma = \tilde{\gamma} + \gamma''$, with $\tilde{\gamma} = \overline{\rho\gamma}/\overline{\rho}$, $\overline{\gamma''} = -\overline{\rho'\gamma'}/\overline{\rho} \neq 0$ and $\overline{\rho\gamma''} = 0$.

The bulk quantities, such as bulk enthalpy h_b and bulk velocity U_b, are computed based on mass and energy conservations as follows:

$$h_b = \int_0^R \overline{\rho w h r} dr \Big/ \int_0^R \overline{\rho w} r dr, \tag{3.1}$$

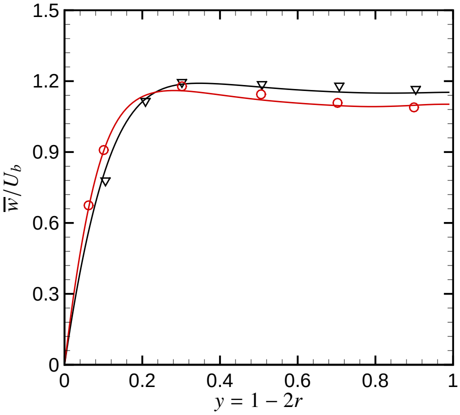

Figure 3.5: Streamwise velocity profiles $\overline{w}/U_b$ for the fully developed heated upward pipe flow. Lines - present study; symbols - Carr *et al.* (1973); red - case N11; black - case N13.

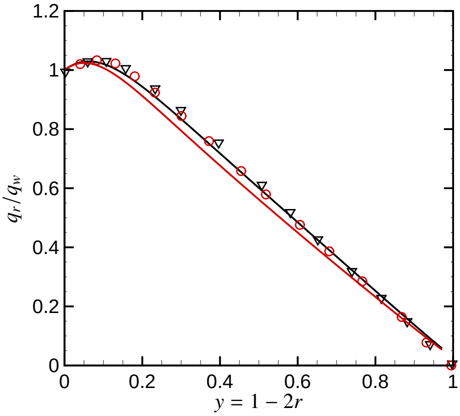

Figure 3.6: Total radial heat flux q_r/q_w for the fully developed heated upward pipe flow. Lines - present study; symbols - Carr *et al.* (1973); red - case N11; black - case N13.

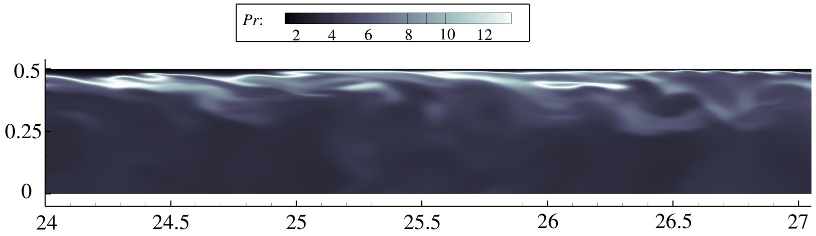

Figure 3.7: Instantaneous Pr number contour in the $r-z$ plane at a downstream location for case A.

$$U_b = \int_0^R \overline{\rho w} r dr / \rho_b. \tag{3.2}$$

Bulk density ρ_b and T_b are calculated using h_b via interpolation from the table.

3.3.1 Bulk quantities and statistical averages

The influence of different mesh resolutions has been studied in this section. The mesh resolution for the inflow generator is clearly sufficient to resolve the smallest turbulent structures, as discussed earlier in Figure 3.2. For the heated pipe flow with CO_2 above its critical pressure, the thermal scales are expected to be smaller than the Kolmogorov length scale, since the Prandtl number $Pr > 1$ (figure 2.9(d)). Figure 3.7 shows a Prandtl number contour plot for case A at one time instant. As stated earlier, the Prandtl number at the inlet is $Pr_0 = 3.19$, whereas very close to the wall it is approximately unity. In a very thin region away from the wall, where the enthalpy corresponds to the pseudo-critical value, the Prandtl number exhibits a maximum value of 14. For most of the remaining flow $Pr \approx 4$. Therefore, the radial mesh distribution has been kept constant until $y^+ \leq 30$ where the flow, depending on streamwise location, crosses the pseudo-critical point. Based on Tennekes & Lumley (1972), the relation between the smallest velocity scales η and the thermal structures η_θ is given as $\eta_\theta = \eta / \sqrt{Pr}$. Thus, the mesh resolution should be approximately twice–and at the location of the pseudo-critical temperature four times–as fine as required to resolve the velocity field. The mesh resolution in terms of the Kolmogorov η and thermal scales η_θ is shown in figure 3.8, where it can seen that the Kolmogorov scales are well resolved in all directions (lines with symbols). The resolution for the thermal scales (lines) is $0.5 < \Delta y/\eta_\theta < 2.8$ in the wall-normal direction, $0.2 < \Delta(r\phi)/\eta_\theta < 9$ in the circumferential direction and $4 < \Delta x/\eta_\theta < 15$ in the streamwise direction. The local maxima of the lines correspond to the locations of the pseudo-critical point, where the spatial resolution indicates that the thermal scales are slightly under-resolved. A comparable mesh resolution has been used by Lee *et al.* (2013) and Zonta *et al.* (2012). For example, the mesh resolution used by Lee *et al.* (2013) is $0.599 < \Delta y/\eta_\theta < 2.99$ in wall-normal direction, $\Delta z/\eta_\theta = 7.9$ in spanwise direction and $\Delta x/\eta_\theta = 12.4$ in streamwise direction. Thus, we expect the mesh resolution to capture all the relevant scales.

To quantify this, a simulation with a coarser mesh of 120×128×1536 points was performed. In comparison, the mesh size for the same domain size used in Bae *et al.* (2005) is 68×128×768 in radial, circumferential and axial direction, respectively. The results of both meshes are compared in terms of averaged streamwise wall temperatures and radial turbulent heat fluxes in Figures 3.9 and 3.10, respectively. It can be seen that the differences are negligible.

As mentioned before, the speed of sound abruptly decreases in the supercritical region (see Figure 2.9(c)); therefore, the applicability of the low-Mach number approximation should be examined. Figure 3.11 shows the variation of inlet Mach number with increasing of pipe diameter for thermodynamic pressure P_0 =80 bar; $M = U_b^*/c^*$ where $U_b^* = Re_b\mu^*/(\rho^* D^*)$. As it can be seen, for pipes with $D^* \geq 1mm$, which is the application diameter of authors interest (see Jiang *et al.* (2008); Zhang *et al.* (2012)), the Mach number is $\mathcal{O}(10^{-3})$. Figure 3.12 shows the instantaneous Mach number contour plot for case A for $D^* = 1mm$. It shows that the low-Mach number approximation also preserves in downstream, where the speed of sound has the lowest value.

Based on Morkovin's hypothesis the compressibility effects are mainly due to the variable property effect and the turbulence structures of compressible boundary layers closely follow the incompressible pattern as long as the ratio of the root-mean-square density fluctuations to the mean density $\rho'_{rms}/\overline{\rho}$ is small (Morkovin, 1962; Bradshaw, 1977). This hypothesis is also extensively approved in the study of wall-bounded compressible turbulent flow. Figure 3.13 shows the profiles of enthalpy fluctuations $h''_{rms} = \sqrt{\overline{\rho h'' h''}/\overline{\rho}}$ and thermophysical property fluctuations for case A at $z = 15$. All thermophysical property fluctuations show the similar profile to enthalpy fluctuations. As can be seen, the root-mean-square density, viscosity and α reach the maximum of 35, 32 and 52%, respectively, of the local mean quantities. These large-density fluctuations show the inapplicability of Morkovin's hypothesis turbulent heat transfer at supercritical pressures (Morkovin, 1962). Note, this hypothesis may be valid at supercritical pressures much higher than critical pressures, where the thermophysical properties are less dependent on temperature and pressure.

Figure 3.14 shows the comparison of the wall temperature profiles between present DNS and that of Bae *et al.* (2005) for the six corresponding cases (case E corresponds to case F of Bae *et al.* (2005)). The forced convection (case A) provides a good match with Bae *et al.* (2005), but the agreement for the mixed convection cases is poor. However, the physical trend between the present results and that of Bae *et al.* (2005) is similar. For small buoyancy effects (case B), the heat transfer deterioration is higher (as seen by the higher wall temperature) than that of the forced convection (case A). By increasing the buoyancy effect (case C), the wall temperature increases until approximately $z = 13$ and then decreases as a result of turbulence recovery, while this recovery starts earlier ($z = 9$) for larger buoyancy (case D). In downward flow (case E), there is an immediate recovery

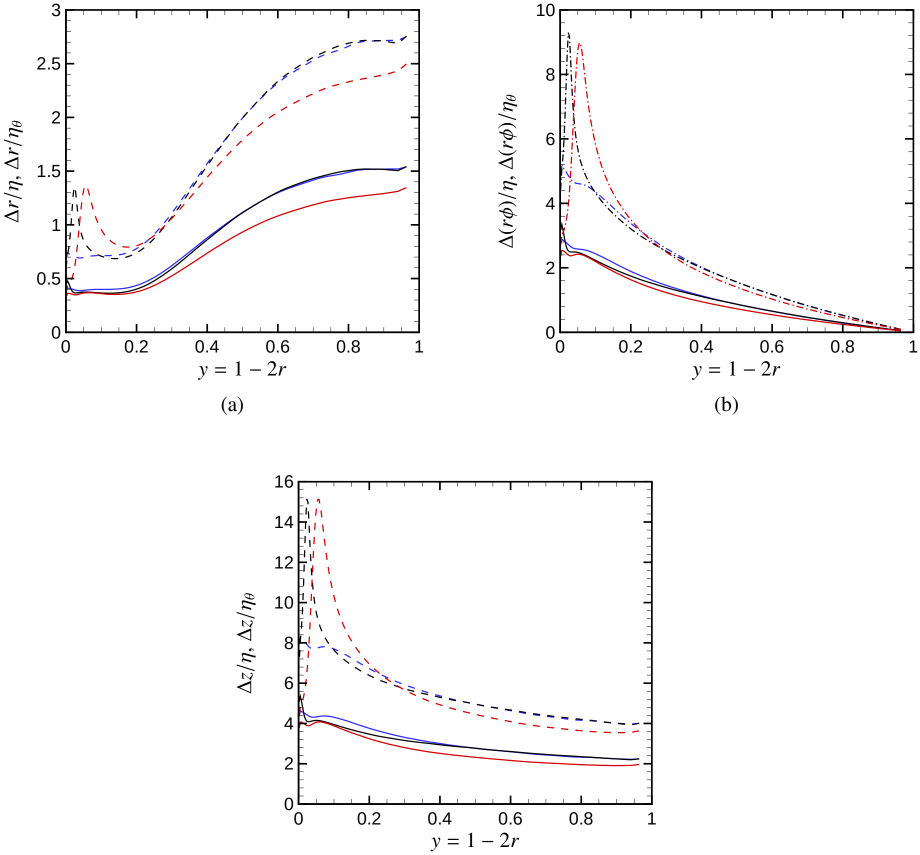

(a)

(b)

(c)

Figure 3.8: Spatial resolution normalized by Kolmogorov scale (solid lines) and thermal scales $\eta_\theta = \eta/\sqrt{Pr}$ (dashed lines), (a) radial, (b) circumferential and (c) streamwise resolution for case A. Blue - $z = 0$, black - $z = 5$, red - $z = 20$.

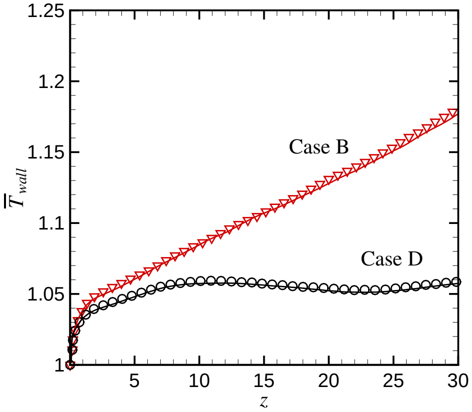

Figure 3.9: Averaged temperature along the pipe wall for cases B and D with two different resolutions. Lines - 126×288×1728; symbols - 120×128×1536.

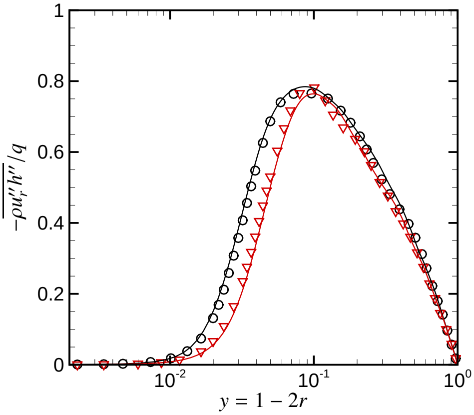

Figure 3.10: Turbulent radial heat flux profile for case B. Lines - 126×288×1728; symbols - 120×128×1536; black - $z = 7.5$; red - $z = 15$.

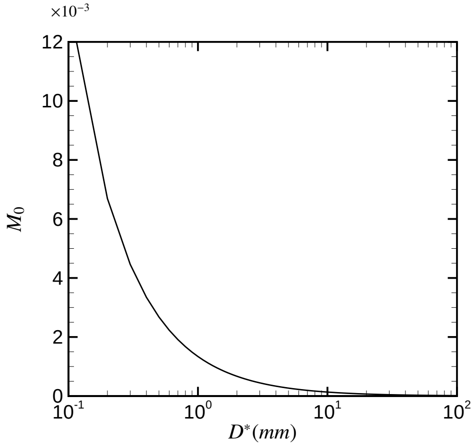

Figure 3.11: Variation of inlet Mach number (M_0) with the diameter of pipe at $Re_{\tau 0} = 360$.

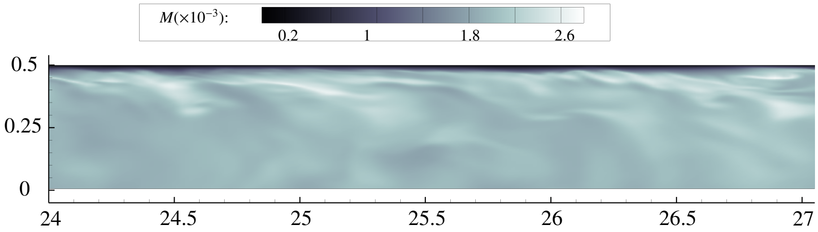

Figure 3.12: Instantaneous M number contour in the $r - z$ plane at a downstream location for case A with $D^* = 1mm$.

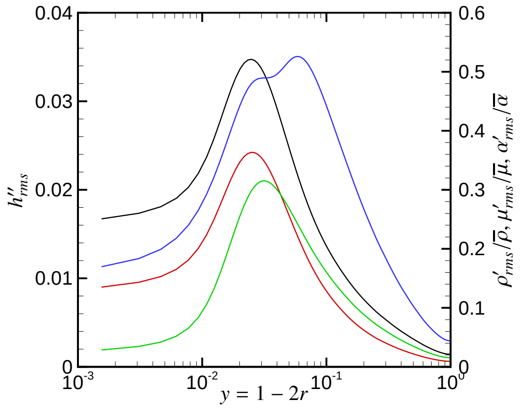

Figure 3.13: Distribution of local enthalpy fluctuations and thermophysical properties fluctuations for case A at $z = 15$. Black - h''_{rms}; red - $\rho'_{rms}/\overline{\rho}$; green - $\mu'_{rms}/\overline{\mu}$; blue - $\alpha'_{rms}/\overline{\alpha}$.

at $z = 1$ and the wall temperature distributions is almost constant after the recovery. It is seen that the wall temperature is lower compared to corresponding upward flows (case C). For case G, which is imposed by higher wall heat flux, the variation of wall temperature is stiffer than other cases. However, the wall temperature experiences a sudden recovery at $z = 13$ and reaches almost constant values. The results of Bae *et al.* (2005) show a higher deterioration for case B and the onset of heat transfer recovery is slightly earlier for cases C and D. The wall temperature of case G is comparable with Bae *et al.* (2005) in deterioration part, while larger inconsistency appears in the recovery region. Note, the main differences between the present DNS and that of Bae *et al.* (2005) are mesh resolution, time step (approximately 65 times smaller time-step in this work), fluid property databases (PROPATH Group (1999) in their work) and numerical schemes.

The distributions of streamwise average wall temperature along the pipe with length of $L/D = 60$ are plotted in figure 3.15. As it can be seen, for case A_{60} the slope of wall temperature $\partial\overline{T}_{wall}/\partial z$ decreases toward the end of pipe. Case E_{60}, exhibits a secondary deterioration after recovery, which starts at $z = 38$.

Figure 3.16(a) shows the distribution of bulk enthalpy in streamwise direction for all cases. Based on the overall energy conservation, for cases with constant wall heat flux, the distribution of the bulk enthalpy increases linearly as a function of z, namely $h_b = 4Qz/Re_{b0}Pr_0$. As it is expected, the bulk enthalpy computed from DNS data follows a linear profile with a slope of $h_b = 4Q/Re_{b0}Pr_0$, which verifies the conservation of energy. Unlike the bulk enthalpy h_b, the bulk temperature distribution exhibits a concave profile, which is more obvious for cases F and G. This non-linear behaviour stems from the non-linear trend of c_p via the expression $c_p = (\partial h/\partial T)_P$. Figures 3.16(c)

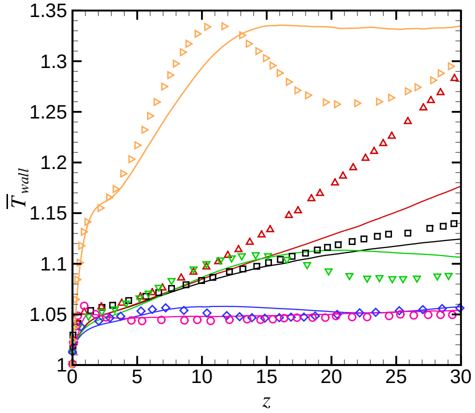

Figure 3.14: Comparison of streamwise average wall temperature along the pipe with the results of Bae *et al.* (2005); Lines - present work; symbols - Bae *et al.* (2005); black- case A; red - case B; green - case C; blue - case D; pink - case E; orange - case G.

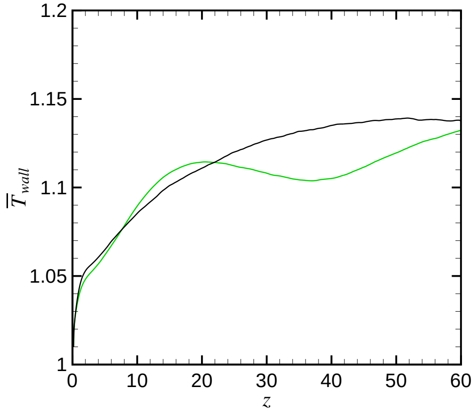

Figure 3.15: Distribution of streamwise average wall temperature along the pipe with length of $L/D = 60$. Black - case A_{60}; green - case E_{60}.

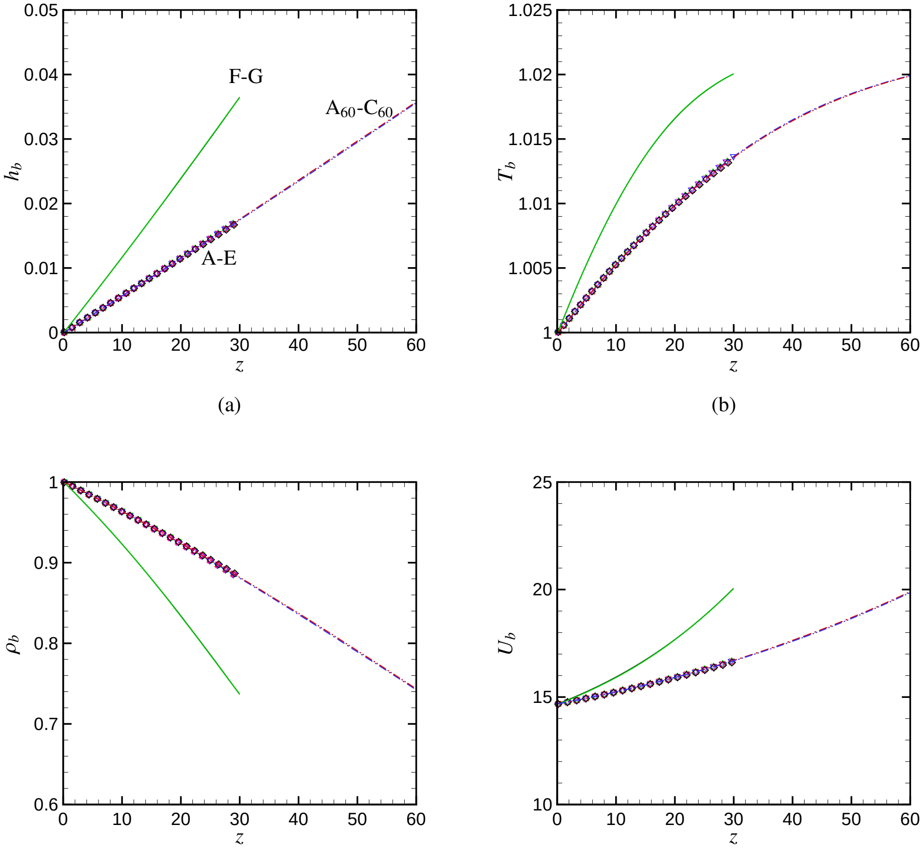

(a)

(b)

(c)

(d)

Figure 3.16: (a) bulk enthalpy h_b, (b) bulk temperature T_b, (c) bulk density ρ_b and (d) bulk velocity U_b.

and 3.16(d) show the streamwise distributions of bulk density and velocity, respectively. As discussed before, because of thermal expansion (reduction of bulk density in figure 3.16(c)), a flow acceleration occurs, which results in increasing bulk velocity (figure 3.16(d)). Note, the slope of the bulk velocity distribution is increasing. The reason is that the bulk temperature approaches the pseudo-critical temperature ($T_{pc} = 1.021$) where the relation between density and temperature is highly non-linear.

Next, we examine the effects of thermal expansion and buoyancy force on mean streamwise velocity and mean enthalpy. In the forced convection case (A), as clearly shown in figure 3.17(a), a flow acceleration due to thermal expansion occurs near the wall such that the velocity profile becomes fuller. Further downstream, as fluid continuously heated, the thermal expansion spreads towards the core region, which results in increasing streamwise velocity ($z = 15, 22.5$). In case B (upward flow with low buoyancy), as shown in figure 3.17(b), the flow acceleration is higher at near-wall region, because of the combined influence of the buoyancy force and thermal expansion; buoyancy force favours the flow acceleration. It can be seen that with increasing buoyancy, such as cases C and D, the velocity distribution deforms to an M-shape profile across the pipe, where $\partial\tilde{w}/\partial r > 0$ in the core flow. The formation of M-shaped velocity profiles in the upward flow cases, reduces the tendency towards heat transfer deterioration, as will be discussed later. In the case of downward flow, the buoyancy force is against the flow direction and due to lower flow acceleration in the near-wall, higher turbulence levels are maintained.

In the following, we briefly examine the changes in temperature profiles for different cases (figure 3.18). Although the thermal wall boundary condition is the same for all cases in this figure, the temperature distributions are different. The temperature is continuously increasing along the pipe for cases A and B with a larger streamwise temperature gradient for case B ($\partial\overline{T}/\partial z|_B > \partial\overline{T}/\partial z|_A$ more obvious in the near-wall region). This is in agreement with the wall temperature distributions discussed in figure 3.14. In the case of moderate buoyancy (case C), near-wall fluid is heated to the highest temperature ($\overline{T}_{wall} = 1.11$) at $z = 20$ and then it decreases farther downstream, while in the core region it is monotonically increasing. A similar behaviour is observed for case D (high buoyancy), except that the near wall temperature increases until $z = 11$ and then decreases farther downstream. Compared to forced convection and upward flows, in downward flow (case E) the temperature profile at the near-wall shows small changes, but the temperature in the core region is increasing, which is because of continuously transferred heat to the core region.

3.3.2 Turbulent statistics

The statistical analysis of DNS data helps to clarify the role of dynamical characteristics of turbulence and buoyancy on mean quantities. The Favre/Reynolds averaged equations are given as

$$\frac{\partial\overline{\rho}\tilde{u}_i}{\partial x_i} = 0, \tag{3.3}$$

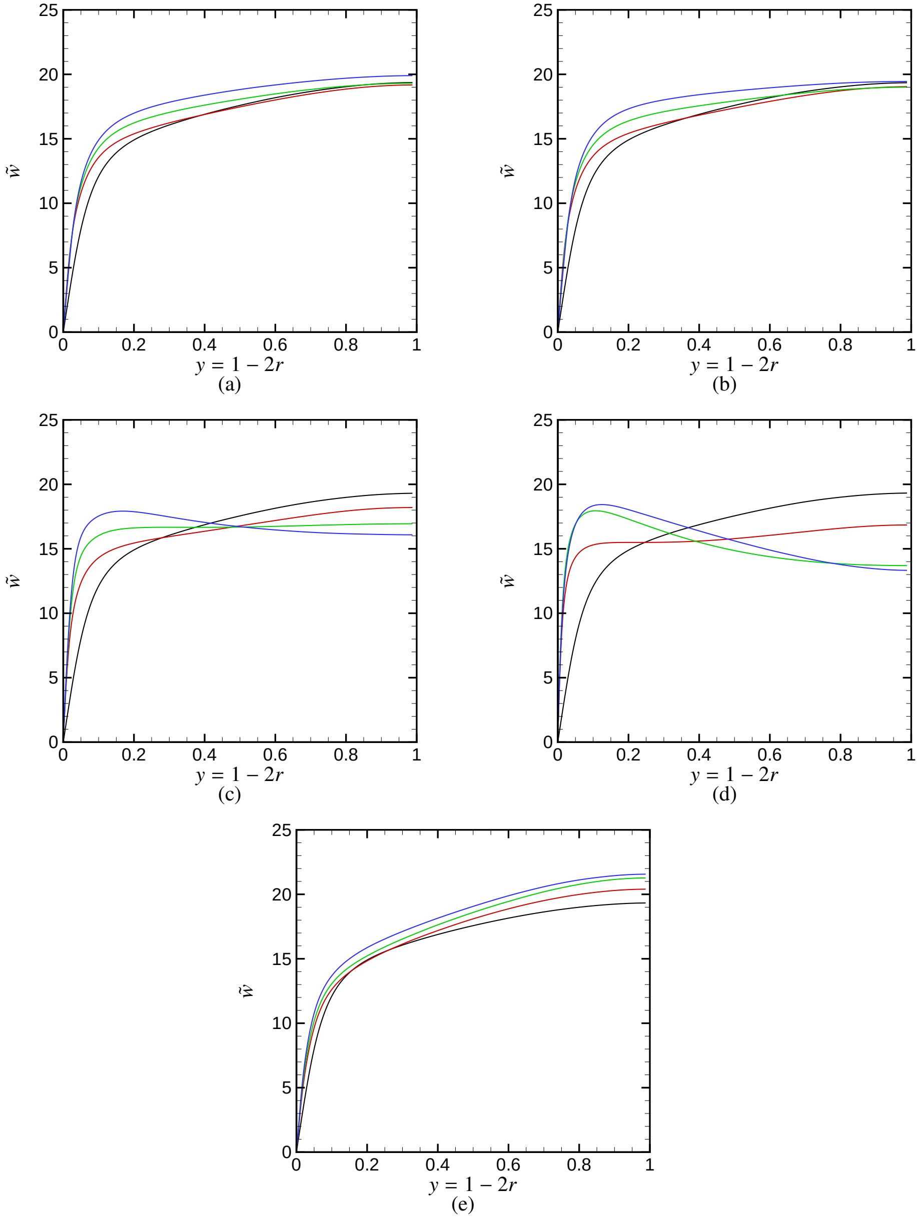

(a) (b) (c) (d) (e)

Figure 3.17: Streamwise velocity profile at different down-stream locations (a) case A, (b) case B, (c) case C, (d) case D, (e) case E. Black - $z = 0$; red - $z = 7.5$; green - $z = 15$; blue - $z = 22.5$.

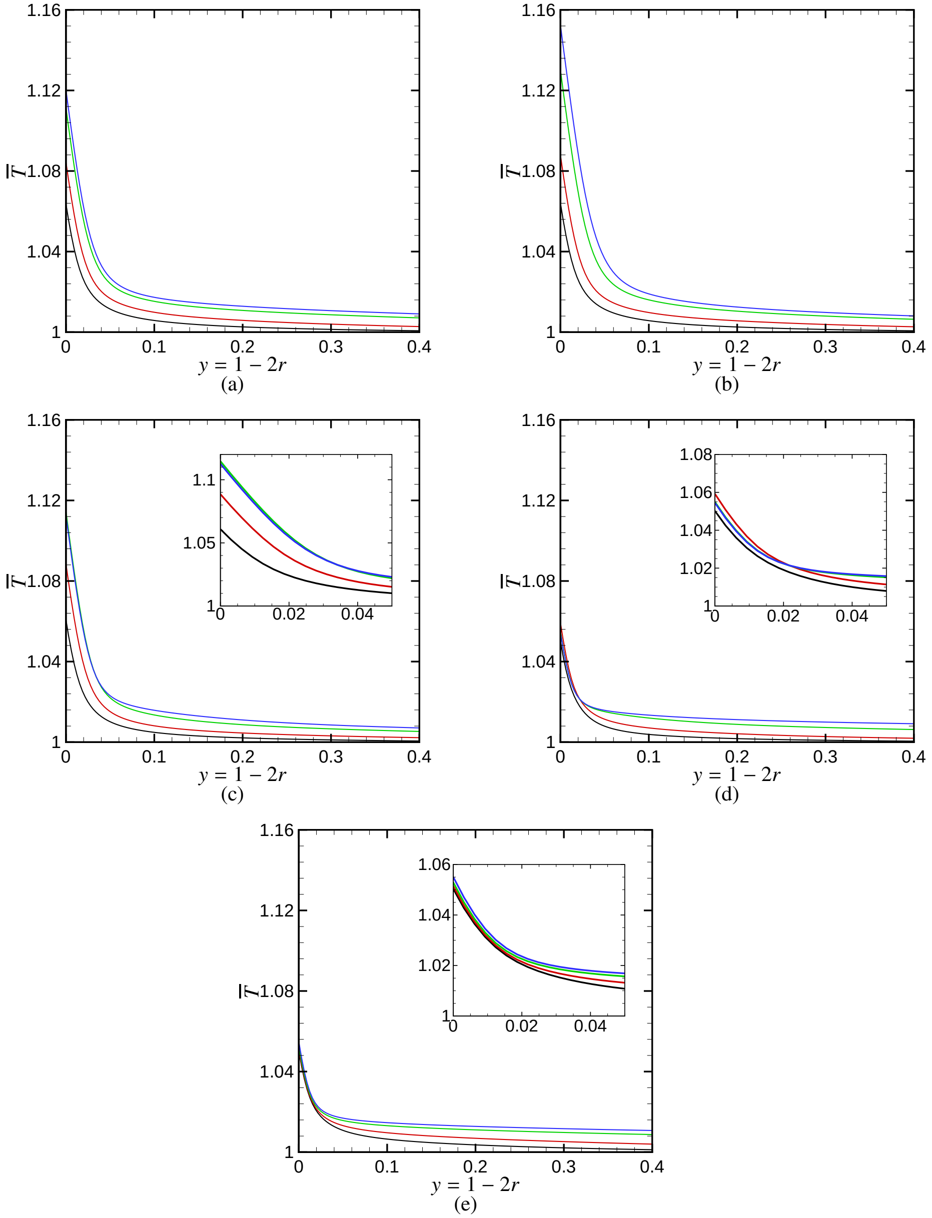

(a) (b) (c) (d) (e)

Figure 3.18: Temperature profile at different down-stream locations (a) case A, (b) case B, (c) case C, (d) case D, (e) case E. Black - $z = 5$; red - $z = 11$; green - $z = 20$; blue - $z = 25$.

$$\frac{\partial \overline{\rho}\tilde{u}_i\tilde{u}_j}{\partial x_j} = -\frac{\partial \overline{p}}{\partial x_i} + \frac{1}{Re_{\tau 0}}\frac{\partial \overline{\tau}_{ij}}{\partial x_j} - \frac{\partial \overline{\rho u_i'' u_j''}}{\partial x_j} \mp \overline{\rho} Ri_0 \delta_{i3}, \tag{3.4}$$

$$\frac{\partial \overline{\rho}\tilde{u}_i\tilde{h}}{\partial x_i} = -\frac{1}{Re_{\tau 0} Pr_0}\frac{\partial \overline{q}_i}{\partial x_i} - \frac{\partial \overline{\rho u_i'' h''}}{\partial x_i}, \tag{3.5}$$

where

$$\overline{\tau}_{ij} = 2\overline{\mu}\tilde{S}_{ij} + 2\overline{\mu' S''_{ij}} + 2\overline{\mu}\overline{S''}_{ij}, \tag{3.6}$$

and

$$\overline{q}_i = -\overline{\alpha}\frac{\partial \tilde{h}}{\partial x_i} - \overline{\alpha}\frac{\partial \overline{h''}}{\partial x_i} - \overline{\alpha'\frac{\partial h''}{\partial x_i}}. \tag{3.7}$$

As compared to ideal gas fluids with constant transport properties the momentum and energy equations contain additional terms. Note, that the terms $2\overline{\mu}\overline{S''_{ij}}$ and $\overline{\alpha}\partial\overline{h''}/\partial x_i$ appear only due to Favre decomposition and are zero if Reynolds decomposition is applied for the diffusion terms ($\overline{\tau}_{ij} = 2\overline{\mu}\overline{S}_{ij} + 2\overline{\mu' S'_{ij}}$ and $\overline{q}_i = -\overline{\alpha}\partial\overline{h}/\partial x_i - \overline{\alpha'\partial h'/\partial x_i}$). It can be shown that $\overline{\alpha'\partial h'/\partial x_i} = \overline{\alpha'\partial h''/\partial x_i}$ and that $\overline{\alpha}\overline{h}/\partial x_i = \overline{\alpha}\tilde{h}/\partial x_i + \overline{\alpha}\overline{h''}/\partial x_i$. It is commonly assumed that $\overline{S''_{ij}}$, as well as $\overline{h''}$, are small in ideal gas flows. However, for flows at supercritical pressure this is not the case and $\overline{S''_{ij}}$ and $\overline{h''}$ are important in terms of turbulence modelling, wherein the mean governing equations are solved for $\tilde{u}_i$ and $\tilde{h}$ (hence the diffusion terms are a function of $\tilde{u}_i$ and $\tilde{h}$). Modelling requirements of $\overline{\gamma''}$ for isothermal compressible flows were also highlighted by (Huang *et al.*, 1995). The significance of these additional terms is discussed in section 3.3.3.

Following turbulent statistics are discussed: Reynolds shear stress $\overline{\rho u''w''}$, radial turbulent heat flux $\overline{\rho u''h''}$, turbulent kinetic energy and production rate of turbulent kinetic energy (both shear and buoyancy). Four streamwise locations are used to study the turbulent statistics, whereby the first streamwise location corresponds to the inlet condition. The inlet condition is used as a reference state to study the downstream development of the flow.

3.3.2.1 Case A

Case A represents the forced convection case, where figure 3.19 shows the Reynolds shear stress (a), the radial turbulent heat flux (b), the turbulent kinetic energy (c) and its shear production rate (d). As discussed in section 1.4, flow acceleration due to thermal expansion causes a decrease in turbulence. The decrease in turbulence is evident as the Reynolds shear stress, the turbulent kinetic energy and the production rate all decrease as one proceeds downstream. Interestingly, the DNS data for the turbulent heat flux in figure 3.19(b) show a constant peak at all locations, except at the inlet (where the heat flux is not active yet). This can be explained by means of the production of the radial turbulent heat flux $P_{\overline{\rho u''h''}} \propto -\overline{\rho u''u''}\partial\tilde{h}/\partial r$. As $\overline{\rho u''u''}$ decreases due to deterioration, $\partial\tilde{h}/\partial r$ increases, maintaining $P_{\overline{\rho u''h''}}$ nearly constant.

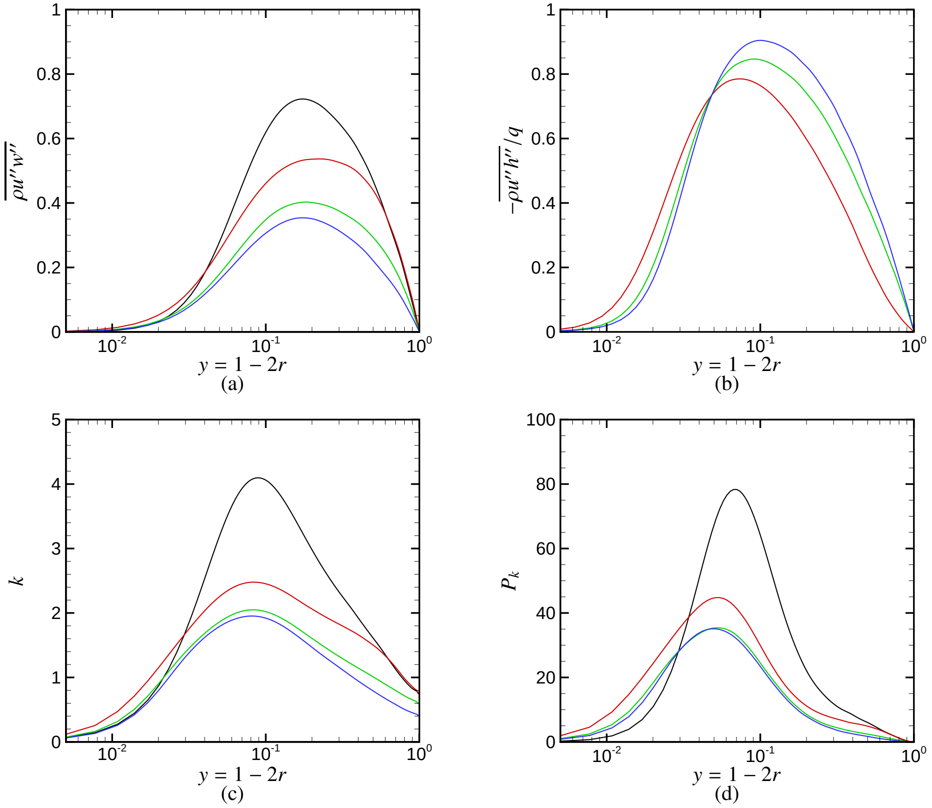

Figure 3.19: Evolution of Reynolds shear stress (a), turbulent heat flux (b), turbulent kinetic energy (c) and turbulent shear production rate (d) along the pipe for case A. Black - $z = 0$; red - $z = 7.5$; green - $z = 15$; blue - $z = 22.5$.

3.3.2.2 Case B

Case B represents an upward flow case with small buoyancy. Buoyancy in upward flows causes local flow acceleration, thereby decreasing the turbulence further as compared to the forced convection case. The recovery in heat transfer due to buoyancy is not observed within the simulated domain of $L/D = 30$. The DNS results for case B are shown in figure 3.20 for Reynolds shear stress (a), radial turbulent heat flux (b), turbulent kinetic energy (c), shear (d), buoyant (e) and total production (f) rate of turbulent kinetic energy. The results show the same trend as those in case A, but with a larger decrease in turbulence and hence higher wall temperature (higher heat transfer deterioration). Because of the structural effects of buoyancy, there is an additional source of turbulent kinetic energy production, namely buoyant turbulent kinetic energy production shown in figure 3.20(e). The buoyant production term is included in the mean pressure gradient in transport equation of turbulent kinetic energy, which is defined as follows (Canuto, 1997),

$$B_k = -\overline{w''}\frac{\partial \overline{p}}{\partial z}. \tag{3.8}$$

Using the hydrostatic equilibrium equation $\partial\overline{p}/\partial z = \mp\overline{\rho}g_z = \mp\overline{\rho}Ri_{0z}$ and the fact that $\overline{w''} = -\overline{\rho' w'}/\overline{\rho}$, buoyancy production reads

$$B_k = \mp Ri_{0z}\overline{\rho' w'}. \tag{3.9}$$

Because of a stably stratified density field (density close to the wall decreases in streamwise direction), the buoyancy production is negative and has the same sign as the turbulent dissipation. However, the buoyant production transfers the turbulent kinetic energy back to the mean flow. The value of the buoyant production is small as compared to the shear production rate in this case.

3.3.2.3 Case C

Case C represents an upward flow with moderate buoyancy. The flow undergoes both, deterioration and recovery. The DNS results for case C are shown in figure 3.21, again for Reynolds shear stress (a), radial turbulent heat flux (b), turbulent kinetic energy (c), shear (d), buoyant (e) and total production (f) rate of turbulent kinetic energy. Deterioration, followed by recovery of turbulence, can be observed in Reynolds shear stress, figure 3.21(a). In the deterioration region (until $z \approx 18$), the Reynolds shear stress decreases and becomes partially negative at locations slightly away from the wall and centreline. As z increases the negative portion of the Reynolds shear stress moves towards the centre of the pipe. At farther downstream locations ($z > 20$) the Reynolds shear stress is negative in most of the radial domain, except close to the wall where it remains positive. It corresponds to the location, where the recovery starts. The recovery onset closely follows the velocity profile, which deforms into an M-shape (external effects) as shown in figure 3.17(c). The turbulent heat flux also increases after the recovery onset. By comparing the turbulent heat flux until $z = 15$, it can be seen that the

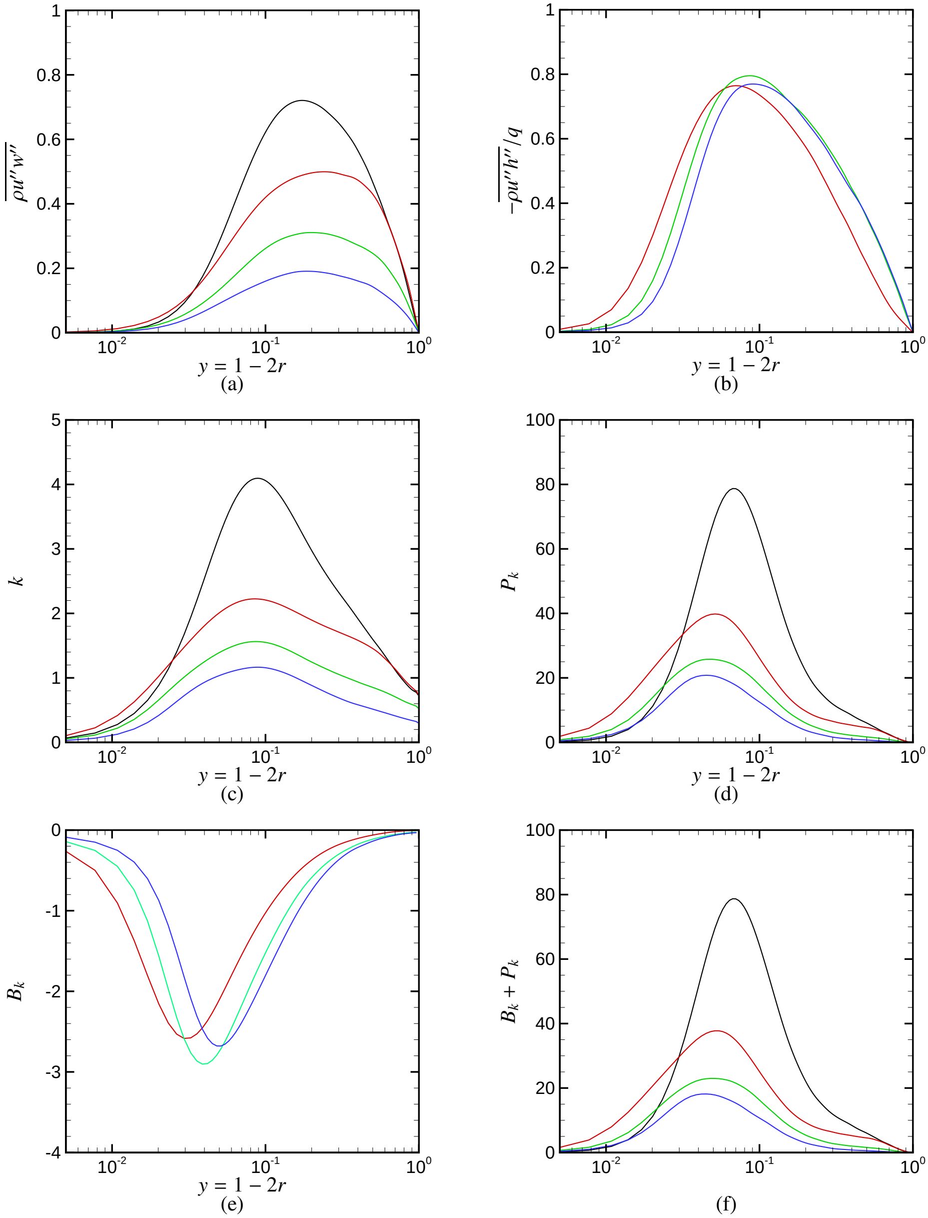

Figure 3.20: Evolution of Reynolds shear stress (a), turbulent heat flux (b), turbulent kinetic energy (c), shear (d), buoyant (e) and total production rate (f) along the pipe for case B. Black - $z = 0$; red - $z = 7.5$; green - $z = 15$; blue - $z = 22.5$.

values are almost identical, but it significantly increases thereafter. Figure 3.21(d) shows the shear production rate, which becomes slightly negative at $z = 22.5$. The reason for this is that the velocity gradient becomes zero and the Reynolds shear stress is small. The buoyancy production term in figure 3.21(e), unlike for case B, shows a positive value (structural effects), which reveals the presence of a locally unstable stratified density field (see section 1.4). When the shear production rate decreases to zero ($z \approx 18$) the buoyancy production rate is the highest, therefore providing a continuous source of turbulence production. As the shear stress production rate recovers, the buoyancy production rate decreases ($z = 22.5$). It results in a considerable magnitude of turbulent kinetic energy close to the wall, even if the Reynolds shear stress deteriorates, as can be seen in figure 3.21(c) and 3.21(f). This phenomenon is rarely observed in flows undergoing small changes in density (ideal gas), where the buoyancy production term is not as dominant. There, the turbulent kinetic energy also shows a decrease along with the Reynolds shear stress in the deterioration regime (see Ref. Bae *et al.* (2006)).

3.3.2.4 Case D

Case D represents an upward flow with strong buoyancy. Similar to case C, the flow undergoes both, deterioration and recovery. The DNS results for case D are shown in figure 3.22, again for Reynolds shear stress (a), radial turbulent heat flux (b), turbulent kinetic energy (c), shear (d), buoyant (e) and total production (f) rate of turbulent kinetic energy. The results show the same trend as those in case C, but with an earlier onset of recovery ($z \approx 9$) and a larger increase in turbulence. This leads to lower wall temperatures in the recovery region. In the deterioration region (until $z \approx 9$), the Reynolds shear stress sharply decreases and becomes negative at locations slightly away from the wall. Further downstream, the Reynolds shear stress is negative in most of the radial domain, except close to the wall. The Reynolds shear stress peaks to an absolute value of 1.2 at $z = 22.5$, which is 1.5 times the peak value at the inlet. The turbulent heat flux also increases after the recovery onset. Comparing the Reynolds shear stress and turbulent heat flux for cases A and D at $z = 7.5$, one can see that both values for case A are higher, but the wall temperature is higher. The reason is the high local flow acceleration due to buoyancy close to the wall, which causes an increase of advective heat transfer (section 1.4).

Figure 3.22(d) shows a negative value of the shear production rate between two positive peaks in the recovery regime. This is due to the fact that the velocity gradient and the Reynolds shear stress change sign at different locations. This can be observed in figure 3.23, which shows the velocity gradient $\partial\tilde{w}/\partial r$ and the turbulent shear stress $\overline{\rho u''w''}$. At the location of $\overline{\rho u''w''} = 0$ the velocity gradient $\partial\tilde{w}/\partial r$ is large and vice versa. Another interesting point to note is the buoyancy production term in figure 3.22(e), which for case D has the same order of magnitude and the same sign as the shear production rate. Similar to case C, when the shear production rate decreases to zero ($z = 7.5$), the buoyancy production rate is the highest, which keeps/increases the source of turbulence production (figure 3.22(f)).

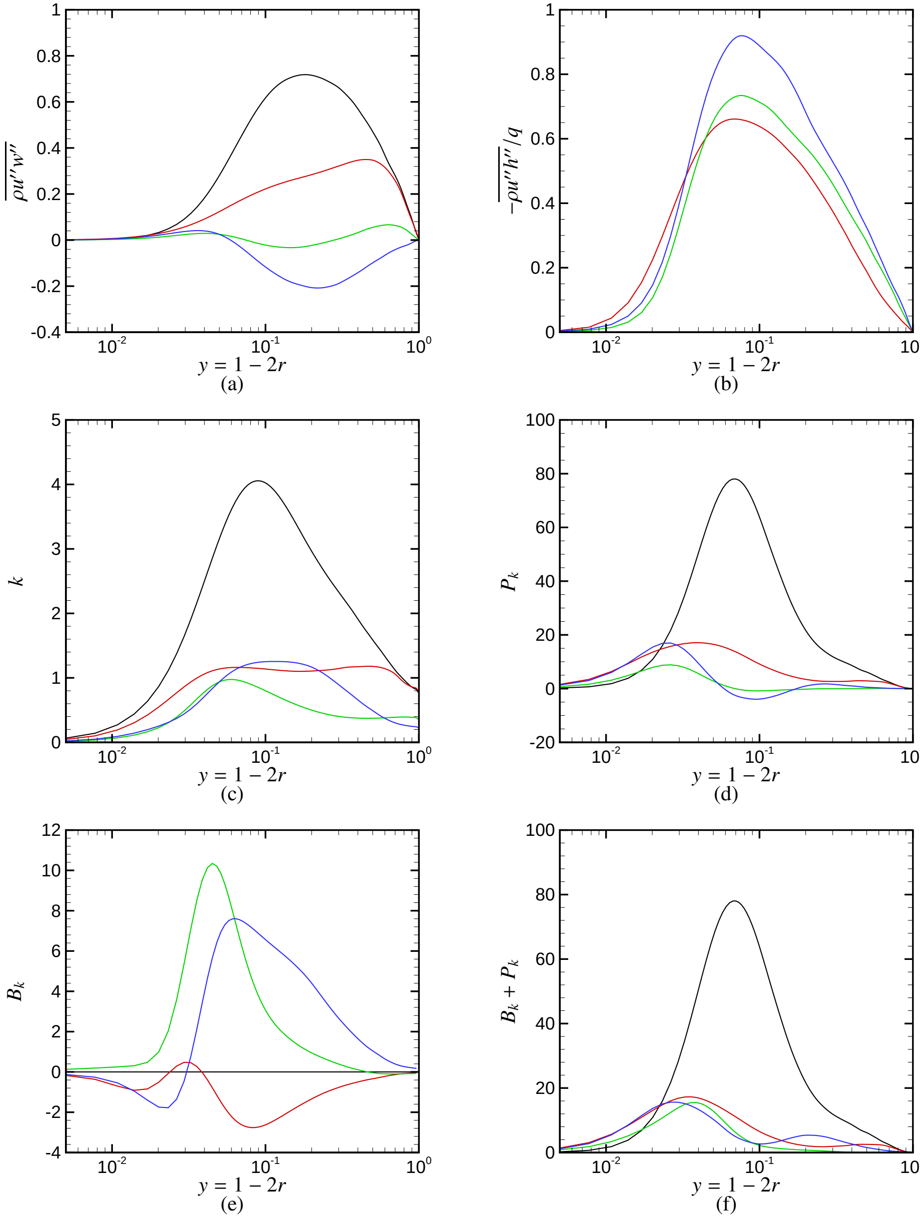

Figure 3.21: Evolution of Reynolds shear stress (a), turbulent heat flux (b), turbulent kinetic energy (c), shear (d), buoyant (e) and total production rate (f) along the pipe for case C. Black - $z = 0$; red - $z = 7.5$; green - $z = 15$; blue - $z = 22.5$.

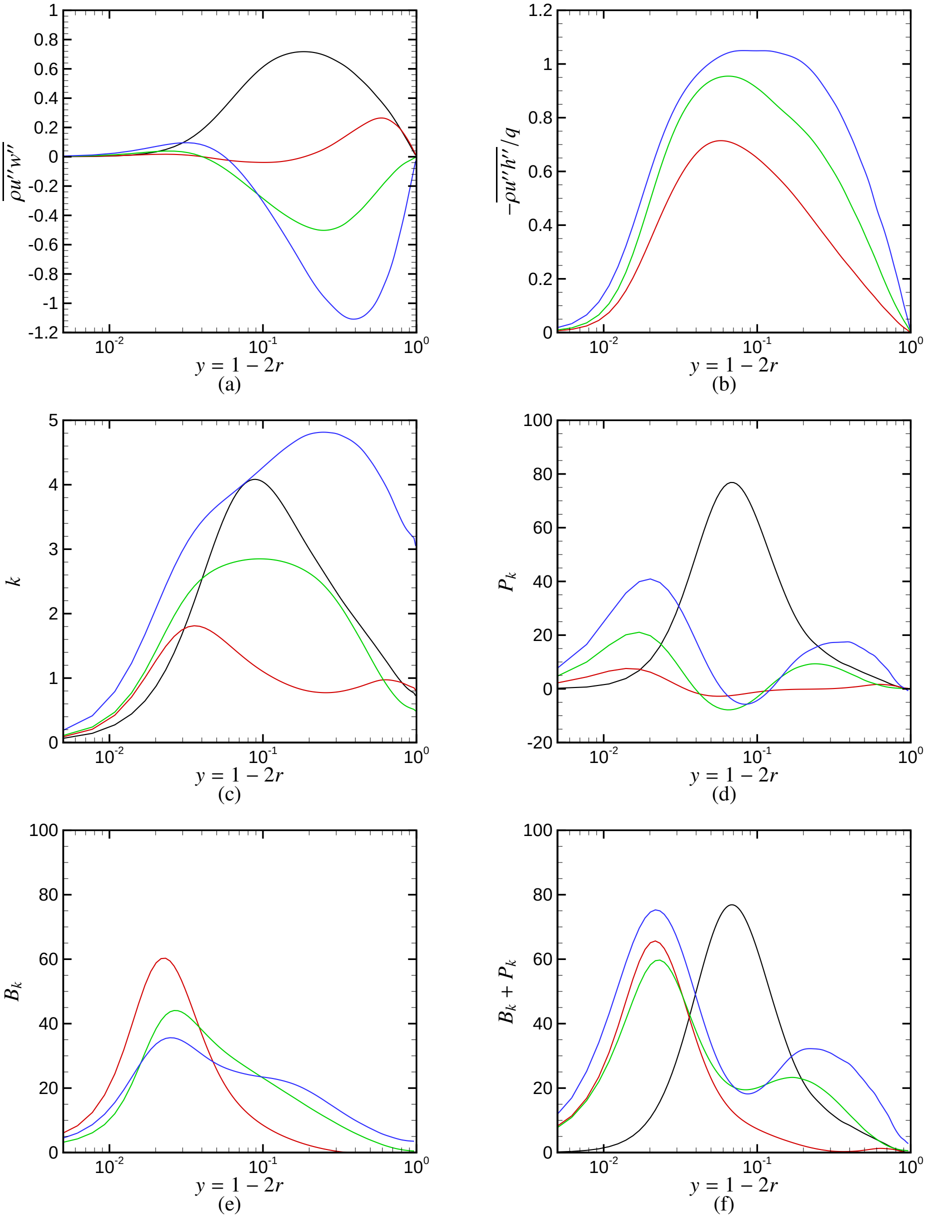

(a) (b) (c) (d) (e) (f)

Figure 3.22: Evolution of Reynolds shear stress (a), turbulent heat flux (b), turbulent kinetic energy (c), shear (d), buoyant (e) and total production rate (f) along the pipe for case D. Black - $z = 0$; red - $z = 7.5$; green - $z = 15$; blue - $z = 22.5$.

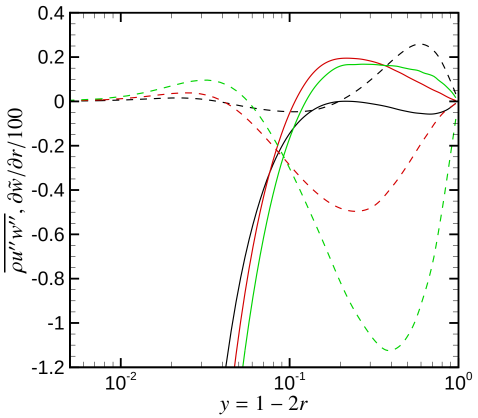

Figure 3.23: Comparison of Reynolds shear stress $\overline{\rho u''w''}$ and $\partial\tilde{w}/\partial r/100$ for case D. Solid lines - $\partial\tilde{w}/\partial r/100$; dashed lines - $\overline{\rho u''w''}$; black - $z = 7.5$; red - $z = 15$; green - $z = 22.5$.

3.3.2.5 Case E

Case E presents a downward flow with moderate buoyancy. In this case, the flow experiences a very short deterioration in the inlet region ($z = 1$) followed by a recovery. Similar to previous cases, the DNS results for case E are shown in figure 3.24. Compared to forced convection in upward flows, an absolute enhancement in turbulence is observed (figures 3.24(a), 3.24(b) and 3.24(c)). As mentioned in section 1.4, downward heated flows are always unstably stratified ($g\partial\rho/\partial z < 0$), in which the buoyant turbulent production acts as a source (positive) in the turbulent kinetic energy budget (figure 3.24(e)). Also, external effects of buoyancy, which change the mean velocity profile (see figure 3.17(e)), further promote shear production (figure 3.24(d)).

3.3.3 Significance of correlations with property fluctuations

3.3.3.1 Momentum

The dominant shear stress in the pipe flow is $\overline{\tau}_{rz}$, which can be decomposed as

$$\overline{\tau}_{rz} = (2\overline{\mu}\tilde{S}_{rz} + 2\overline{\mu' S''_{rz}} + 2\overline{\mu}\overline{S''_{rz}}). \tag{3.10}$$

The second-order moment $2\overline{\mu' S''_{rz}}$ and the first order moment $2\overline{\mu}\overline{S''_{rz}}$ appear only due to property fluctuations and will be zero for constant property flows. A comparison of $2\overline{\mu}\tilde{S}_{rz}$, $2\overline{\mu' S''_{rz}}$, $2\overline{\mu}\overline{S''_{rz}}$ and $\overline{\tau}_{rz}$ is shown for cases A and E in figure 3.25. $2\overline{\mu}\overline{S''_{rz}}$ is appreciable only very close to the wall, while $2\overline{\mu' S''_{rz}}$, caused by viscosity fluctuations, is negligible. From

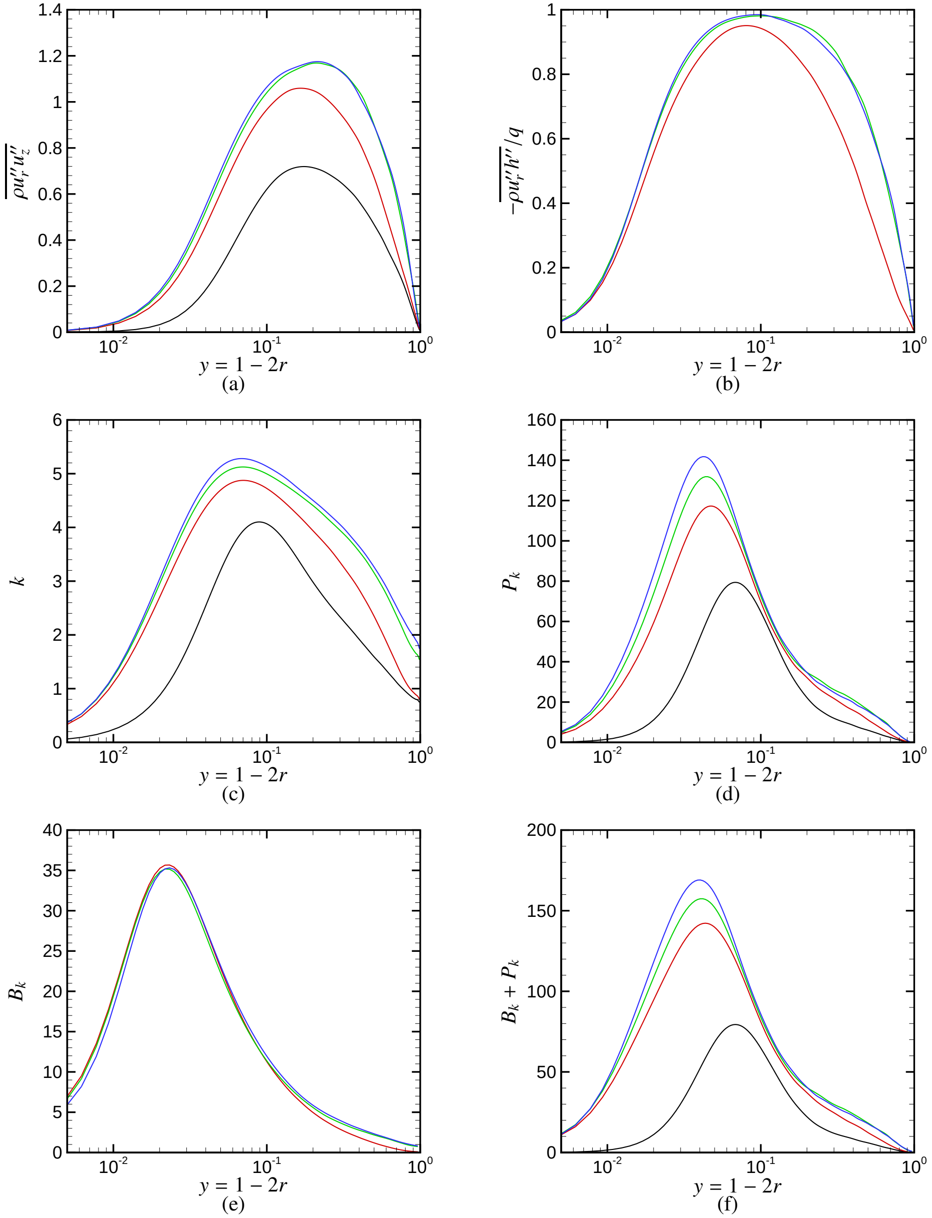

Figure 3.24: Evolution of Reynolds shear stress (a), turbulent heat flux (b), turbulent kinetic energy (c), shear (d), buoyant (e) and total production rate (f) along the pipe for case E. Black - $z = 0$; red - $z = 7.5$; green - $z = 15$; blue - $z = 22.5$.

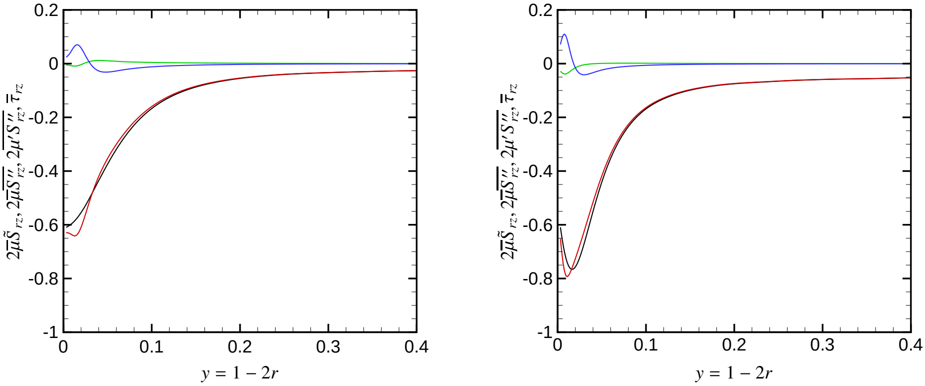

(a) Case A

(b) Case E

Figure 3.25: Contribution of correlations on total viscous shear stress for (a) case A and (b) case E at $z = 15$. Black - $\overline{\tau}_{rz}$; red - $2\overline{\mu}\tilde{S}_{rz}$; green - $2\overline{\mu}\overline{S''_{rz}}$; blue - $2\overline{\mu' S''_{rz}}$.

a physical point of view, this can be attributed to the fact that the gradient of the mean flow $\tilde{w}$ close to the wall is very high compared to that of the fluctuating component $\overline{w''}$.

3.3.3.2 Energy

Among the additional terms generated, namely $\partial/\partial x_i(\overline{\alpha}\partial\overline{h''}/\partial x_i)$ and $\partial/\partial x_i(\overline{\alpha'\partial h''/\partial x_i})$, only the radial gradients play a significant role. The total radial heat flux can then be written as

$$q_{r,tot} = \overline{\alpha}\frac{\partial\tilde{h}}{\partial r} + \overline{\alpha}\frac{\partial\overline{h''}}{\partial r} + \overline{\alpha'\frac{\partial h''}{\partial r}}. \tag{3.11}$$

Again, the first order moment $\overline{\alpha}\partial\overline{h''}/\partial r$ and the second-order moment $\overline{\alpha'\partial h''}/\partial r$ are zero for constant property flows. Figure 3.26 shows the comparison of the radial heat flux terms at $z = 15$ for cases A and E. It is important to note that the total heat flux at the wall $q_{r,tot}$ is equal to 2.4, which is the non-dimensional constant wall heat flux Q used in the simulation. The mean heat flux $\overline{\alpha}\partial\tilde{h}/\partial r$ is modified not only close to the wall, but also at the wall, where its value is 2.7 and 3.15, which are 12.5% and 31% higher than Q for cases A and E, respectively. This can be thought of as a quenching effect due to $\overline{\alpha}\partial\overline{h''}/\partial r$ and $\overline{\alpha'\partial h''}/\partial r$, which are negative at the wall. This will result in a higher mean enthalpy at the wall, hence also modifying the heat transfer coefficient. It is interesting to note that the $\overline{\alpha}\partial\overline{h''}/\partial r$ and $\overline{\alpha'\partial h''}/\partial r$ are zero at the wall if the isothermal wall boundary condition is applied. The peak value of the mean heat flux is approximately 45% higher than the total heat flux for case A around $y^+ \approx 3$. Figure 3.27 shows the derivatives of $\overline{\alpha}\partial\tilde{h}/\partial r$, $\overline{\alpha}\partial\overline{h''}/\partial r$, $\overline{\alpha'\partial h''}/\partial r$ and $\overline{\rho u''_r h''}$, as they appear in the energy equation. It can be seen that

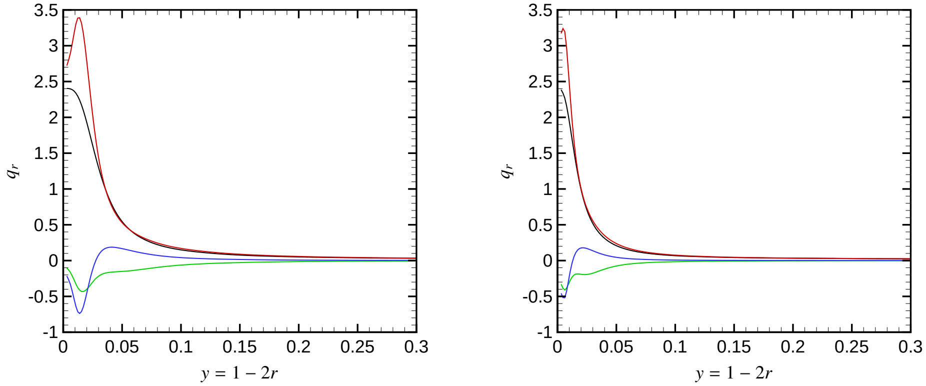

(a) Case A

(b) Case E

Figure 3.26: Contribution of correlations on total heat flux for (a) case A and (b) case E at $z = 15$. Black - $q_{r,tot}$; red - $\overline{\alpha}\partial\tilde{h}/\partial r$; green - $\overline{\alpha}\partial\overline{h''}/\partial r$; blue - $\overline{\alpha'\partial h''}/\partial r$.

the magnitude of the additional terms is significant close to the wall for both cases, hence causing an additional enthalpy transfer.

3.3.4 Quadrant analysis

The quadrant analysis provides information to identify fractional contributions of instantaneous fluctuations to turbulence statistics, such as the turbulent shear stress $\overline{\rho u''w''}$ and the turbulent heat flux $-\overline{\rho u''h''}$, investigated here. Independently, Wallace *et al.* (1972) and Willmarth & Lu (1972) developed this method in order to distinguish the individual contributions of ejection and sweep events to drag or heat transfer. Since then, this analysis has been used in many different flows; e.g., boundary layer flows (Lee *et al.*, 2013; Nolan *et al.*, 2010), turbulent channel flows (Moin & Kim, 1985; Antonia *et al.*, 1992) and to study the mechanism of particle motions in turbulent flows (Zeinali *et al.*, 2012). Ejection events (also called burst activities) originate in the vicinity of the wall and transport fluid away from the wall, while sweep events originate in the core flow and move fluid towards the wall.

For this technique, $\overline{\rho u''w''}$ is conditionally averaged based on instantaneous values of $\sqrt{\rho}u''$ and $\sqrt{\rho}w''$. Depending on the sign of $\sqrt{\rho}u''$ and $\sqrt{\rho}w''$, four individual contributions to the turbulent shear stress are distinguished, which are then averaged and plotted in four quadrants. The result of this conditional averaging is shown in figures 3.28-3.31 as a function of wall-normal distance for cases B to E (case A will be discussed in the next chapter). The quadrants $Q1$ and $Q3$ are the so-called sweep and ejection events, which have the largest contributions to the Reynolds shear stress. In the low buoyancy upward flow (case B) all contributions to the Reynolds shear stress are attenuated as proceeding downstream (similar behaviour is observed for case A).

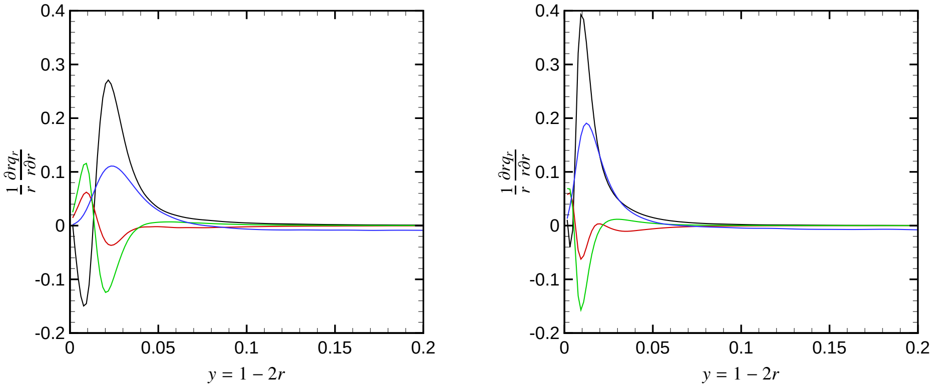

(a) Case A

(b) Case E

Figure 3.27: Derivative of heat flux terms for case A at $z = 15$. Black - $\partial(r\overline{\alpha}\partial\tilde{h}/\partial r)/(r\partial r)$; red - $\partial(r\overline{\alpha'\partial h''/\partial r})/(r\partial r)$; green - $\partial(r\overline{\alpha}\partial\overline{h''}/\partial r)/(r\partial r)$; blue - $-\partial(r\overline{\rho u_r'' h''})/r\partial r$.

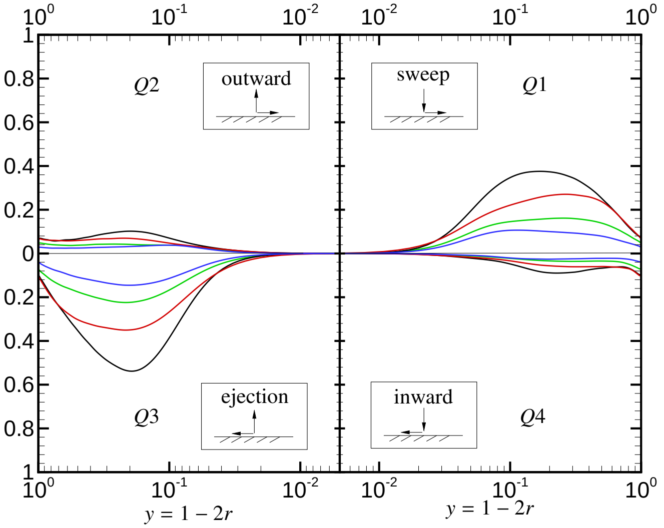

Figure 3.28: Fractional contribution to the Reynolds shear stress $\overline{\rho u'' w''}$ for case B. Black - $z = 0$; red - $z = 7.5$; green - $z = 15$; blue - $z = 22.5$.

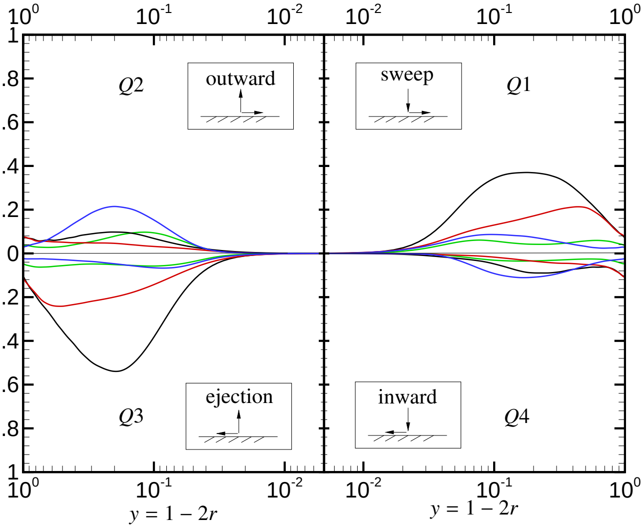

Figure 3.29: Fractional contribution to the Reynolds shear stress $\overline{\rho u''w''}$ for case C. Black - z = 0; red - z = 7.5; green - z = 15; blue - z = 22.5.

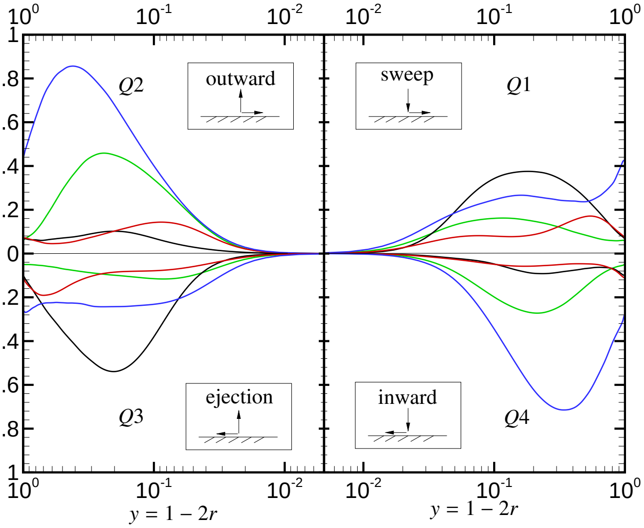

Figure 3.30: Fractional contribution to the Reynolds shear stress $\overline{\rho u''w''}$ for case D. Black - z = 0; red - z = 7.5; green - z = 15; blue - z = 22.5.

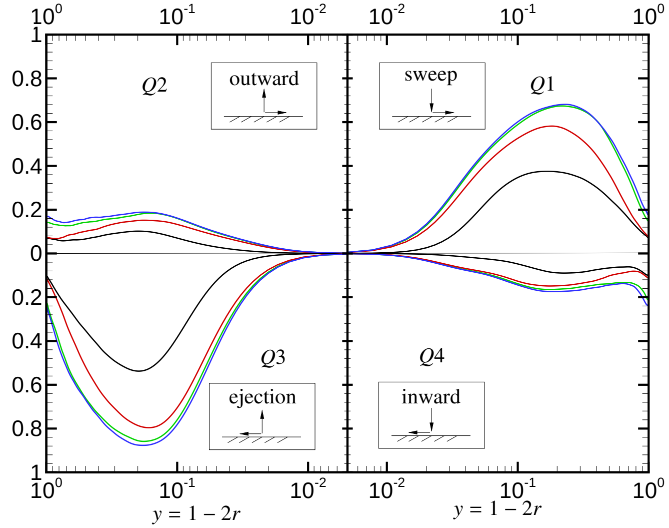

Figure 3.31: Fractional contribution to the Reynolds shear stress $\overline{\rho u''w''}$ for case E. Black - $z = 0$; red - $z = 7.5$; green - $z = 15$; blue - $z = 22.5$.

Compared to case B, there is a slight enhancement in all events at $z = 22.5$ for case C, which is the location where turbulence recovery starts. As can be seen, outward and inward motions show a larger increase among all events. This trend is more apparent in the case of high buoyancy, where the upward and inward motions are the dominant contributions to the Reynolds shear stress. This change in relative contributions stems from structural and external effects of buoyancy. To highlight how structural effects affect buoyant production of Reynolds shear stress, figure 3.32 shows $B_{\overline{\rho u''w''}} = \mp Ri_{0z}\overline{\rho' u'}$ for cases C and D. For both cases the buoyancy production of Reynolds shear stress is negative (i.e. ρ' and u' are positively correlated), which favours the negative contribution of shear rate production $P_{\overline{\rho u''w''}} = -\overline{\rho u''u''}\partial\tilde{w}/\partial r$. In the case with downward flow (case E) all the contributions are enhanced as expected. It can be seen that ejection and sweep events have the largest increase compared to inward and outward events.

Similarly, also the radial turbulent heat flux $\overline{\rho u''h''}$ can be conditionally averaged based on the sign of $\sqrt{\rho}u''$ and $\sqrt{\rho}h''$. Here, the quadrants $Q1$ and $Q2$ are associated with cold fluid moving towards and away from the wall, respectively. $Q3$ and $Q4$ represent hot fluid moving away and towards the wall, respectively. Figures 3.33-3.36 show the contributions from each quadrant to the radial turbulent heat flux $\overline{\rho u''h''}$ plotted as a function of wall-normal coordinate. In the case of low buoyancy upward flow (case B) and moderate buoyancy downward flow (case E), there are no considerable changes along the pipe (see also figures 3.20(b) and 3.24(b)). On the other hand, all events increase in downstream direction for cases C and D, where the $Q1$ and $Q3$ events are enhanced. Compared to the Reynolds shear stress, no relative importance in events for

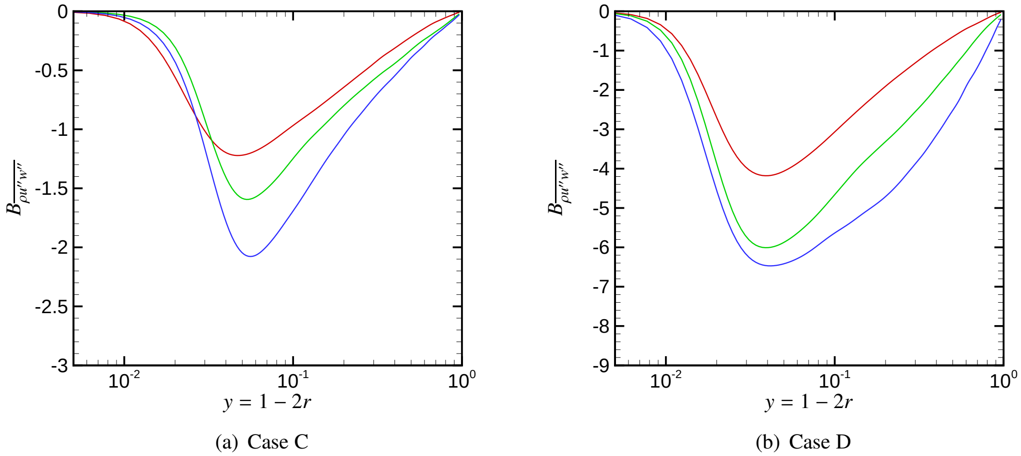

(a) Case C

(b) Case D

Figure 3.32: Buoyancy production of the Reynolds shear stress $\overline{\rho u''w''}$. Red - $z = 7.5$; green - $z = 15$; blue - $z = 22.5$.

turbulent heat flux is observed for cases C and D. u'' and h'' are positively and h'' and ρ' are negatively correlated (see figures 3.32(a) and 3.32(b)). Therefore, one can expect that the increase in turbulent heat flux results due to an enhancement in $Q1$ and $Q3$ events.

3.3.5 FIK identity

A general understanding of turbulent flows is that the major part of skin friction is attributed to the near-wall vortical motions, i.e., ejection/sweep events (Robinson, 1991). Based on this knowledge a variety of ideas have been examined to establish a theoretical framework for skin friction drag reduction. Fukagata *et al.* (2002) have derived a general mathematical relationship, called Fukagata-Iwamoto-Kasagi (FIK) identity, between the skin friction coefficient and different dynamical contributions for wall-bounded flows, e.g. channel and pipe flows and flat plane boundary layer flow. Since then it has been used extensively to study drag reduction mechanisms and active control strategies in fully developed channel and pipe flows (Fukagata & Kasagi, 2003), developing turbulent boundary layers with suction and blowing (Kametani & Fukagata, 2011), heated developing turbulent boundary layers (Lee *et al.*, 2013) and compressible flows (Gomez *et al.*, 2009). Fukagata *et al.* (2005) also used the same approach to derive an identity relation for the Nusselt number and turbulent heat flux in fully developed incompressible channel flows.

In this work, we obtain the FIK identity to take into account the strong property fluctuations in supercritical fluids, by integrating the streamwise momentum and enthalpy equations twice in the radial direction. The FIK identity for the skin friction

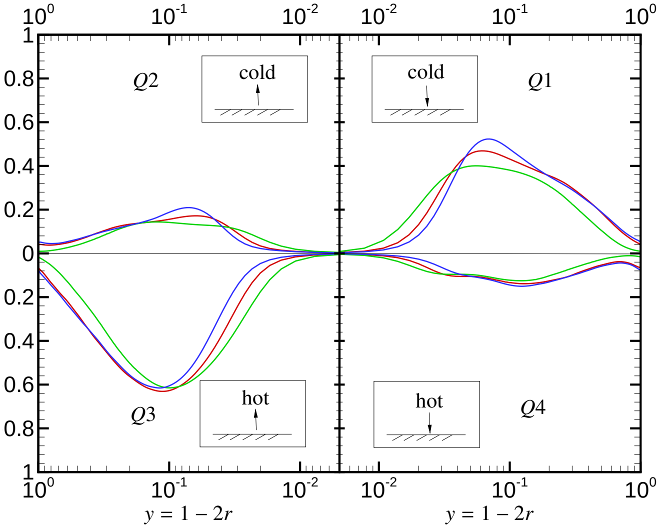

Figure 3.33: Fractional contribution to the turbulent heat flux $\overline{\rho u'' h''}/q$ for case B. Red - $z = 7.5$; green - $z = 15$; blue - $z = 22.5$.

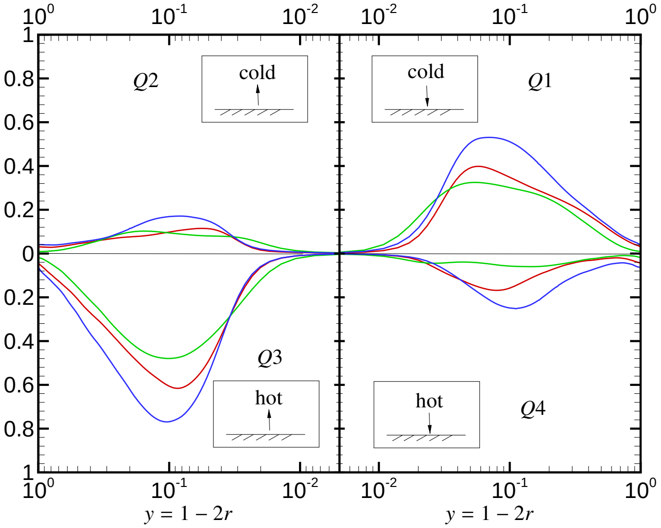

Figure 3.34: Fractional contribution to the turbulent heat flux $\overline{\rho u'' h''}/q$ for case C. Red - $z = 7.5$; green - $z = 15$; blue - $z = 22.5$.

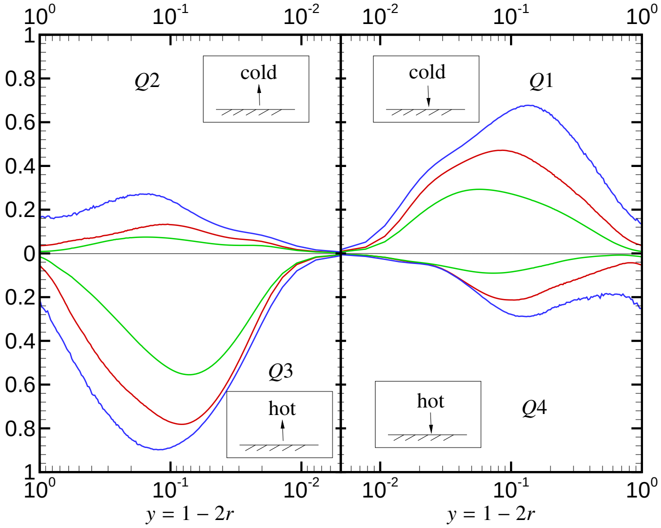

Figure 3.35: Fractional contribution to the turbulent heat flux $\overline{\rho u'' h''}/q$ for case D. Red - $z = 7.5$; green - $z = 15$; blue - $z = 22.5$.

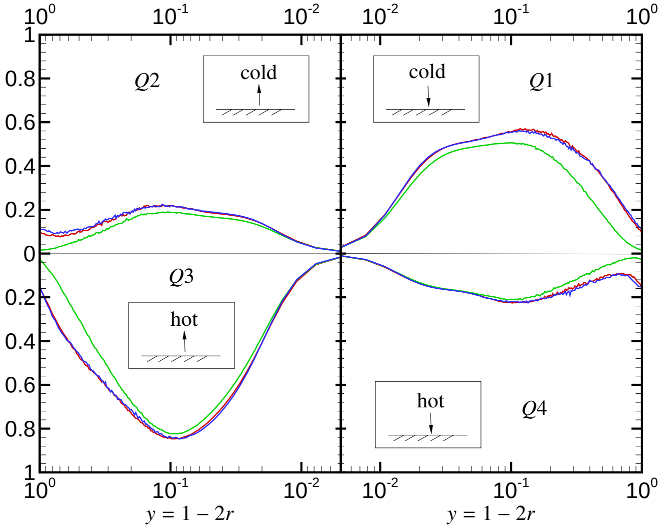

Figure 3.36: Fractional contribution to the turbulent heat flux $\overline{\rho u'' h''}/q$ for case E. Red - $z = 7.5$; green - $z = 15$; blue - $z = 22.5$.

reads (the complete derivation can be found in appendix A):

$$
\begin{aligned}
C_{f,FIK} = & \underbrace{-\frac{2}{\rho_b U_b^2 Re_{\tau 0}} \int_0^R r\overline{\mu}\overline{S}_{rz} rdr}_{C_I} + \underbrace{\frac{2}{\rho_b U_b^2} \int_0^R r\overline{\rho u_r'' u_z''} rdr}_{C_{II}} \\
& \underbrace{+ \frac{1}{\rho_b U_b^2} \int_0^R (R^2 - r^2) \left\langle \frac{\partial \overline{p}}{\partial z} \right\rangle rdr}_{C_{III}} + \underbrace{\frac{1}{\rho_b U_b^2} \int_0^R r\overline{\rho}\tilde{u}_r\tilde{u}_z rdr}_{C_{IV}} \\
& \underbrace{+ \frac{1}{\rho_b U_b^2} \int_0^R (R^2 - r^2) \left\langle \frac{\partial \overline{\rho}\tilde{u}_z\tilde{u}_z}{\partial z} \right\rangle rdr}_{C_V} + \underbrace{\frac{1}{\rho_b U_b^2} \int_0^R (R^2 - r^2) \left\langle \frac{\partial \overline{\rho u_z'' u_z''}}{\partial z} \right\rangle rdr}_{C_{VI}} \\
& \underbrace{- \frac{1}{\rho_b U_b^2 Re_{\tau 0}} \int_0^R (R^2 - r^2) \left\langle \frac{1}{r} \frac{\partial r\overline{\mu' S'_{rz}}}{\partial r} \right\rangle rdr}_{C_{VII}} \underbrace{- \frac{1}{\rho_b U_b^2 Re_{\tau 0}} \int_0^R (R^2 - r^2) \left\langle \frac{\partial \overline{\mu}\overline{S}_{zz}}{\partial z} \right\rangle rdr}_{C_{VIII}} \\
& \underbrace{- \frac{1}{\rho_b U_b^2 Re_{\tau 0}} \int_0^R (R^2 - r^2) \left\langle \frac{\partial \overline{\mu' S'_{zz}}}{\partial z} \right\rangle rdr}_{C_{IX}} \pm \underbrace{\frac{Ri_{0z}}{\rho_b U_b^2} \int_0^R (R^2 - r^2) \left\langle \overline{\rho} \right\rangle rdr}_{C_X},
\end{aligned}
\tag{3.12}
$$

where $\langle\ \rangle$ indicates the following operation

$$
\langle \Phi(r,z) \rangle = \Phi(r,z) - \frac{2}{R^2} \int_0^R \Phi(r,z) rdr. \tag{3.13}
$$

Equation (3.12) shows that the skin friction coefficient can be decomposed into a laminar contribution C_I, which for a constant property fluid is identical to the analytical solution for laminar flows $16/Re_{b0}$, a turbulent contribution C_{II} and several inhomogeneous contributions C_{III} to C_X. The merit of this equation is that different contributions to skin friction can be compared for fluids with constant or variable properties.

Figure 3.37 presents the distribution of the local skin friction coefficient for all cases. The skin friction coefficient is defined as $C_f = 2\left(\mu \partial w / \partial r|_{wall}\right) / \left(\rho_b U_b^2\right)$. The skin friction coefficient at the inlet (or the inflow generator) is $C_f = 9.26 \times 10^{-3}$, which is in perfect agreement with the Blasius correlation ($0.079/Re_b^{1/4} = 9.27 \times 10^{-3}$). The common observation among all cases is that C_f experiences a rapid reduction after the inlet due to the sharp decrease in dynamic viscosity at the wall μ_w. After this initial decrease, μ_w

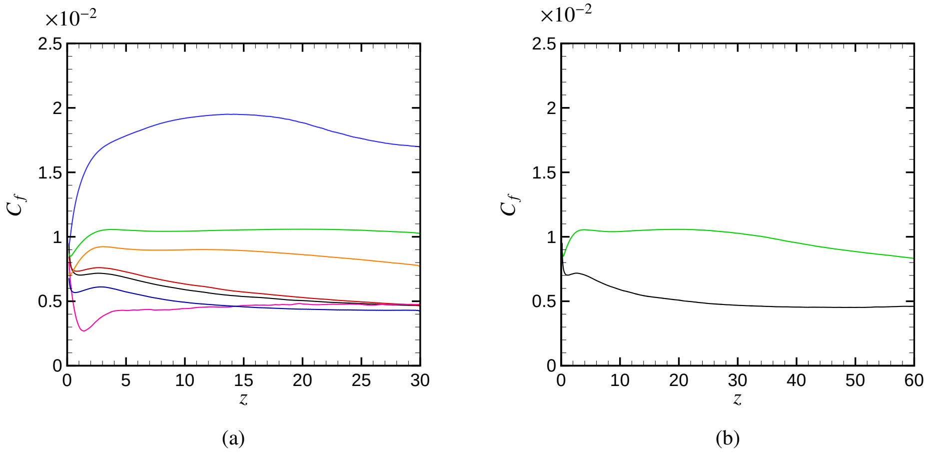

(a)

(b)

Figure 3.37: Skin friction C_f distribution for cases A to G (a), and for cases A$_{60}$ and C$_{60}$ (b). Black - case A and A$_{60}$; red - case B; green - case C and C$_{60}$; blue - case D; pink - case E; dark blue - case F; orange - case G.

becomes almost constant and mostly the variation in $\partial w/\partial r|_{wall}$ is responsible for changes in C_f (see figure 3.38). Compared to the forced convection (case A) and downward flow case, the upward flows show an increase of C_f due to buoyancy. This is due to an increase in the mean streamwise velocity gradient, resulting from a favourable buoyancy-induced flow acceleration.

The results of Eq. (3.12) are plotted for different cases in figure 3.39 (note, insignificant terms are not shown). To verify the FIK derivation, the sum of all terms is compared with C_f computed by means of the velocity gradient at the wall. An excellent agreement is obtained, ensuring correctness and consistency of Eq. (3.12) (symbols and line overlap). As expected, the laminar and turbulent contributions at the inlet are $3.04 \times 10^{-3} = 16/Re_{b0}$ and 6.23×10^{-3}, respectively. Note, that the same agreement is observed for those cases that are not shown. These contributions are identical to the results of a fully developed pipe flow that have also been reported by Fukagata *et al.* (2002). Interestingly, farther downstream, the laminar contribution C_I is identical in all cases shown in this figure (pink lines in figures 3.39(a) to 3.39(c)). The reason for this is that the bulk Reynolds number $Re_b = \rho_b U_b D/\mu_b$ is the same for the cases with the same heat flux. The term related to the turbulent contribution C_{II} considerably changes further downstream. With an increase in buoyancy for upward flows, C_{II} reduces from the inlet and its contribution to the skin friction becomes negative in cases C and D. This can be explained by referring to figures 3.21(a) and 3.21(a), where the profile of Reynolds shear stress becomes negative in the core region. In the case of downward flow (case E), this term increases to values higher than $C_{f,FIK}$ along the downstream direction (see figure 3.24(a)).

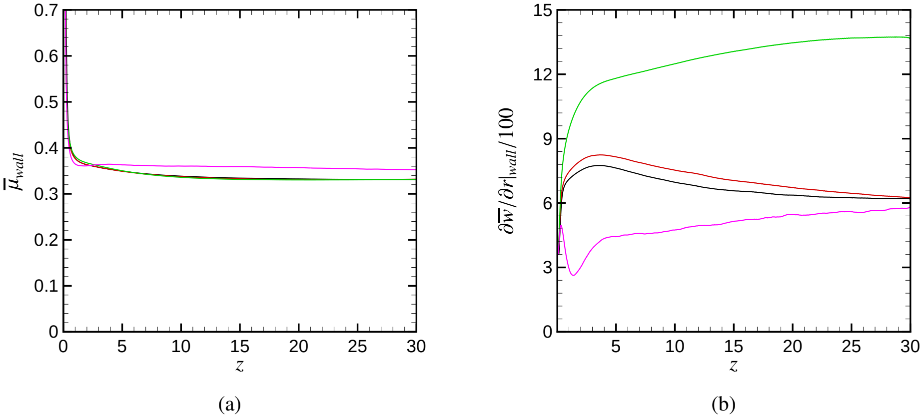

Figure 3.38: (a) Wall dynamic viscosity and (b) wall streamwise velocity gradient. Black - case A; red - case B; green - case C; pink - case E.

The inhomogeneous contributions play a significant role for the skin friction in heated flows at supercritical pressures (unlike for the constant properties which will be discussed in the next chapter). The behaviour of the term related to the streamwise momentum flux (C_V) follows the evolution of the mean streamwise velocity profile along the pipe. Depending on the rate of change in the radial profile of the streamwise momentum $\partial\overline{\rho}\tilde{u}_z\tilde{u}_z/\partial z(r,z)$, this contribution can be negative or positive. For instance, at the inlet region for upward flows, this value is positive in the near-wall region and negative in the core region of the flow. Since the bulk flow has a larger contribution to the integral (see figure 3.40), it results in negative values. The opposite holds for the downward flow case (case E). In contrast to C_V, the term C_{IV} (the product of the mean density, mean wall-normal and streamwise velocities) experiences an increase at the inlet region in upward flows. This can be explained by the sharp changes of streamwise velocity in the near-wall region, which results in a high positive/negative wall-normal velocity at the inlet region. The last term C_X, which is the contribution due to gravity, depends on the value of Ri_0 and the direction of the flow. As expected, this term positively contributes to the total skin friction in upward flows; the opposite is true for downward flow.

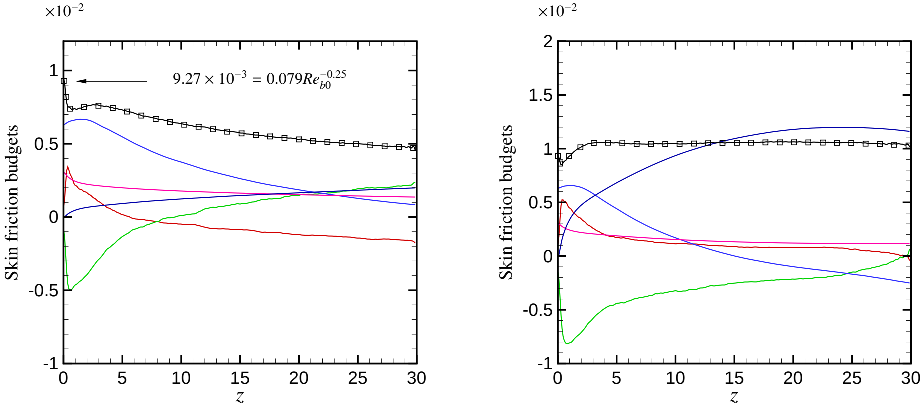

(a) Case B

(b) Case C

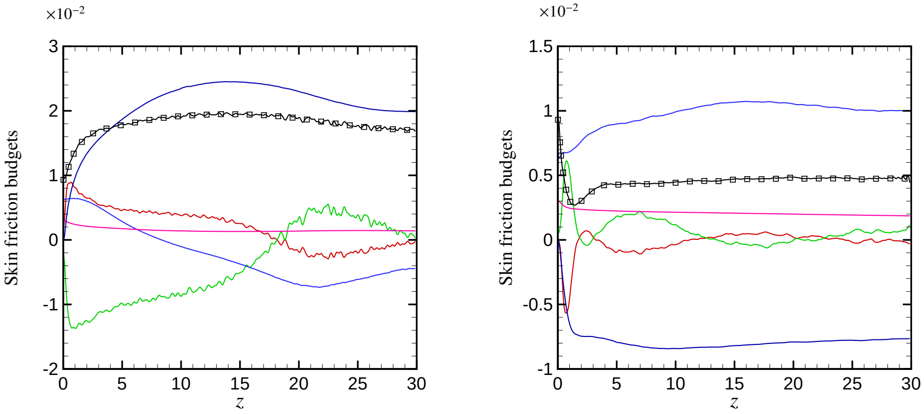

(c) Case D

(d) Case E

Figure 3.39: Componential contributions to the skin friction. The lines indicate the individual terms as given in Eq. (3.12) and the symbols indicate the locally computed skin friction C_f. Black - $C_{f,FIK}$; pink - C_I; blue - C_{II}; red - C_{IV}; green - C_V; dark blue - C_X.

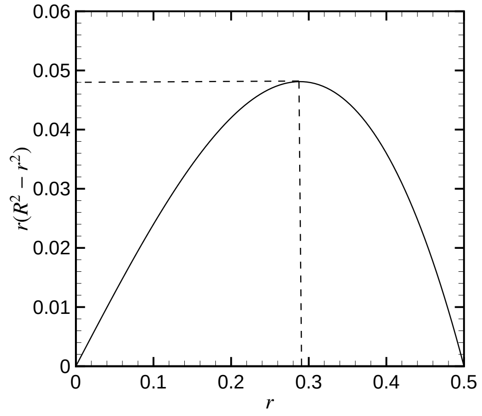

Figure 3.40: Distribution of weighting factor $r(R^2 - r^2)$.

Similar to the skin friction, the FIK identity for the Nusselt number reads:

$$
\begin{aligned}
Nu_{FIK} = {} & \underbrace{\frac{32}{\alpha_b(\overline{h}_{wall} - h_b)}\int_0^R r\overline{\alpha}\frac{\partial\overline{h}}{\partial r}rdr}_{H_I} - \underbrace{\frac{32Re_{\tau0}Pr_0}{\alpha_b(\overline{h}_{wall} - h_b)}\int_0^R r\overline{\rho u_r''h''}rdr}_{H_{II}} \\
& \underbrace{-\frac{16Re_{\tau0}Pr_0}{\alpha_b(\overline{h}_{wall} - h_b)}\int_0^R (R^2 - r^2)\left\langle\frac{1}{r}\frac{\partial r\overline{\rho}\tilde{u}_r\tilde{h}}{\partial r}\right\rangle rdr}_{H_{III}} \underbrace{-\frac{16Re_{\tau0}Pr_0}{\alpha_b(\overline{h}_{wall} - h_b)}\int_0^R (R^2 - r^2)\left\langle\frac{\partial\overline{\rho}\tilde{u}_z\tilde{h}}{\partial z}\right\rangle rdr}_{H_{IV}} \\
& \underbrace{-\frac{16Re_{\tau0}Pr_0}{\alpha_b(\overline{h}_{wall} - h_b)}\int_0^R (R^2 - r^2)\left\langle\frac{\partial\overline{\rho u_z''h''}}{\partial z}\right\rangle rdr}_{H_V} + \underbrace{\frac{16}{\alpha_b(\overline{h}_{wall} - h_b)}\int_0^R (R^2 - r^2)\left\langle\frac{1}{r}\frac{\partial r}{\partial r}\overline{\alpha'\frac{\partial h'}{\partial r}}\right\rangle rdr}_{H_{VI}} \\
& \underbrace{+\frac{16}{\alpha_b(\overline{h}_{wall} - h_b)}\int_0^R (R^2 - r^2)\left\langle\frac{\partial}{\partial z}(\overline{\alpha}\frac{\partial\overline{h}}{\partial z})\right\rangle rdr}_{H_{VII}} + \underbrace{\frac{16}{\alpha_b(\overline{h}_{wall} - h_b)}\int_0^R (R^2 - r^2)\left\langle\frac{\partial}{\partial z}(\overline{\alpha'\frac{\partial h'}{\partial z}})\right\rangle rdr}_{H_{VIII}},
\end{aligned}
\tag{3.14}
$$

where H_I is laminar, H_{II} is turbulent and the remaining terms are inhomogeneous contributions to the Nusselt number. The subscript $_{wall}$ denotes wall quantities.

As mentioned before, the enhancement and deterioration of heat transfer can be easily recognised from the behaviour of wall temperature. One way of representing the

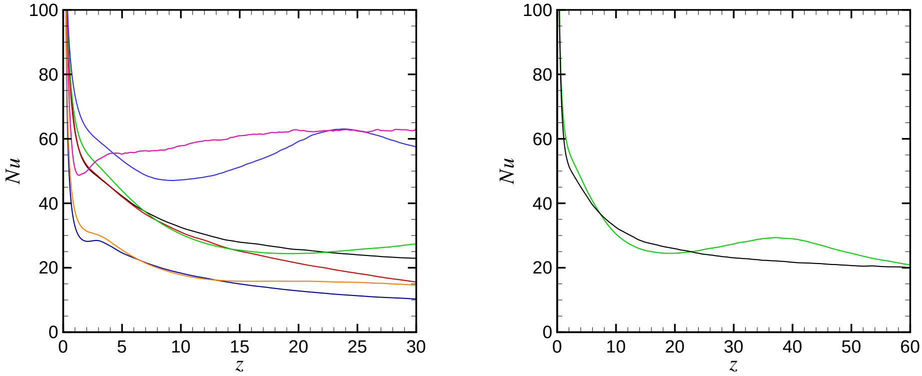

(a)

(b)

Figure 3.41: Distribution of local Nusselt number Nu (a) cases A to G (b) A_{60} and C_{60}. Black - case A and A_{60}; red - case B; green - case C and C_{60}; blue - case D; pink - case E; dark blue - case F; orange - case G.

enhancement and deterioration of heat transfer is the Nusselt number, which is defined as $Nu = Q / \left(\alpha_b \left(\overline{h}_{wall} - h_b \right) \right)$. It shows that the Nusselt number highly depends on wall enthalpy, while D and Q are constant and α_b and h_b are locally identical for cases with the same Q. The distribution of Nusselt number for all cases is plotted in figure 3.41. The figure confirms the enhancement and deterioration of heat transfer, as discussed in figures 3.14 and 3.15.

Next, the effect of componential contribution to Nusselt number is investigated in figure 3.42 for cases B to E (again the negligible terms are not shown). As for the skin friction discussed above, the FIK derivation for the Nusselt number is first verified. The sum of all terms is compared with the locally calculated Nusselt number. A perfect agreement is obtained, ensuring correctness and consistency of the derivation (symbols and line overlap). The most significant contributions to the Nusselt number, in terms of relative magnitude, are the radial turbulent heat flux H_{II}, the laminar part H_I and the contribution of the mean streamwise enthalpy flux H_{III}. By comparing the evolution of the laminar contribution for all cases, one can notice that they are qualitatively and quantitatively similar. Therefore, the differences in Nusselt number stem from the differences of H_{II} and H_{III}. It is evident that downstream from the inlet the radial turbulent heat flux H_{II} has the largest contribution to the Nusselt number for all cases. For case B, H_{II} is continuously decreasing after $z = 4.5$, which can be explained by the unchanged radial turbulent heat flux profile (figure3.20(b)), while $\overline{h}_{wall} - h_b$ is enhanced. The term H_{III} has a positive contribution to Nusselt number at inlet region and decreases further downstream. This is attributed to the streamwise gradient of the enthalpy profile growth (thermal boundary layer) and its product with streamwise velocity. For case C,

H_{II} shows a recovery at $z \approx 17$ and reaches the value close to the total Nusselt number Nu_{FIK} near the outlet and H_{III} becomes negative after $z = 25$. The negative values of H_{III} are related to the deformation of streamwise velocity to the M-shaped profile. In the case of high buoyancy in the upward flow case, the radial turbulent heat flux contribution H_{II} shows a peculiar behaviour and exhibits a peak greater than the total Nusselt number at $z \approx 23$. The changes in H_{II} is mainly attributed to the behaviour of the radial turbulent heat flux (figure 3.22(b)), since $\overline{h}_{wall} - h_b$ shows smaller changes compared to cases B and C. The overshoot of H_{II} is compensated by the negative contribution of H_{III}, which is in response of the M-shaped velocity profile. For the downward flow (case E), the contribution of the radial turbulent heat flux H_{II} becomes larger than Nu at $z = 10$ and reaches a plateau. Similarly, the larger values of H_{II} are balanced by the negative contribution of H_{III}.

3.3.6 Instantaneous fields

For heated flows at the supercritical pressure the turbulent kinetic energy, depending on flow conditions, showed a peculiar behaviour. It was shown that the turbulent structures are weakened for forced convection and low buoyancy upward flow in response to heating. In order to visualize the effects of heating and buoyancy on turbulent motions, the iso-surfaces of streamwise vorticity $\omega_z' = ((\partial r v')/(r \partial r) - (\partial u')/(r \partial \theta))$ are plotted in figures 3.43 and 3.44 for cases A to E. It can be seen that the evolution of vortical motions follows the behaviour of turbulent kinetic energy that was discussed before. As expected, in the case of forced convection (case A) the streamwise vorticity fluctuations become sparse along the pipe, which is due to thermal expansion. In addition to the thermal expansion, stabilising effects of buoyancy in case B result in a rather significant reduction in the population of structures in downstream direction.

For case C in the upstream region, the intensity of vortical motions significantly weakened, while farther downstream the turbulence is re-established due to the deformation of streamwise velocity to M-shaped profile. Similar behaviour is observed for case D, except that the transition from deterioration to recovery region is shorter and the vorticities in the recovery region are stronger. In the case of downward flow (case E), the vortical motions are continuously increasing from the inlet through the entire pipe length.

3.3.7 Jensen inequality

It has been observed that the averaged thermophysical properties (first order moment), in particular, $\overline{c_p}$ (and therefore $\overline{\alpha}$) deviates significantly from those evaluated using mean temperature or enthalpy, such that for a thermophysical property ϕ in a turbulent flow

$$\overline{\phi} \neq \phi(\tilde{h}, P_0). \tag{3.15}$$

This can be explained with the help of the Jensen inequality, which states that the convex transformation of a mean is less than or equal to the mean after a convex transformation

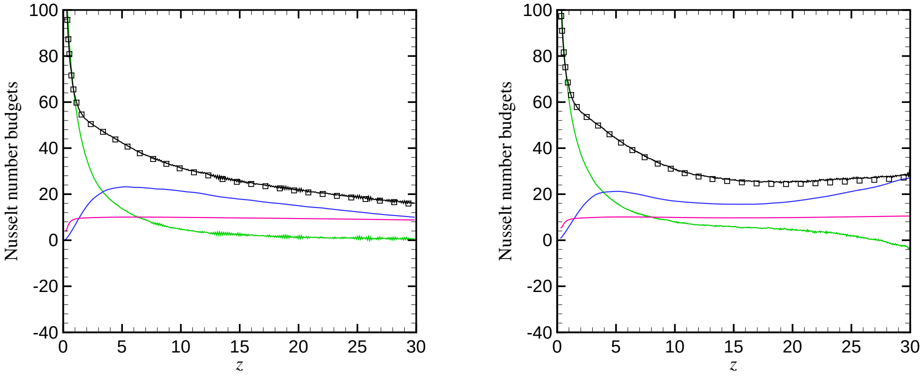

(a) Case B (b) Case C

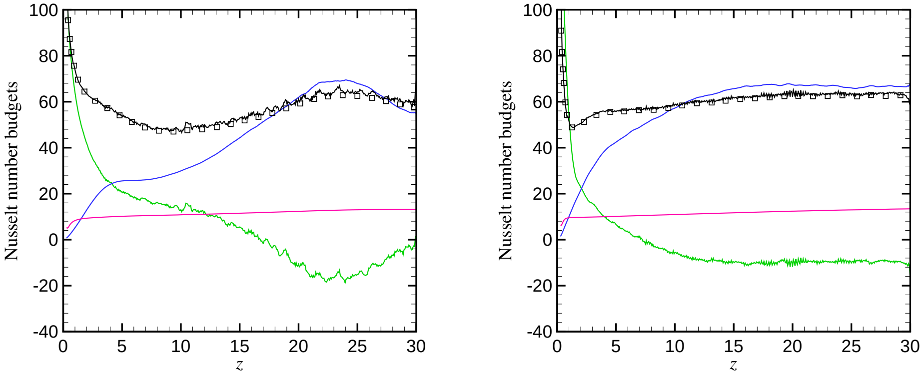

(c) Case D (d) Case E

Figure 3.42: Componential contributions to the Nusselt number. The lines indicate the individual terms as given in Eq. (A.9) and the symbols indicate the locally computed skin friction Nu. Black - Nu_{FIK}; pink - H_I; blue - H_{II}; green - H_{III}.

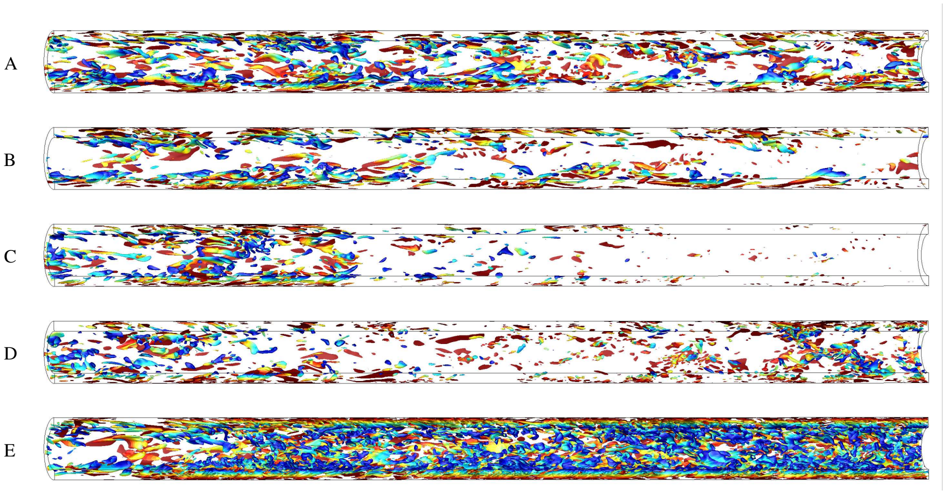

Figure 3.43: Iso-vorticity surfaces $\omega'_z = \pm 150$ for $z = 0 - 15$ for different cases.

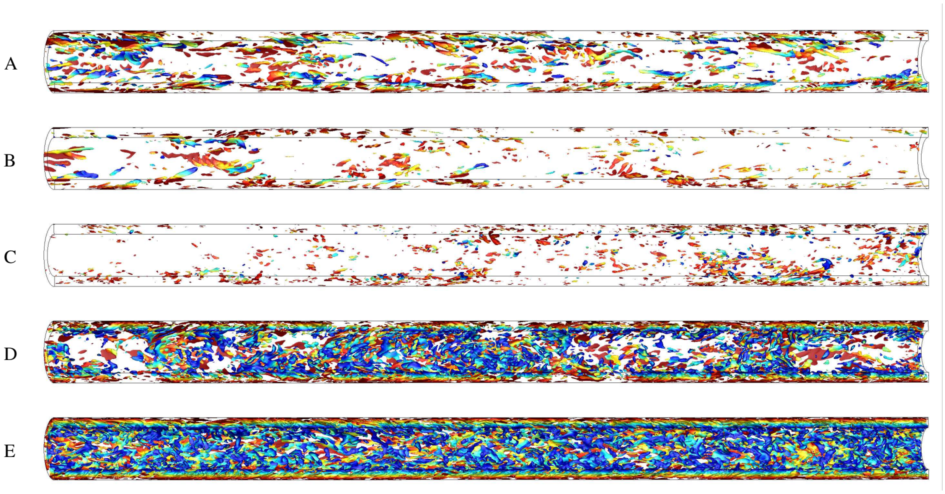

Figure 3.44: Iso-vorticity surfaces $\omega'_z = \pm 150$ for $z = 15 - 30$ for different cases.

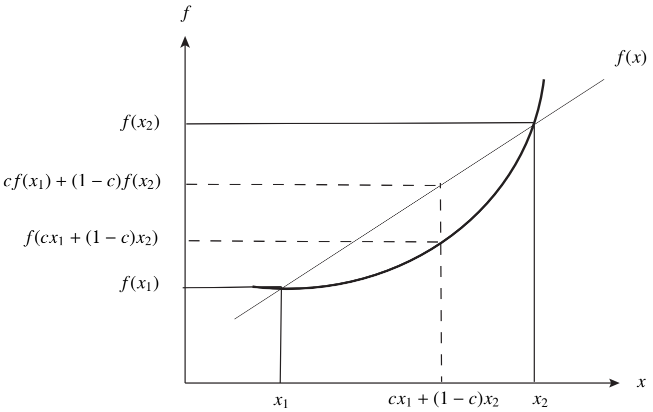

(a) Convex function

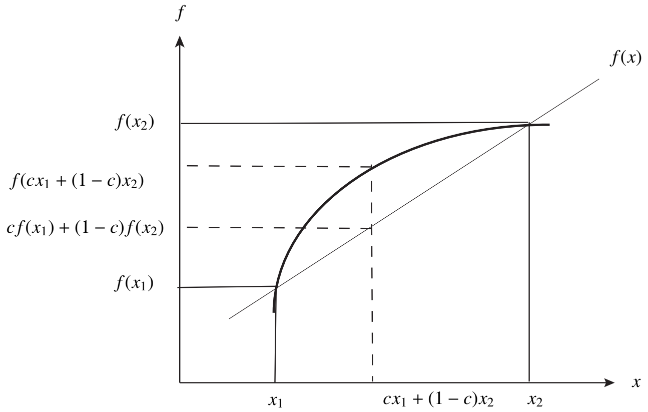

(b) Concave function

Figure 3.45: Jensen inequality generalizes the statement that a secant line of a convex functions ($\partial^2 f(x)/\partial x^2 > 0$) lies above the graph and for concave functions ($\partial^2 f(x)/\partial x^2 < 0$) lies beneath the graph.

(Jensen, 1906) (figure 3.45(a)); the opposite is true for concave transformation (figure 3.45(b)). According to the Jensen inequality,

$$\sum p_k f(x_k) \geq f(\sum p_k x_k), \tag{3.16}$$

where $1 \leq k \leq n$, $p_1, ..., p_n$ are positive numbers, which sum to 1 and f is a real continuous function that is convex ($\partial^2 f(x)/\partial x^2 > 0$). If f is concave ($\partial^2 f(x)/\partial x^2 < 0$) the inequality becomes $\sum p_k f(x_k) \leq f(\sum p_k x_k)$. Translated into Reynolds/Favre averaging with $p_k = 1/N$ the averaging operator, f a thermophysical property ϕ and x_k the enthalpy h_k, we get

$$\frac{1}{N}\sum \phi(h_k) \geq \phi(\frac{1}{N}\sum h_k). \tag{3.17}$$

This can be written as

$$\overline{\phi} \geq \phi(\tilde{h}), \quad \text{if } \phi \text{ is convex}, \tag{3.18}$$

$$\text{and } \overline{\phi} \leq \phi(\tilde{h}), \quad \text{if } \phi \text{ is concave}. \tag{3.19}$$

Consequently, this inequality also generates an additional closure problems in terms of turbulence modelling, as $\overline{\phi}$ is not a prior known. Figure 3.46 demonstrates the Jensen inequality for all thermophysical properties for case A. The DNS averaged properties are compared with properties calculated using Reynolds and Favre averaged enthalpy $\overline{h}$, $\tilde{h}$ and Reynolds averaged temperature $\overline{T}$. The deviations for c_p and λ are large with respect to both $\tilde{h}$ and $\overline{T}$. It can also be seen that $\overline{c_p} < c_p(\tilde{h})$ in the concave part and $\overline{c_p} > c_p(\tilde{h})$ in the convex part. For ρ and μ the inequality is negligible with respect to $\tilde{h}$, however using $\overline{T}$ shows large differences. This is caused by the larger curvature of the functional relation between temperature and the thermophysical properties. Since the Jensen inequality is most significant for c_p, further discussion will be focused on c_p only.

Figure 3.47(a) shows the inequality for c_p for cases A and D at $z = 15$. At both case the values for $c_p(\tilde{h})$ show the same peak value. This is because $c_p(\tilde{h})$ is interpolated on a continuous distribution of $\tilde{h}$ and at the pseudo-critical point, $c_p(\tilde{h})$ has its maximum. However, the peak of $\overline{c_p}$ changes its magnitude in both locations. The different peak values are due to the turbulent enthalpy fluctuations only, as the functional relation (convexity/concavity) between c_p and $\tilde{h}$ does not change. The probability density function of this fluctuations will also influence this inequality. Consequently, the Jensen inequality is an averaging artefact that depends on the curvature of the function and the fluctuations of the averaging quantity. The higher the curvature and the fluctuations, the higher the differences between $\overline{\phi}$ and $\phi(\tilde{h})$. In order to estimate the extent of the Jensen inequality it is suggested to use the enthalpy variance $h''_{rms} = \sqrt{\overline{\rho h'' h''}/\overline{\rho}}$ as a parameter. Figure 3.47(b) shows h''_{rms} for case A and D $z = 15$. It can be seen that, case D which exhibits a lower enthalpy variance, also results in a lower difference between $\overline{c_p}$ and $c_p(\tilde{h})$. This also provides a basis for modelling turbulence to account for the extent of the Jensen inequality.

The dependence of the Jensen inequality on the enthalpy variance is shown in the previous paragraph. However, it is interesting to point out that a sharp curvature of

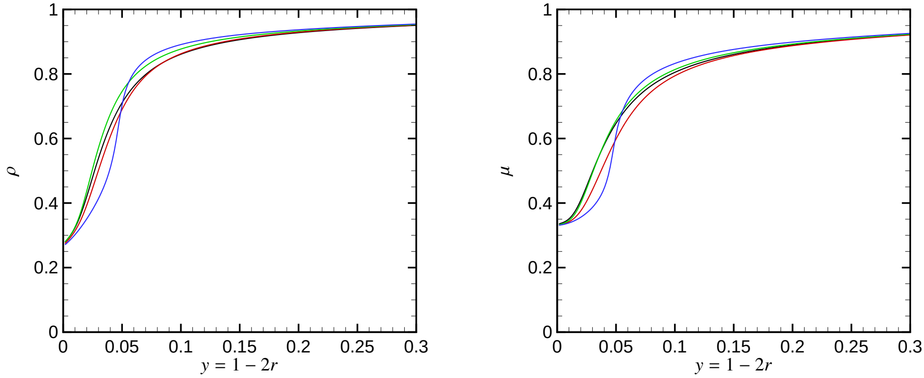

(a) Density ρ (b) Dynamic viscosity μ

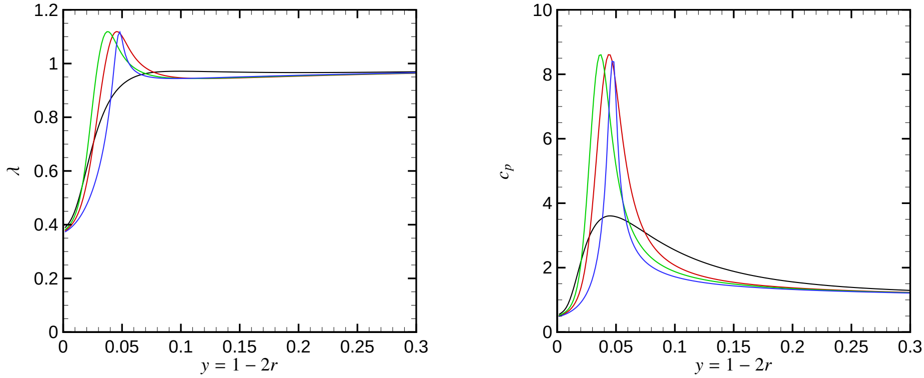

(c) Thermal conductivity λ (d) Isobaric heat capacity c_p

Figure 3.46: Effect of the Jensen inequality on averaging of thermophysical property (ϕ) at $z = 15$ for case A. Black - $\overline{\phi}$; red - $\phi(\overline{h})$; green - $\phi(\tilde{h})$; blue - $\phi(\overline{T})$.

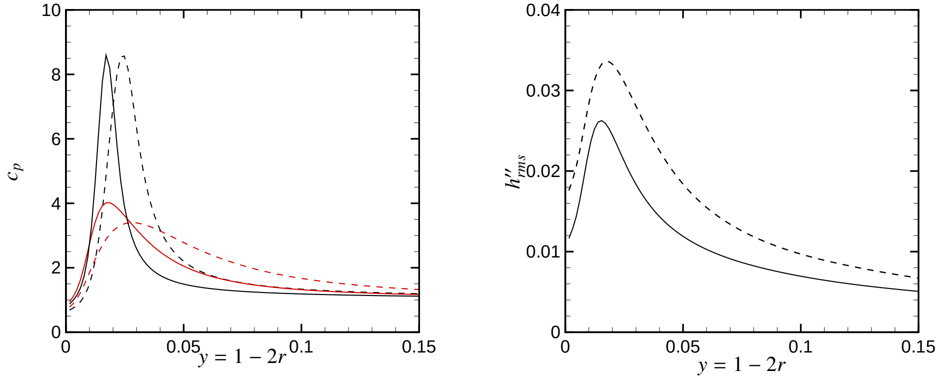

(a) $\overline{c_p}$ and $c_p(\tilde{h})$

(b) Variation of enthalpy variance h''_{rms}

Figure 3.47: Jensen inequality on averaging of $\overline{c_p}$ and $c_p(\tilde{h})$ and variation of enthalpy variance h''_{rms} at $z = 15$. Solid lines - case A; dashed line - case C; red - $\overline{c_p}$; black - $c_p(\tilde{h})$.

thermophysical properties also plays a dominant role in the production of the enthalpy variance. The production term in the enthalpy variance transport equation can be written as

$$P_{\widetilde{h''^2}} = -2\overline{\rho u_r'' h''}\frac{\partial \tilde{h}}{\partial r} - 2\overline{\rho u_z'' h''}\frac{\partial \tilde{h}}{\partial z} + 2\overline{h''\frac{1}{r}\frac{\partial}{\partial r}(r\alpha\frac{\partial \tilde{h}}{\partial r})} + 2\overline{h''\frac{\partial}{\partial z}(\alpha\frac{\partial \tilde{h}}{\partial z})}. \tag{3.20}$$

The two dominant terms are $-2\overline{\rho u_r'' h''}\frac{\partial \tilde{h}}{\partial r}$ and $2\overline{h''\frac{1}{r}\frac{\partial}{\partial r}(r\alpha\frac{\partial \tilde{h}}{\partial r})}$, where the second term can further be decomposed as

$$2\overline{h''\frac{1}{r}\frac{\partial}{\partial r}(r\alpha\frac{\partial \tilde{h}}{\partial r})} = 2\overline{h''\frac{1}{r}\frac{\partial (r\alpha)}{\partial r}}\frac{\partial \tilde{h}}{\partial r} + 2\overline{h''\alpha}\frac{\partial^2 \tilde{h}}{\partial r^2}. \tag{3.21}$$

The first term on the right hand side is significant for fluids with strong α variations and contributes to the production of the enthalpy variance.

3.3.8 The effects of bulk viscosity

In order to examine the effect of bulk viscosity μ_b on heated turbulent flow at supercritical pressures, case A has also been simulated including the temperature-dependent bulk viscosity at $P_0 = 80$ bar. No significant differences are observed. The reason is that the local dilation (see Eqs. (2.13-2.15)) is very small compared to the strain rate (the ratio is $\approx O(10^{-3})$), while the ratio of μ_b/μ is $\approx O(10)$.

3.4 Conclusion

DNS of heated pipe flows with CO_2 above the supercritical pressure were performed to study the effect of buoyancy and large thermophysical property variations on the mean flow statistics. We report turbulent statistics, which have not been discussed in the literature, such as turbulent shear stress, radial turbulent heat flux, turbulent kinetic energy and its shear and buoyant production rates. Different cases, with forced convection and with mixed convection in upward and downward flows are discussed and the observations for first five cases are summarised below:

1. In case A (forced convection), flow acceleration $\partial \tilde{u}_z / \partial z > 0$ due to thermal expansion causes a reduction in turbulent kinetic energy in the downstream direction. The wall temperature shows a monotonous increase due to deteriorating turbulence.

2. In case B (upward mixed convection with small buoyancy), the trend of turbulent statistics is the same as that of case A, but with a higher reduction in turbulence and hence a further increase of wall temperature. The flow acceleration due to thermal expansion is augmented by local flow accelerations due to buoyancy. The structural effect of buoyancy is of minor significance in this case.

3. In case C (upward mixed convection with moderate buoyancy), the deterioration of heat transfer is followed by a recovery of turbulence which starts at the very end of the pipe. The wall temperature shows an increase in the deterioration region (higher temperature than case A), whereas in the recovery region it decreases to values lower than case A. In the deterioration region, the Reynolds shear stress decreases (becoming negative) at locations slightly away from the wall. Recovery starts after the Reynolds shear stress is negative in most of the radial domain (except close to the wall). It is observed that both structural and external effects of buoyancy play a significant role in the recovery process.

4. In case D (upward mixed convection with high buoyancy), similar to case C, the deterioration of heat transfer is followed by a recovery of turbulence. Even though the deterioration of turbulence is larger as compared to case A, the wall temperature remains lower due to the higher flow acceleration. In the deterioration region, the deformation of Reynolds shear stress profile to negative values start much earlier than case C and the reaches the values that are larger than the inlet. The role of structural and external effects of buoyancy on the recovery heat transfer is more pronounced than case C.

5. In case E (downward mixed convection with moderate buoyancy), except for a small region near the inlet, the flow experiences enhancement of heat transfer for the entire pipe. The Reynolds shear stress continuously increases. In contrary to upward flows, the buoyancy force is in opposite direction of flow and induces deceleration at near-wall region and acceleration at core region which results in

flatter velocity profiles (external effects). The buoyancy production (structural effect) in this case is always positive which favours the turbulent kinetic energy.

We furthermore highlight additional first and second-order moments in the mean flow equations. They are found to be of major significance in the mean energy equation, where they strongly modify the average heat flux distribution at- and close to the wall. The smaller effect of property fluctuations on the mean momentum was observed. However, they might play a large role in the energy budgets of the Reynolds stresses. The same holds the energy budgets of the turbulent heat fluxes.

We derived two identities from the streamwise momentum equations and energy equations in order to investigate componential contributions to the skin friction coefficient and the Nusselt number, respectively. The sum of all terms of these identities is compared with the locally calculated skin friction coefficient and Nusselt number and a perfect agreement is obtained ensuring correctness and consistency of the derivation.

The analysis of the DNS also pointed out that $\overline{c_p}$ deviates significantly from $c_p(\tilde{h})$ because of the Jensen inequality. It was shown that the larger the enthalpy fluctuation, the larger the difference between $\overline{c_p}$ and $c_p(\tilde{h})$. Because the additional first and second-order moments appear in the mean flow governing equations, they become important in terms of turbulence modelling where they require closure. Furthermore, the closer the fluid state is to the critical point, the higher the thermophysical property variations. This will cause the effects observed herein to increase further.

4

The effect of thermal boundary conditions on forced convection heat transfer to fluids at supercritical pressure

The contents of this chapter appeared in:

Nemati, H., Patel, A., Boersma, B.J. & Pecnik, R.
J. Fluid Mech., **800**, 531-556 (2016)

In this chapter we use DNS to study the effect of thermal boundary conditions on developing turbulent pipe flows with fluids at supercritical pressure. Two different thermal wall boundary conditions are studied: one that permits temperature fluctuations and one that does not allow temperature fluctuations at the wall (equivalent to cases where the thermal effusivity ratio approaches infinity and zero, respectively). Unlike for turbulent flows with constant thermophysical properties and Prandtl numbers above unity–where the effusivity ratio has a negligible influence on heat transfer–supercritical fluids shows a strong dependency on the effusivity ratio. We observe a reduction of 7% in Nusselt number when the temperature fluctuations at the wall are suppressed. On the other hand, if temperature fluctuations are permitted, large property variations are induced that consequently cause an increase of wall-normal velocity fluctuations very close to the wall and thus an increased overall heat flux and skin friction.

4.1 Introduction

As already discussed in the previous chapter, owing to the unusual thermophysical properties the heat transfer at a supercritical pressure is very different from that at sub-critical pressures. It was shown that property fluctuations, in the case of an isoflux wall boundary condition significantly affect the mean energy transfer and strongly modify the average heat flux distribution at- and close to the wall. This motivated us to study the effect of the thermal effusivity ratio on heat transfer to supercritical fluids.

The thermal effusivity ratio K (also called the thermal activity ratio) describes the ability of two materials to exchange heat. The thermal effusivity is defined as the square root of the product of density, thermal conductivity and specific heat capacity, namely $e = \sqrt{\rho \lambda c_p}$ (Carslaw & Jaeger, 1959). For example, if two semi-infinite materials with different temperatures T_1 and T_2 are brought into contact, the equilibrium contact temperature is a function of $K = e_2/e_1$, expressed as $T_c = (T_1 + KT_2) / (1 + K)$. It follows that for $K \gg 1$, the contact temperature is closer to T_2, while for $K \ll 1$ it is closer to T_1. In the case of heat transfer between a turbulent flow and a solid, the thermal effusivity ratio ($K{=}e_{\text{fluid}}/e_{\text{solid}}$) not only determines the averaged contact temperature but also whether wall temperature fluctuations are allowed or suppressed. Kasagi *et al.* (1989) investigated the effect of thermal effusivity ratio, wall thickness and Prandtl number on wall temperature fluctuations and turbulent heat transfer. They found that for thick solid walls and $K \rightarrow 0$, no temperature fluctuations can occur, such that the thermal boundary condition can be approximated as an ideal isothermal wall. This condition is met for combinations of air and most solid materials and for water if heated or cooled by a thick copper wall. On the other hand, for $K \rightarrow \infty$ the wall heat flux can be described by an ideal isoflux wall boundary condition. For values of $K \approx 1$, such as water and glass, temperature fluctuations at the wall are approximately 50% to that of an ideal isoflux wall. Kasagi *et al.* (1989) also investigated the effect of wall thickness on temperature fluctuations. For fluids with $Pr \approx 1$ and a thermal conductivity a hundred times lower than that of the solid, temperature fluctuations are independent for wall thicknesses larger than the non-dimensional wall distance of $y^+ \approx 100$ of the fluid. By decreasing the wall thickness, the temperature fluctuations approach the value of the ideal isoflux condition, even for $K \ll 1$. Later, Tiselj *et al.* (2001*a*) confirmed the results of Kasagi *et al.* (1989) by performing DNS of fully developed turbulent channel flows with conjugate heat transfer by varying values of wall thickness, effusivity ratio and Prandtl number.

Kays & Crawford (1993) found that in a fully developed turbulent pipe flow the effects of temperature fluctuations on heat transfer vanish with increasing Prandtl number and that the Nusselt number for isoflux and isothermal boundary conditions are equal if $Pr \geq 0.7$. This can be explained by the thickness of thermal resistance region, which depends on the Prandtl number. For fluids with $Pr \ll 1$ the dominant heat transfer mechanism is thermal conduction, which causes the thermal resistance region to move toward the centre of the pipe. In this case, different thermal wall boundary conditions have a large influence on temperature fluctuations and consequently heat transfer from the wall. A higher value of Pr causes the thermal resistance region to move closer to the wall, such that the vanishing (small) velocity fluctuations very close to the wall mitigate the effect of temperature fluctuations on the wall-normal turbulent heat flux. Studies on flat plate boundary layers with respect to different thermal boundary conditions were performed by Kong *et al.* (2000) and Li *et al.* (2009). They showed that close to the wall the behaviour of the wall-normal heat flux for isothermal wall boundary conditions is similar to that of the Reynolds shear stress, implying consistency between temperature and streamwise velocity. They also confirmed that the mean temperature profiles and the streamwise Stanton number ($St = Nu/(RePr)$) distributions are independent of the boundary condition for Prandtl numbers above unity. Further studies on this topic have been performed by Iritani *et al.* (1985); Hetsroni & Rozenblit (1994); Mosyak *et al.* (2001); Verzicco & Sreenivasan (2008), who also investigated the effect of thermal wall boundary condition on wall temperature fluctuations and turbulent heat transfer.

In this chapter, we investigate the influence of thermal wall boundary conditions, namely isothermal ($K \rightarrow 0$) and isoflux ($K \rightarrow \infty$), on heat transfer to fluids with large property variations and high Prandtl numbers. The configuration is a heated developing pipe flow with supercritical CO_2 at a pressure of 80 bar. The fluid temperature at the inlet is slightly below the thermodynamic pseudo-critical point and the fluid is heated at the wall, such that the fluid crosses a region where strong thermophysical property variations occur. If supercritical CO_2 at 80 bar is considered as the heat transfer medium in a heat exchanger made of stainless steel, the effusivity ratio at the pseudo-critical temperature is of the order of $K = 0.15$. Thus, it can be expected that considerable temperature fluctuations at the wall can occur, which can be estimated to approximately 20% that of an ideal isoflux boundary conditions for thick walls. For thin walls, the fluctuations can be even higher. However, the Prandtl number close to the pseudo-critical point is approximately 14 (see figure 2.9(d)) and the effect of the thermal boundary conditions–and thus wall temperature fluctuations–on the turbulent heat transfer should be negligible. As we will outline in this work, this is not the case for fluids with large property variations.

The organisation of the chapter is as follows. Section 4.2 discusses the simulation set-up and boundary conditions. Section 4.3 outlines the results for the instantaneous fields (section 4.3.1), mean and turbulence statistics (section 4.3.2), quadrant analysis of the Reynolds shear stress and the turbulent heat flux (section 4.3.3) and turbulence budgets in section 4.3.4. In section 4.3.5, we exploit the FIK identity to examine the componential contributions to skin-friction and Nusselt number. The summary of the results is given in section 4.4.

4.2 Thermal boundary conditions and simulation set-up

Before we discuss the numerical details and the results, it is necessary to outline the procedure for setting the thermal boundary conditions in our simulations. The aim of this work is to investigate the effect of wall temperature fluctuations on the Nusselt number for flows with variable thermophysical properties. Therefore, it is crucial that the thermodynamic conditions for all the investigated cases are equivalent, such that the observed effects on heat transfer only depend on wall temperature fluctuations and not on different thermodynamic states (note, the thermophysical properties depend on the absolute value of temperature).

Kong *et al.* (2000) and Li *et al.* (2009) investigated the effect of zero/non-zero wall temperature fluctuations on the Nusselt number for constant property fluids by setting isothermal and isoflux boundary condition, respectively. The Nusselt number is defined as $Nu = HL^*_{ref}/\lambda^*_{ref}$, with the heat transfer coefficient H, a reference length L^*_{ref} and a reference thermal conductivity λ^*_{ref} of the fluid. In their simulations, the non-dimensional temperature Θ, the thermal wall boundary condition and the Nusselt number Nu for $K \to 0$ and $K \to \infty$ can be summarised as follows,

$$K \to 0: \quad \Theta = \frac{T^*_{wall} - T^*}{T^*_{wall} - T^*_\infty}, \quad \Theta|_{wall} = 0, \quad Nu = \left.\frac{\partial \overline{\Theta}}{\partial y}\right|_w, \tag{4.1}$$

$$K \to \infty: \quad \Theta = \frac{T^*_\infty - T^*}{q^*_{wall} L^*_{ref}/\lambda^*_{ref}}, \quad \left.\frac{\partial \Theta}{\partial y}\right|_{wall} = 1, \quad Nu = \frac{1}{\overline{\Theta}}, \tag{4.2}$$

where T^*_∞ is the free stream temperature, T^*_{wall} is the wall temperature and q^*_{wall} is the wall heat flux. Note, the bar in (4.1) and (4.2) indicates Reynolds averaging to properly define the average Nusselt number. It is apparent that for constant thermophysical properties, the Nusselt number in (4.1) and (4.2) only depends on the non-dimensional temperature Θ.

If the thermophysical properties are a function of temperature, the Nusselt number not only depends on the temperature, but also on the thermal conductivity as follows

$$Nu = \frac{\overline{\lambda^* \frac{\partial T^*}{\partial y^*}}\Big|_w}{\lambda^*_{ref}(T^*_w - T^*_b)/L^*_{ref}} \,. \tag{4.3}$$

Moreover, it is also not possible to use isoflux and isothermal boundary conditions and to ensure the same thermodynamic conditions at the wall.

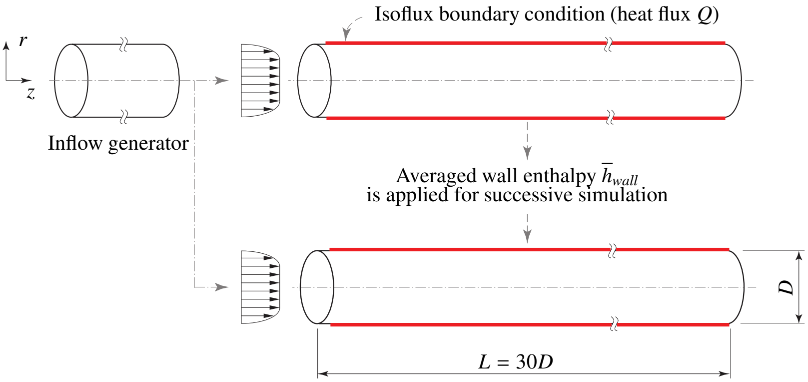

Figure 4.1: Simulation set-up: an inflow generator is used to provide a fully developed turbulent flow for the developing pipe flows. A simulation with constant heat flux is performed first, which then provides the averaged wall enthalpy for a successive simulation.

We therefore use a different approach. First, we perform a simulation with a constant heat flux boundary condition that corresponds to a solid-fluid configuration with $K \rightarrow \infty$. The averaged wall enthalpy obtained from this simulation is then used for a successive simulation, whereby the wall enthalpy is constant in time but with the same streamwise distribution as obtained from the simulation with the constant wall heat flux. This simulation is associated with a solid-fluid configuration with $K \rightarrow 0$. This procedure of applying a fluctuating and non-fluctuating wall temperature boundary condition is outlined in figure 4.1. The same approach was also performed for the constant property simulations to verify this set-up. Note, an equivalent approach would have been to first perform a simulation with an isothermal wall boundary condition ($K \rightarrow 0$) and then to use the obtained bulk enthalpy increase to calculate the streamwise heat flux distribution for the successive simulation ($K \rightarrow \infty$). Four cases have been investigated: two cases with fluid properties corresponding to supercritical CO_2 at 80 bar and two cases with a constant property fluid. For both pairs, simulations with either a fluctuating or non-fluctuating enthalpy boundary condition at the wall were performed. A summary of all case studies is given in table 4.1.

4.3 Results and discussion

4.3.1 Instantaneous fields

The effects of thermal wall boundary condition on turbulence can be visually highlighted by instantaneous enthalpy fluctuations in a plane parallel to the wall ($\theta - z$) as depicted in figure 4.2. The plane is located at $y^+ = 2.5$ (based on inlet conditions), which corresponds to a wall-normal position of $y = 1 - 2r = 0.012$. It should be noted that all simulations

Case	Fluid properties	Thermal wall boundary condition
$\mathrm{SC}_{K\to\infty}$	supercritical CO_2	isoflux Q =2.4 (case A from chapter 3)
$\mathrm{SC}_{K\to 0}$	supercritical CO_2	averaged wall enthalpy $\overline{h}_{wall}$
$\mathrm{CP}_{K\to\infty}$	constant property	isoflux Q =2.4
$\mathrm{CP}_{K\to 0}$	constant property	averaged wall enthalpy $\overline{h}_{wall}$

Table 4.1: Case studies corresponding to thermal wall boundary conditions and fluid properties.

use an identical inflow velocity field and that the enthalpy fluctuations are plotted at the same time instant.

As seen in figure 4.2, turbulent structures are clearly observed in enthalpy fluctuations and differences between $\mathrm{SC}_{K\to\infty}$ and $\mathrm{SC}_{K\to 0}$ are visible. The regions of low and high enthalpy fluctuations are stronger for $\mathrm{SC}_{K\to\infty}$ as compared to $\mathrm{SC}_{K\to 0}$. Similar differences in near-wall scalar fluctuations for incompressible boundary layers were reported by Kong *et al.* (2000) and Li *et al.* (2009). The plot also shows a decrease in streamwise coherency for $\mathrm{SC}_{K\to 0}$. In order to quantify the change in coherency, figure 4.3 shows the streamwise autocorrelation function, defined as

$$\mathrm{p}_{zz}(\pm s) = \frac{\overline{\sqrt{\rho(r,z)}h''(r,z)\sqrt{\rho(r,z\pm s)}h''(r,z\pm s)}}{\overline{\rho(r,z)h''(r,z)h''(r,z)}} \tag{4.4}$$

at $y^+ = 2.5$ (based on inlet condition) for both $\mathrm{SC}_{K\to\infty}$ and $\mathrm{SC}_{K\to 0}$ cases. It can be seen that, the autocorrelation function clearly indicates shorter structures for case $\mathrm{SC}_{K\to 0}$ as compared to $\mathrm{SC}_{K\to\infty}$. Furthermore, small-scale structures (ripples) can be observed in figure 4.2, which emerge after approximately $z > 10$ at the shear layers between the streaks that separate hot and cold fluid regions. The strong gradients of viscosity and density across the shear layer cause destabilising effects (Govindarajan & Sahu, 2014). Similar small-scale structures were also observed in Duan *et al.* (2010) for the case with strong wall cooling.

4.3.2 Mean flow and turbulence statistics

Figure 4.4(a) shows the distribution of bulk enthalpy in the streamwise direction for all four cases. Based on the overall energy conservation, it follows that for cases with constant wall heat flux (cases $\mathrm{SC}_{K\to\infty}$ and $\mathrm{CP}_{K\to\infty}$) the distribution of the bulk enthalpy increases linearly as a function of z, namely $h_b = 4Qz/\left(Re_{b0}Pr_0\right)$. The bulk enthalpy is defined as $h_b = \int_0^R \overline{\rho w h} r dr / \int_0^R \overline{\rho w} r dr$. As can be seen, the symbols for the constant property cases $\mathrm{CP}_{K\to\infty}$ and $\mathrm{CP}_{K\to 0}$ overlap, which highlights that the boundary condition has no influence on the global energy balance. This result agrees well with the

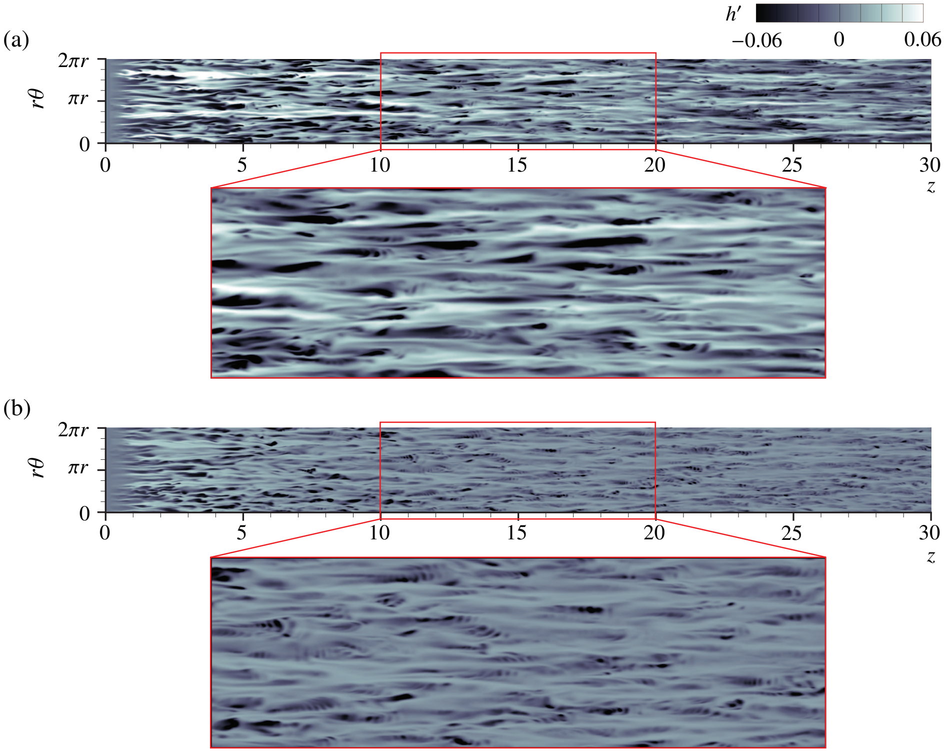

Figure 4.2: Instantaneous enthalpy fluctuations h' in $\theta - z$ at $y^+ = 2.5$ (based on inlet condition). (a) $SC_{K\rightarrow\infty}$ and (b) $SC_{K\rightarrow 0}$.

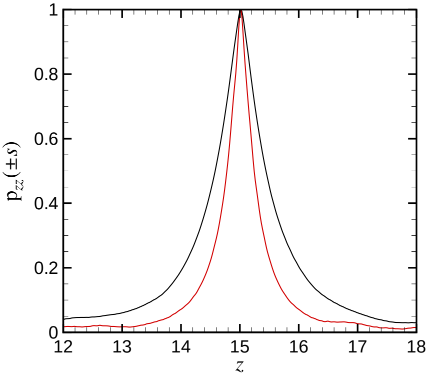

Figure 4.3: Two-point spatial correlation of enthalpy fluctuations $p_{zz}(\pm s)$ at $y^+ = 2.5$ (based on inlet condition). Black - $SC_{K\rightarrow\infty}$; red - $SC_{K\rightarrow 0}$.

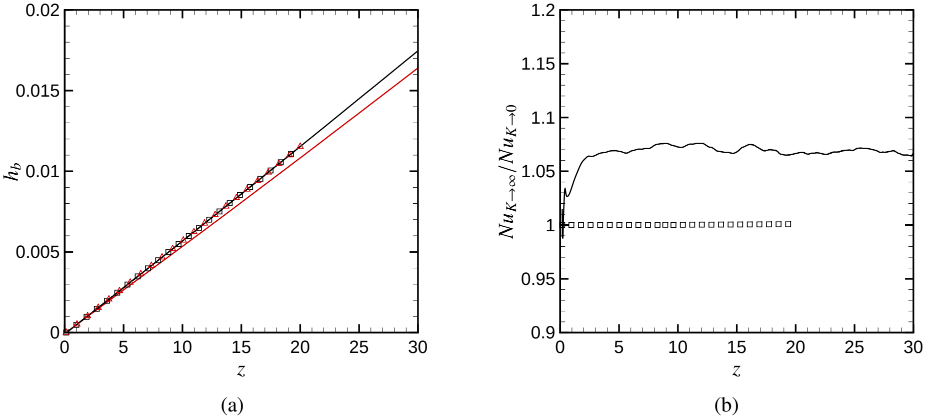

Figure 4.4: (a) Comparison of streamwise distributions of the bulk enthalpy h_b. Black line - SC$_{K\to\infty}$; red line - SC$_{K\to 0}$; black symbols - CP$_{K\to\infty}$; red symbols - CP$_{K\to 0}$. (b) Nusselt number ratio along the pipe. Lines - supercritical fluid; symbols - constant property fluid.

observation from previous studies (Kays & Crawford, 1993; Li *et al.*, 2009) and also confirms the consistency of applying the thermal boundary conditions, as described in section 4.2. For the two supercritical fluid cases, however, the bulk enthalpy distributions are affected by the thermal boundary conditions. In figure 4.4(a) it can be seen that less energy is transferred to the fluid if the enthalpy at the wall is non-fluctuating (SC$_{K\to 0}$) and in figure 4.4(b) the Nusselt number ratio ($Nu_{K\to\infty}/Nu_{K\to 0}$) shows that $Nu_{K\to\infty}$ is approximately 7% higher for the case with the fluctuating wall enthalpy boundary condition.

To investigate this, the Nusselt number dependency on the wall boundary condition, we will first analyse mean profiles for the enthalpy, velocity and several turbulence correlations. Figure 4.5 shows the radial distribution of the mean enthalpy–normalised by the value at the wall–and streamwise velocity for all cases investigated at a streamwise location of $z = 15$. Hereafter, all radial profiles are shown at $z = 15$, since this location is representative of almost the entire length of the pipe, except very close to the inlet where the heating of the pipe starts (the region between $z = 0$ and $z \approx 3$). While the constant property cases show no difference with respect to the applied boundary condition, the supercritical cases indicate a small difference. There are higher enthalpy gradients at the wall for SC$_{K\to\infty}$, which support the results of a higher heat flux from the wall. The mean streamwise velocity shows only slightly higher values for SC$_{K\to\infty}$ in the near-wall region. Larger differences are obtained for the enthalpy variance h'_{rms} as shown in figure 4.6 for all four cases at the same streamwise location of $z = 15$. For CP$_{K\to\infty}$ the variance at the wall is non-zero and its slope is zero, while for the case CP$_{K\to 0}$ the value at the wall is zero and its slope is proportional to y. Similar observations were made in

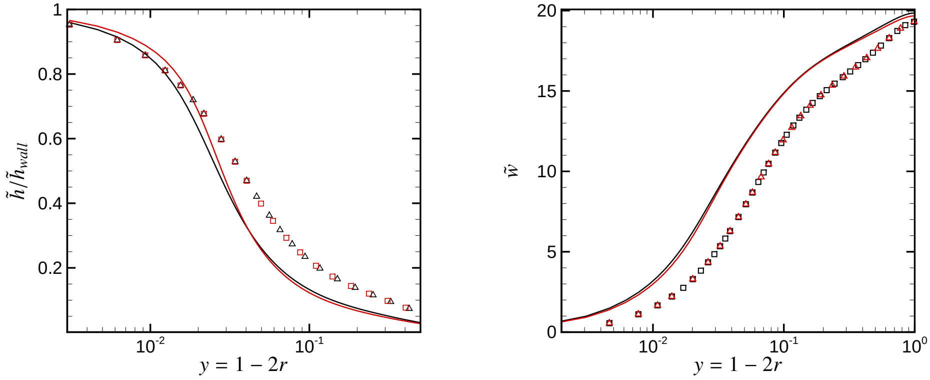

(a) (b)

Figure 4.5: (a) Mean enthalpy $\tilde{h}/\tilde{h}_{wall}$ and (b) streamwise velocity $\tilde{w}$ at $z = 15$. Black line - $\mathrm{SC}_{K\to\infty}$; red line - $\mathrm{SC}_{K\to 0}$; black symbols - $\mathrm{CP}_{K\to\infty}$; red symbols - $\mathrm{CP}_{K\to 0}$.

Tiselj *et al.* (2001*b*); Kong *et al.* (2000); Li *et al.* (2009). The supercritical cases show higher variances for both cases. However, the main difference is that for case $\mathrm{SC}_{K\to\infty}$ the slope of the enthalpy variance at the wall is non-zero. This can be explained by using Reynolds decomposition for the instantaneous heat flux:

$$\overline{\alpha}\frac{\partial \overline{h}}{\partial r}\Big|_{wall} + \alpha'\frac{\partial h}{\partial r}\Big|_{wall} + \overline{\alpha}\frac{\partial h'}{\partial r}\Big|_{wall} = Q \tag{4.5}$$

after multiplication with h', substituting $y = 1 - 2r$ and time averaging we obtain

$$\frac{\partial \overline{h'^2}}{\partial y}\Big|_{wall} = -\frac{\overline{\alpha' h' \frac{\partial h}{\partial y}}}{\overline{\alpha}}\Big|_{wall}. \tag{4.6}$$

Note, for the case $\mathrm{SC}_{K\to\infty}$ the wall heat flux Q is constant and thus the term $h'Q$ vanishes after averaging. When the property fluctuations are present, as they are in case $\mathrm{SC}_{K\to\infty}$ ($\alpha' \neq 0$), the right-hand side of equation (4.6) does not vanish–the consequence is that the gradient of h'_{rms} at the wall is non-zero (see solid line in figure 4.6). The enthalpy variance for the case $\mathrm{SC}_{K\to 0}$ shows a similar behaviour as for $\mathrm{CP}_{K\to 0}$, because the fixed wall enthalpy boundary conditions results in zero and negligible property fluctuations at and close to the wall, respectively.

Next, components of the total radial heat flux are compared for different thermal wall boundary conditions. Using Reynolds decomposition, the heat flux can be decomposed as

$$q_{r,tot} = \overline{\alpha}\frac{\partial \overline{h}}{\partial r} + \overline{\alpha'\frac{\partial h'}{\partial r}} - \overline{\rho u_r'' h''} Re_{\tau 0} Pr_0, \tag{4.7}$$

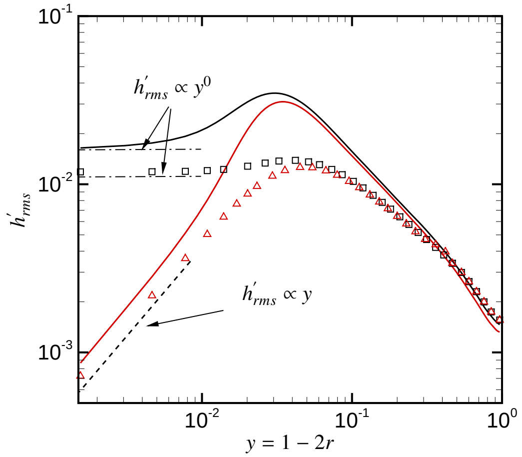

Figure 4.6: Enthalpy fluctuations h'_{rms} at $z = 15$. Black line - $\mathrm{SC}_{K\to\infty}$; red line - $\mathrm{SC}_{K\to 0}$; black symbols - $\mathrm{CP}_{K\to\infty}$; red symbols - $\mathrm{CP}_{K\to 0}$.

where $\overline{\alpha}\partial\overline{h}/\partial r$ is the averaged molecular heat flux, $\overline{\rho u'' h''}$ is the turbulent heat flux and $\overline{\alpha' \partial h'/\partial r}$ is an additional averaging term due to property fluctuations. Their profiles for all cases are shown in figure 4.7 at $z = 15$. As can be seen in figure 4.7(a), the averaged molecular heat flux for the constant property cases is 2.4 at the wall, which corresponds to the specified heat flux value for the case $\mathrm{CP}_{K\to\infty}$; and the different thermal wall boundary conditions (cases $\mathrm{CP}_{K\to\infty}$ and $\mathrm{CP}_{K\to 0}$) have no effect on the overall heat transfer since $Pr \geq 1$. For the supercritical case $\mathrm{SC}_{K\to\infty}$, however, the averaged molecular heat flux at the wall is substantially higher than the specified value of 2.4 (see figure 4.7(b)). The additional term $\overline{\alpha' \partial h'/\partial r}$ in (4.7) causes a negative heat flux contribution of approximately -0.1. For the case $\mathrm{SC}_{K\to 0}$ the wall value for the averaged molecular heat flux $\overline{\alpha}\partial\overline{h}/\partial r$ is below 2.4 and the additional term $\overline{\alpha' \partial h'/\partial r} = 0$. This confirms the decreased heat transfer rate as shown in figure 4.4 when the constant heat flux boundary condition $\mathrm{SC}_{K\to\infty}$ is replaced by its corresponding averaged wall enthalpy in case $\mathrm{SC}_{K\to 0}$.

The effect of thermal wall boundary conditions on the averaged heat flux and the additional term is limited to the near-wall region $y \leq 0.03$, while the turbulent heat flux is affected over the entire cross-section of the pipe. It can be seen that $-\overline{\rho u'' h''}$ for $\mathrm{SC}_{K\to 0}$ is lower than for $\mathrm{SC}_{K\to\infty}$. This difference stems from the correlation between enthalpy h' and density ρ' fluctuations, whereby enhanced density fluctuations ρ' cause increased mass fluctuations and consequently larger velocity fluctuations.

This is quantified in figure 4.8 by means of probability density functions (PDF) of radial u'' and streamwise w'' velocity fluctuations and the turbulent shear stress. The radial u'' and streamwise w'' velocity fluctuations are compared at two different wall-normal locations for the cases $\mathrm{SC}_{K\to\infty}$ and $\mathrm{SC}_{K\to 0}$ in figures 4.8(a) and 4.8(b). Two observations

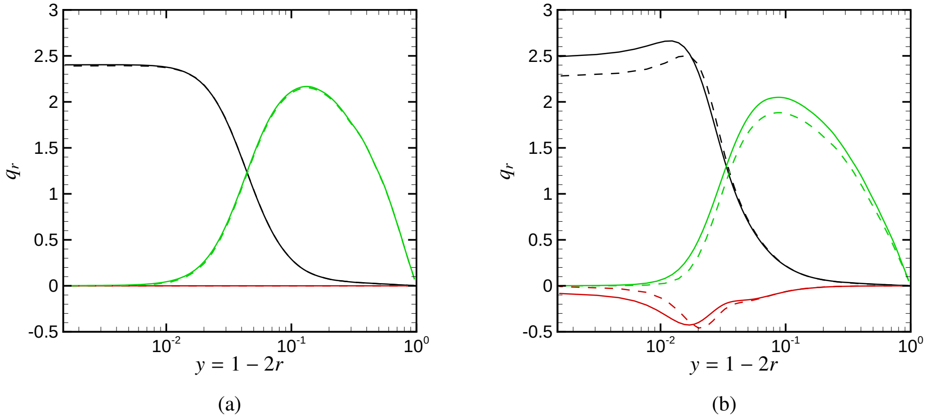

(a)

(b)

Figure 4.7: Wall-normal heat flux q_r at $z = 15$ (a) $\mathrm{CP}_{K\to\infty}$ and $\mathrm{CP}_{K\to 0}$ and (b) $\mathrm{SC}_{K\to\infty}$ and $\mathrm{SC}_{K\to 0}$. Solid lines - $\mathrm{SC}_{K\to\infty}$ and $\mathrm{CP}_{K\to\infty}$; dashed lines - $\mathrm{SC}_{K\to 0}$ and $\mathrm{CP}_{K\to 0}$; black - $\overline{\alpha}\partial\overline{h}/\partial r$; red - $\overline{\alpha'\partial h'/\partial r}$; green - $-\overline{\rho u'' h''} Re_{\tau 0} Pr_0$.

can be made. First, both radial and streamwise velocity fluctuations are higher for $\mathrm{SC}_{K\to\infty}$ than for $\mathrm{SC}_{K\to 0}$ (however, more pronounced in streamwise velocity), which again can be linked to the effect of higher density fluctuations in $\mathrm{SC}_{K\to\infty}$. Second, the velocity fluctuations for both cases increase close to the wall, while they decrease close to the centre if compared to the $\mathrm{CP}_{K\to 0}$ ($\mathrm{CP}_{K\to\infty}$). The latter observation can also be seen from the profile of the Reynolds shear stress, which is plotted in figure 4.8(c) at the same streamwise position for different cases. As discussed in our previous work (Nemati *et al.*, 2015), this is due to flow acceleration by means of thermal expansion, which results in an increase in the bulk velocity. In laminar flows, the thermal expansion increases the convective heat transfer because of flow acceleration. In turbulent convection the effects are opposite (Kim *et al.*, 2008*b*). Although flow acceleration increases the velocity close to the wall, it reduces turbulence production. The wall-normal velocity gradient in the viscous dominant region increases, where it has a small influence on the turbulence production, while further away from the wall the velocity gradient decreases and thus also decreases the turbulence production.

4.3.3 Quadrant analysis

Next, we use the quadrant analysis to examine the effects of thermal effusivity ratio on fractional contributions of instantaneous fluctuations to turbulent heat flux $\overline{\rho u_r'' h''}$ and the turbulent shear stress $\overline{\rho u_r'' u_z''}$. Similar to chapter 2 $\overline{\rho u_r'' h''}$ and $\overline{\rho u'' w''}$ are conditionally averaged into four quadrants of $\sqrt{\rho} u_r'' - \sqrt{\rho} h''$ and $\sqrt{\rho} u_r'' - \sqrt{\rho} w''$ planes. Figure 4.9(a) shows the contributions from each quadrant to the radial turbulent heat flux $\overline{\rho u_r'' h''}$ plotted

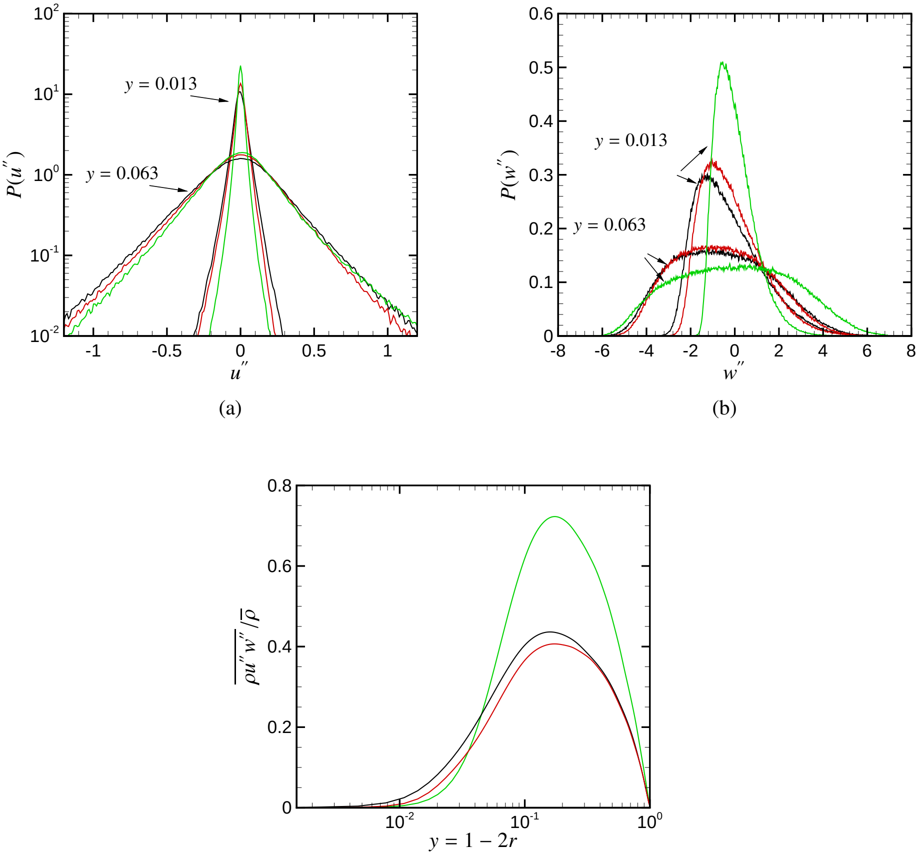

(a)

(b)

(c)

Figure 4.8: (a) PDF of radial velocity fluctuations u'', (b) streamwise velocity fluctuations w'' at two different wall-normal positions and (c) turbulent shear stress profile $\overline{\rho u'' w''}$ at $z = 15$. Black - $\mathrm{SC}_{K\to\infty}$; red - $\mathrm{SC}_{K\to 0}$; green - $\mathrm{CP}_{K\to\infty}$ ($\mathrm{CP}_{K\to 0}$).

as a function of wall-normal coordinate. In the case of non-fluctuating wall temperature (case $\mathrm{SC}_{K\to 0}$), all contributions to the turbulent heat flux are attenuated. It can be seen that the $Q1$ and $Q3$ events, which have the largest contributions, are smaller for case $\mathrm{SC}_{K\to 0}$ than for $\mathrm{SC}_{K\to\infty}$. In other words, for the case $\mathrm{SC}_{K\to 0}$ the hot fluid has less tendency to leave the wall, which consequently leads to the lower heat transfer.

The fractional contributions to the Reynolds shear stress $\overline{\rho u'' w''}$ are shown in figure 4.9(b) for $\mathrm{SC}_{K\to\infty}$ and $\mathrm{SC}_{K\to 0}$. Similar to the turbulent heat flux, all contributions to the Reynolds shear stress are decreased when the fluctuating wall temperature ($\mathrm{SC}_{K\to\infty}$) is changed to the non-fluctuating wall temperature condition ($\mathrm{SC}_{K\to 0}$). Sweep $Q1$ and ejection $Q3$ events, which have positive contributions to the Reynolds shear stress, show the largest differences.

4.3.4 Turbulence budgets

To study the effect of different enthalpy wall boundary conditions on the averaged transport equation for turbulence kinetic energy and wall-normal turbulent heat flux, their budgets are examined next. The evolution equation for the Favre-averaged turbulence kinetic energy is $k = \widetilde{u_i'' u_i''}/2$ can be written as follows (Huang *et al.*, 1995):

$$\frac{\partial \bar{\rho} k}{\partial t} + C_k = P_k + T_k + \Pi_k + \Phi_k + V_k + \epsilon_k + E_k^{(1)} + E_k^{(2)}, \tag{4.8}$$

with

$$C_k = \frac{\partial \bar{\rho} \tilde{u}_j k}{\partial x_j}, \quad P_k = -\bar{\rho}\widetilde{u_i'' u_j''}\frac{\partial \tilde{u}_j}{\partial x_i}, \quad T_k = -\frac{1}{2}\frac{\partial \bar{\rho}\widetilde{u_i'' u_i'' u_j''}}{\partial x_j},$$

$$\Pi_k = -\frac{\partial \overline{p' u_j''}}{\partial x_j}, \quad \Phi_k = \overline{p'\frac{\partial u_j''}{\partial x_j}}, \quad V_k = \frac{1}{Re_{\tau 0}}\frac{\partial \overline{\tau_{ij}' u_i''}}{\partial x_j},$$

$$\epsilon_k = -\frac{1}{Re_{\tau 0}}\overline{\tau_{ij}'\frac{\partial u_i''}{\partial x_j}}, \quad E_k^{(1)} = \overline{u_i''}\frac{1}{Re_{\tau 0}}\frac{\partial \bar{\tau}_{ij}}{\partial x_j}, \quad E_k^{(2)} = -\overline{u_i''}\frac{\partial \bar{p}}{\partial x_i}, \tag{4.9}$$

where

$$\bar{\tau}_{ij} = \bar{\mu}\left(\frac{\partial \bar{u}_i}{\partial x_j} + \frac{\partial \bar{u}_j}{\partial x_i}\right) + \overline{\mu'\left(\frac{\partial u_i'}{\partial x_j} + \frac{\partial u_j'}{\partial x_i}\right)} - \frac{2}{3}\bar{\mu}\frac{\partial \bar{u}_k}{\partial x_k}\delta_{ij} - \frac{2}{3}\overline{\mu'\frac{\partial u_k'}{\partial x_k}}\delta_{ij}, \quad \tau_{ij}' = \tau_{ij} - \bar{\tau}_{ij}. \tag{4.10}$$

The terms in Eq. (4.9) are mean convection C_k, turbulence production P_k, turbulence diffusion T_k, pressure diffusion Π_k, pressure dilatation Φ_k, viscous diffusion of turbulence kinetic energy V_k, turbulence dissipation ϵ_k and $E_k^{(l)} (l = 1, 2)$ are additional terms due to density and velocity fluctuations. These terms are referred to as additional

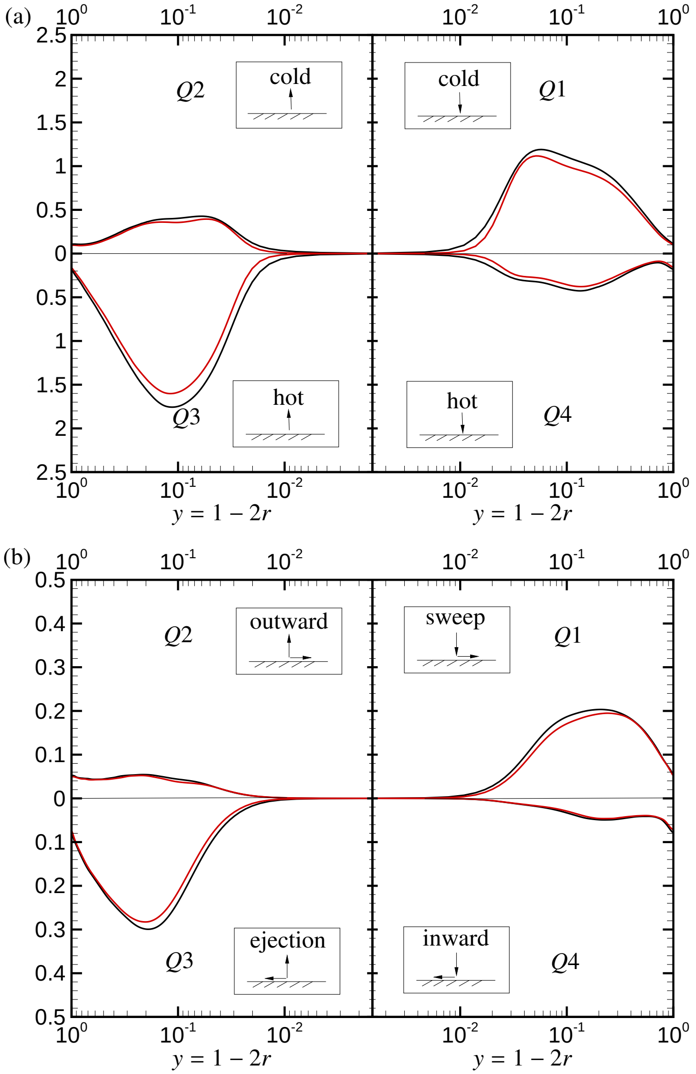

Figure 4.9: Fractional contribution to the (a) radial turbulent heat flux $\overline{\rho u''h''}$ and (b) Reynolds shear stress $\overline{\rho u''w''}$ at $z = 15$. Black - SC$_{K\to\infty}$; red - SC$_{K\to 0}$.

correlations and result from turbulent fluctuations that are responsible for energy exchange between mean and turbulence kinetic energy (see Huang *et al.* (1995)). Emphasis is given to P_k, T_k, V_k, ϵ_k and $E_k = \sum_{l=1}^{2} E_k^{(l)}$ and their profiles are shown in figure 4.10 for all cases at $z = 15$. Note, the budgets for the constant property cases shown in figure 4.10(a) do not change in the streamwise direction since the energy equation is a passive scalar and the velocity field is unaffected by the heat transfer. Thus the profiles in figure 4.10(a) also correspond to the inlet condition for the supercritical cases as shown in figure 4.10(b).

As discussed in our previous work (Nemati *et al.*, 2015), flow acceleration due to thermal expansion causes a decrease in turbulence for the supercritical cases. The production rate in figure 4.10(b) is substantially lower than for the constant property case in figure 4.10(a). The turbulence dissipation also shows a reduction for both supercritical cases, except for $\mathrm{SC}_{K\to\infty}$ very close to the wall. An equivalent effect has been observed in Zonta *et al.* (2012), where they studied the effect of viscosity variations on turbulence statistics in fully developed channel flows. They observed that on the hot side of the channel (low viscosity) the turbulent dissipation decreases above the viscous sublayer, but increases between the viscous sublayer and the wall. The turbulent diffusion T_k is reduced due to the reduction in turbulence caused by flow acceleration and thermal expansion.

With respect to the different boundary conditions, it can be seen that the turbulence production P_k experiences a larger reduction for the non-fluctuating wall enthalpy case $\mathrm{SC}_{K\to 0}$ as compared to $\mathrm{SC}_{K\to\infty}$. This can be further analysed by expanding P_k, in cylindrical coordinates, to

$$P_k = -\overline{\rho u'' u''}\frac{\partial \tilde{u}}{\partial r} - \overline{\rho u'' w''}\frac{\partial \tilde{u}}{\partial z} - \overline{\rho v'' v''}\frac{\tilde{u}}{r} - \overline{\rho u'' w''}\frac{\partial \tilde{w}}{\partial r} - \overline{\rho w'' w''}\frac{\partial \tilde{w}}{\partial z}. \tag{4.11}$$

The product of Reynolds shear stress and streamwise velocity gradient is the dominant source of turbulence kinetic energy production (fourth term in Eq. (4.11)). Based on the results discussed in section 4.3.2, the higher P_k in $\mathrm{SC}_{K\to\infty}$ can thus be explained by the higher Reynolds shear stress $\overline{\rho u'' w''}$ (figure 4.8(c)), since the streamwise velocity gradient shows only small differences in the near-wall region (figure 4.5(b)). The turbulence dissipation in $\mathrm{SC}_{K\to 0}$ is slightly smaller over the entire cross-section of the pipe than it is for $\mathrm{SC}_{K\to\infty}$, but larger differences are observed very close to the wall. This is a direct consequence of the higher gradients in velocity fluctuations for case $\mathrm{SC}_{K\to\infty}$. The larger dissipation in the near-wall region is balanced with a higher energy transfer due to viscous diffusion in the near-wall region for case $\mathrm{SC}_{K\to\infty}$. The turbulence diffusion T_k and the additional terms are less affected by the thermal boundary condition. As can be seen, the additional terms $E_k^{(1)}$ and $E_k^{(2)}$ contribute to the production and sink of turbulence kinetic energy, respectively. Figure 4.11 shows the largest components of $E_k^{(1)}$ and $E_k^{(2)}$ at $z = 15$ for $\mathrm{SC}_{K\to\infty}$ and $\mathrm{SC}_{K\to 0}$. The term $\overline{w''}\left(\partial r \overline{\tau}_{rz}/r\partial r\right)/Re_{\tau 0}$ (part of $E_k^{(1)}$) corresponds to a source (energy is received from the mean flow), whereas the term $-\overline{w''}\partial\overline{p}/\partial z$ (part of $E_k^{(2)}$) corresponds to a sink (energy is transferred to the mean flow) of turbulent kinetic energy. Comparing these two additional terms for the cases $\mathrm{SC}_{K\to\infty}$ and

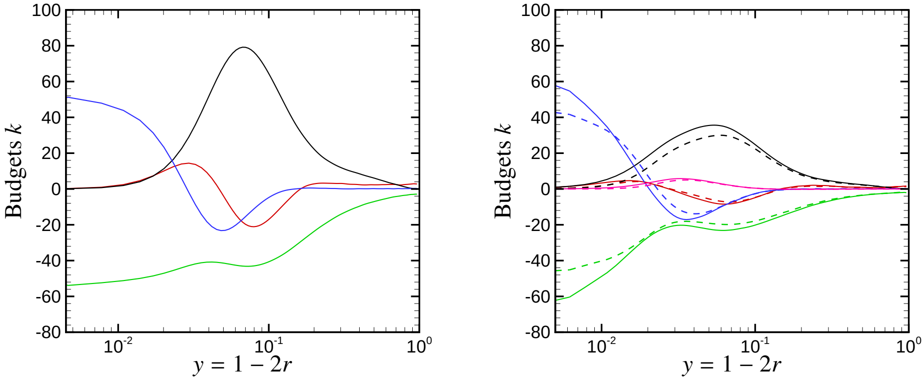

(a) $\mathrm{CP}_{K\to\infty}$ ($\mathrm{CP}_{K\to 0}$)

(b) $\mathrm{SC}_{K\to\infty}$ and $\mathrm{SC}_{K\to 0}$

Figure 4.10: Turbulence kinetic energy $k = 1/2\widetilde{u_i'' u_i''}$ budgets at $z = 15$ (a) $\mathrm{CP}_{K\to\infty}$ ($\mathrm{CP}_{K\to 0}$), (b) solid lines $\mathrm{SC}_{K\to\infty}$ and dashed lines $\mathrm{SC}_{K\to 0}$. Black - P_k; red - T_k; green - ϵ_k; blue - V_k; pink - E_k. Note, the profiles for $\mathrm{CP}_{K\to\infty}$ ($\mathrm{CP}_{K\to 0}$) are equivalent to $z = 0$ for the SC cases.

$\mathrm{SC}_{K\to 0}$, it is possible to observe a reduction in magnitude for $\mathrm{SC}_{K\to 0}$ that stems from the difference in streamwise velocity fluctuations (see figure 4.8(b)) in the near-wall region.

Similar to the turbulence kinetic energy, an evolution equation for the Favre-averaged turbulent heat flux can be formulated as:

$$\frac{\partial \overline{\rho u_i'' h''}}{\partial t} + C_{e,i} = P_{e,i} + T_{e,i} + \Pi_{e,i} + V_{e,i} + \epsilon_{e,i} + E_{e,i}, \tag{4.12}$$

with

$$\begin{gathered}
C_{e,i} = \frac{\partial \tilde{u}_j \overline{\rho u_i'' h''}}{\partial x_j}, \quad P_{e,i} = -\overline{\rho u_j'' h''}\frac{\partial \tilde{u}_i}{\partial x_j} - \overline{\rho u_i'' u_j''}\frac{\partial \tilde{h}}{\partial x_j}, \quad T_{e,i} = -\frac{\partial \overline{\rho u_i'' u_j'' h''}}{\partial x_j}, \\
\Psi_{e,i} = -\overline{h'' \frac{\partial p'}{\partial x_i}}, \quad V_{e,i} = \frac{1}{Re_{\tau 0}} \frac{\partial \overline{\tau_{ij}' h''}}{\partial x_j} + \frac{1}{Re_{\tau 0} Pr_0} \frac{\partial \overline{q_j' u_i''}}{\partial x_j}, \\
\epsilon_{e,i} = -\frac{1}{Re_{\tau 0}} \overline{\tau_{ij}' \frac{\partial h''}{\partial x_j}} - \frac{1}{Re_{\tau 0} Pr_0} \overline{q_j' \frac{\partial u_i''}{\partial x_j}}, \\
E_{e,i}^{(1)} = \overline{h''}\left(\frac{1}{Re_{\tau 0}} \frac{\partial \overline{\tau}_{ij}}{\partial x_j} - \frac{\partial \overline{p}}{\partial x_i}\right), \quad E_{e,i}^{(2)} = \frac{1}{Re_{\tau 0} Pr_0} \overline{u_i''} \frac{\partial \overline{q}_j}{\partial x_j},
\end{gathered} \tag{4.13}$$

where

$$\overline{q}_i = -\overline{\alpha} \frac{\partial \overline{h}}{\partial x_j} - \overline{\alpha' \frac{\partial h'}{\partial x_j}}, \quad q_i' = q_i - \overline{q}_i. \tag{4.14}$$

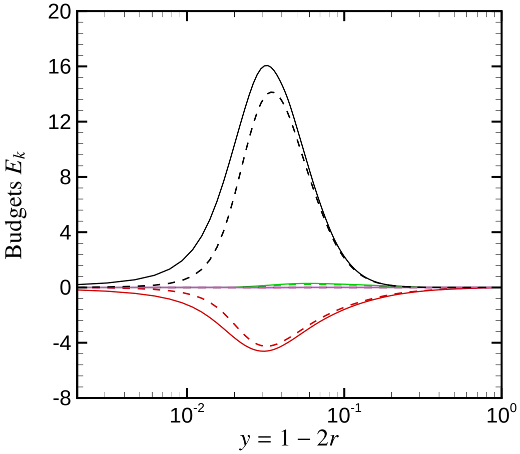

Figure 4.11: Largest components of $E_k^{(1)}$ and $E_k^{(2)}$. Solid lines - SC$_{K\to\infty}$; dashed lines - SC$_{K\to 0}$; black - $\overline{w''}\left(\partial r\overline{\tau}_{rz}/r\partial r\right)/Re_{\tau 0}$; red - $-\overline{w''}\partial\overline{p}/\partial z$.

Here the terms are mean convection $C_{e,i}$, production $P_{e,i}$, turbulence diffusion $T_{e,i}$, enthalpy–pressure-gradient correlation $\Psi_{e,i}$, molecular diffusion $V_{e,i}$, dissipation of turbulent heat flux $\epsilon_{e,i}$ and $E_{e,i}^{(l)}(l = 1, 2)$ are additional terms that stem from density, velocity and enthalpy fluctuations. Figure 4.12 shows profiles of $P_{e,r}$, $\Psi_{e,r}$, $V_{e,r}$, $\epsilon_{e,r}$ and $E_{e,r}^{(2)}$ (remaining terms are insignificant) for the constant property and the supercritical pressure cases with different wall enthalpy boundary conditions at $z = 15$. It is evident from figure 4.12(a) that the budgets for the constant property cases with different boundary conditions collapse over a wide range. Only minor differences between CP$_{K\to\infty}$ and CP$_{K\to 0}$ appear for the dissipation $\epsilon_{e,r}$, viscous diffusion $V_{e,r}$ and enthalpy–pressure-gradient correlation $\Psi_{e,r}$ very close to the wall. This is due to the wall enthalpy fluctuations in case CP$_{K\to\infty}$. The production $P_{e,r}$ does not change, because it contains products of turbulent heat flux and velocity gradients and turbulent stresses and enthalpy gradients, see Eq. (4.13). Because none of these terms change (see figure 4.5(a) and 4.7(a)) with respect to thermal boundary conditions, also $P_{e,r}$ is unaffected. The terms $\epsilon_{e,r}$, $V_{e,r}$ and $\Psi_{e,r}$ contain products of h'' with velocity and pressure gradients. Because, h'' is affected by the thermal boundary conditions, also $\epsilon_{e,r}$, $V_{e,r}$ and $\Psi_{e,r}$ change.

If the constant property and the supercritical fluid cases are compared, it can be seen that, although the production $P_{e,r}$ of the turbulent heat flux are nearly the same for both fluids, the main destruction $\Psi_{e,r}$ substantially differs. For the supercritical fluid cases SC$_{K\to\infty}$ and SC$_{K\to 0}$ the enthalpy–pressure-gradient correlation $\Psi_{e,r}$ is mainly balanced by $P_{e,r}$ and the additional term $E_{e,r}^{(2)}$, which is a source of turbulent heat flux that only appears for the supercritical fluid cases. Unlike for the constant property cases shown in

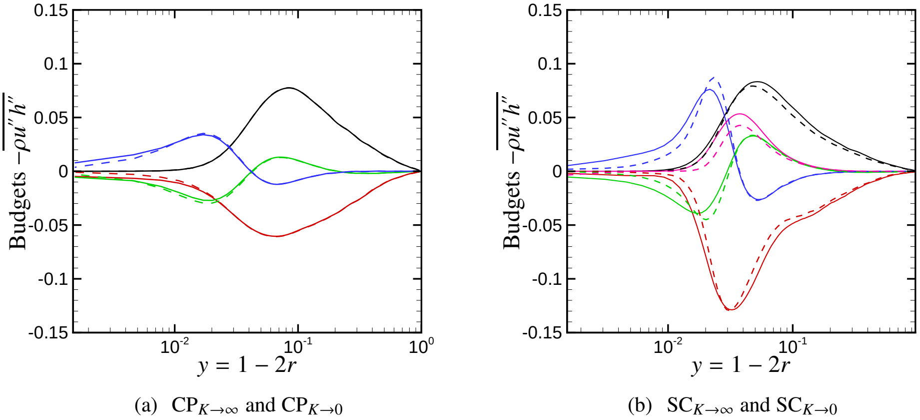

(a) $\text{CP}_{K\to\infty}$ and $\text{CP}_{K\to 0}$

(b) $\text{SC}_{K\to\infty}$ and $\text{SC}_{K\to 0}$

Figure 4.12: Wall-normal turbulent heat flux $-\overline{\rho u''h''}$ budgets at $z = 15$. Solid lines - $\text{SC}_{K\to\infty}$ and $\text{CP}_{K\to\infty}$; dashed lines - $\text{SC}_{K\to 0}$ and $\text{CP}_{K\to 0}$; black - $P_{e,r}$; red - $\Psi_{e,r}$; green - $\epsilon_{e,r}$; blue - $V_{e,r}$; pink - $E_{e,r}$.

figure 4.12(a), the effect of thermal wall boundary conditions on the turbulent heat flux budgets is larger for the variable property cases in figure 4.12(b). Similar to the turbulence kinetic energy budgets, the production for case $\text{SC}_{K\to\infty}$ is larger than for $\text{SC}_{K\to 0}$. The enthalpy–pressure-gradient correlation $\Psi_{e,r}$ shows larger values for $\text{SC}_{K\to\infty}$ than for $\text{SC}_{K\to 0}$ case. The decreased enthalpy–pressure-gradient correlation for $\text{SC}_{K\to 0}$ is mainly because of the decreased enthalpy fluctuation, while the gradient of the pressure fluctuations does not show major differences (not shown here). The additional term $E^{(2)}_{e,r}$, the dissipation $\epsilon_{e,r}$ and the viscous diffusion $V_{e,r}$ show larger values in the near-wall region for case $\text{SC}_{K\to\infty}$, which is due to the higher velocity and enthalpy fluctuations.

4.3.5 FIK identity

In this section we use FIK identity to distinguish the effects of thermal effusivity ratio on skin friction and Nusselt number.

The results of Eq. (3.12) are plotted in figure 4.13 (note, insignificant terms are not shown). In order to verify the FIK derivation, the sum of all terms is compared first with the locally calculated wall shear stress $C_f = 2\tau_{wall}/\left(\rho_b U_b^2\right)$ for $\text{CP}_{K\to\infty}$, $\text{SC}_{K\to\infty}$ and $\text{SC}_{K\to 0}$. An excellent agreement is obtained ensuring correctness and consistency (symbols and line overlap). As expected, for $\text{CP}_{K\to\infty}$ (results for $\text{CP}_{K\to 0}$ are identical and thus not shown) the laminar and turbulent contributions are $3.04 \times 10^{-3} = 16/Re_{b0}$ and 6.23×10^{-3}, respectively. These contributions are identical to the results of a fully developed pipe flow that have also been reported by Fukagata *et al.* (2002).
Unlike for the constant property cases, the inhomogeneous contributions play a significant

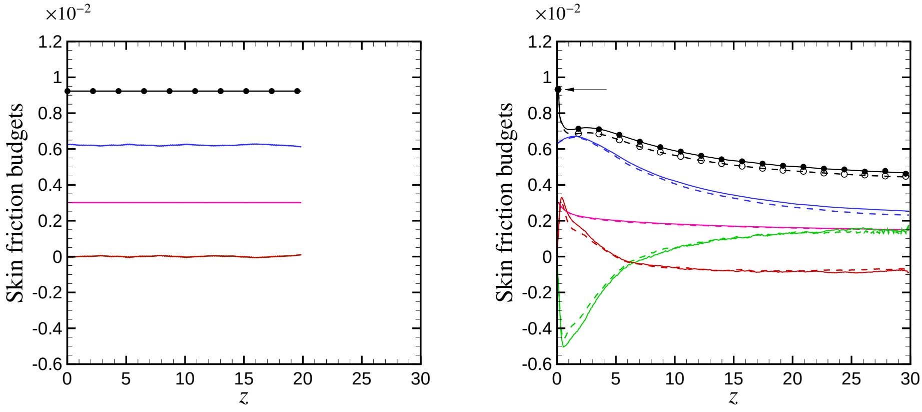

(a) $\mathrm{CP}_{K\to\infty}$ $(\mathrm{CP}_{K\to 0})$ (b) $\mathrm{SC}_{K\to\infty}$ and $\mathrm{SC}_{K\to 0}$

Figure 4.13: Componential contributions to the skin friction. The lines indicate the individual terms as given in Eq. (3.12) and the symbols indicate the locally computed skin friction C_f, (a) (———) $\mathrm{CP}_{K\to\infty}$ $(\mathrm{CP}_{K\to 0})$, (b) solid lines $\mathrm{SC}_{K\to\infty}$ and dashed lines $\mathrm{SC}_{K\to 0}$. Black - $C_{f,FIK}$; pink - C_I; blue - C_{II}; red - C_{IV}; green - C_V.

role for the skin friction in the supercritical cases (see figure 4.13(b)). The term related to the streamwise momentum flux C_V is negative at the inlet and becomes positive at $z \approx 7$. At the beginning of the pipe, the thermal boundary layer is very thin. The density rapidly decreases close to the wall and the mass flux increases. To satisfy the mass flux balance, the velocity in the core region decreases, which also causes a decrease of momentum flux $\overline{\rho}\tilde{u}_z\tilde{u}_z$. Proceeding downstream, the thermal boundary layer grows until a net positive value of C_V is reached at $z \approx 7$. In contrast to C_V, the magnitude of the term C_{IV} (the product of the mean density, mean wall-normal and streamwise velocities) experiences a sharp increase at the inlet region and shows a peak value of 0.33 at $z = 0.7$. Afterwards C_{IV} decreases and reaches a negative value of -0.09 at $z = 17$. This can be explained by the sharp changes of streamwise velocity in the near-wall region, which results in a high positive wall-normal velocity close to the inlet and negative wall-normal velocity further downstream. The contributions of C_I (laminar) and C_{II} (turbulent) to the skin friction show a decreasing trend, due to the reduction in mean viscosity and Reynolds shear stress, respectively.

Figure 4.13(b) shows that the skin friction for $\mathrm{SC}_{K\to\infty}$ is higher along the pipe than for $\mathrm{SC}_{K\to 0}$. Comparing the individual contributions for $\mathrm{SC}_{K\to\infty}$ and $\mathrm{SC}_{K\to 0}$, it can be seen that the turbulent contribution C_{II} shows the largest differences. As explained in section 4.3.3, the lower values of C_{II} for $\mathrm{SC}_{K\to 0}$ are due to the lower Reynolds shear stress, as also shown in figure 4.9(b). In conclusion, the non-fluctuating wall enthalpy boundary condition causes the skin friction for case $\mathrm{SC}_{K\to 0}$ to reduce by approximately 6%.

The comparison of componential contribution to Nusselt number for case $\mathrm{CP}_{K\to\infty}$ and

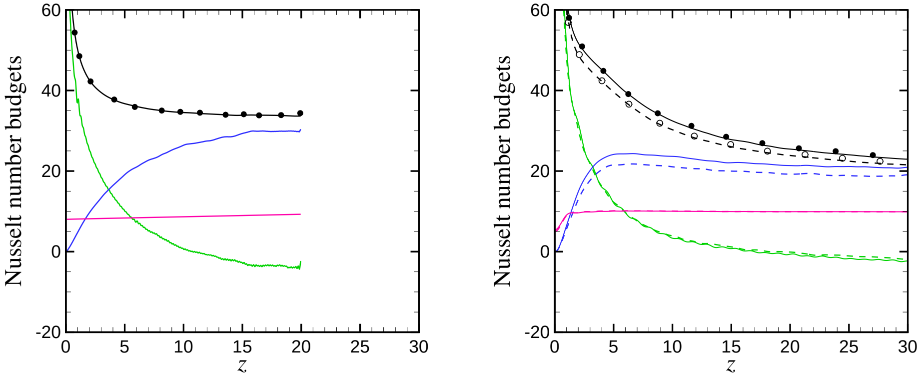

(a) $\text{CP}_{K\to\infty}$ (b) $\text{SC}_{K\to\infty}$ and $\text{SC}_{K\to 0}$

Figure 4.14: Componential contributions to the Nusselt number. The lines indicate the individual terms in Eq. (A.9) and the symbols indicate the locally computed Nusselt number Nu, (a) $\text{CP}_{K\to\infty}$ and (b) solid lines $\text{SC}_{K\to\infty}$, dashed lines $\text{SC}_{K\to 0}$. Black - Nu_{FIK}; pink - H_I; blue - H_{II}; green - H_{III}.

$\text{SC}_{K\to\infty}$ are shown in figure 4.14 (the negligible terms are not shown). As for the skin friction discussed above, the FIK derivation for the Nusselt number is first verified. The sum of all terms is compared with the locally calculated Nusselt number for $\text{CP}_{K\to\infty}$ and $\text{SC}_{K\to\infty}$. An excellent agreement is obtained, ensuring correctness and consistency of the derivation (symbols and line overlap). The most significant contributions to the Nusselt number, in terms of relative magnitude, are attributed to the radial turbulent heat flux H_{II}, the laminar part H_I and the contribution of the mean streamwise enthalpy flux H_{IV}. It is evident that downstream from the inlet, the radial turbulent heat flux H_{II} has the largest contribution to the Nusselt number. The second largest term is the laminar contribution H_I and the term H_{IV} has a positive contribution to Nusselt number at inlet region and it becomes negative further downstream. This is attributed to the growth of the enthalpy profile (thermal boundary layer) and its product with streamwise velocity. Figure 4.14(b) also shows the influence of different thermal boundary conditions on the componential contributions to the Nusselt number for case $\text{SC}_{K\to\infty}$ and $\text{SC}_{K\to 0}$. It is evident that the boundary condition solely affects the turbulent radial heat flux H_{II}, thus causing the Nusselt number to reduce for the non-fluctuating wall enthalpy case $\text{SC}_{K\to 0}$ by approximately 7%.

4.4 Conclusion

In this chapter we used DNS to investigate the effect of thermal wall boundary conditions on developing turbulent pipe flows with CO_2 at a thermodynamic supercritical pressure

of P_0 = 80 bar. The Reynolds number based on pipe diameter and inlet friction velocity is $Re_{\tau 0} = 360$ and the inlet Prandtl number is $Pr_0 = 3.19$. Two different wall boundary conditions are studied, namely a case with fluctuating ($\mathrm{SC}_{K\to\infty}$) and non-fluctuating ($\mathrm{SC}_{K\to 0}$) wall enthalpy. The boundary conditions correspond to the upper and lower limit of thermal effusivity ratio K, respectively. To incorporate both thermal wall boundary conditions, first, a simulation with a constant heat flux boundary condition ($\mathrm{SC}_{K\to\infty}$) is performed. Then, for the other simulation, the mean wall enthalpy obtained from the first simulation is used as the thermal wall boundary condition ($\mathrm{SC}_{K\to 0}$).
To compare the effects of different thermal boundary conditions on heat transfer to supercritical fluid cases, we also performed DNS with constant property fluids that have the same Reynolds number and Prandtl number as the supercritical fluid cases at the inlet of the pipe. The results show that the wall temperature fluctuations at the wall have very limited effect on the mean enthalpy and Nusselt number for constant property cases. This result is in agreement with existing literature, where it was shown that the Nusselt number is independent of the thermal boundary condition if $Pr \geq 1$.
In contrast to the constant property cases, the heat transfer to supercritical fluids with $Pr \geq 1$ strongly depends on the thermal wall boundary condition. A significant increase in Nusselt number and bulk enthalpy is observed if thermal fluctuations are allowed at the wall. We found that the wall enthalpy fluctuations cause strong fluctuations in density, viscosity and thermal conductivity, which consequently promote mass and velocity fluctuations that increase turbulent shear stress and turbulent heat flux. A quadrant analysis and FIK identities for both quantities confirms this result, which shows that the turbulent shear stress and turbulent heat flux are attenuated for the non-fluctuating wall temperature case. The present work provides clear evidence that thermal effusivity ratio has a large impact on Nusselt number and skin friction for fluids with large property variations.

5

Conclusions and future directions

In the final chapter of this thesis, the overall results from this research are summarised and conclusions are drawn regarding the contribution of this thesis to the subsequent development in this field of research. Recommendations based on the results presented in this thesis will be given for the direction of future research.

5.1 Conclusions

The simulations performed in the course of the research work were aimed at developing a better understanding of turbulent heat transfer in flows at supercritical pressures. Previous turbulence models have largely failed in this regard due to their inability in capturing the highly non-linear nature of the physical phenomena encountered under these conditions. Also experiments have a limitations, since very detailed visualisations of the flow are very difficult to obtain for flows in supercritical conditions. Utilising high-performance computing resources in order to carry out fully resolved numerical simulations of the Navier-Stokes equations of flows at supercritical pressures can provide more detailed insights. The aim of this thesis was therefore to use DNS to study the effects of strong thermophysical property variations on turbulent heat transfer at supercritical pressures.

To this end, an in-house DNS program was developed to solve the low-Mach number approximation of the Navier-Stokes equations in cylindrical coordinates in a spatially developing pipe flows with CO_2 as working fluid at a thermodynamic pressure of P_0= 80 bar (P_{cr} = 73.77 bar). The Reynolds number based on the pipe diameter and friction velocity at the pipe inlet was $Re_{\tau 0} = 360$ and the inlet Prandtl number was $Pr_0 = 3.19$. To incorporate large variations in thermophysical properties within the pipe flow, a constant wall heat flux is applied such that the pseudo-critical temperature occurs close to the pipe wall. To have realistic turbulent inlet boundary conditions, a separate simulation of a periodic isothermal pipe was run to generate a library of turbulence data.

The core results of this thesis consist of two main parts, (1) the effect of large thermophysical property variations and buoyancy on the mean flow was studied (chapter 3) and (2) the effect of different thermal wall boundary conditions was investigated on turbulent heat transfer to supercritical fluids (chapter 4). The overall results of each part are summarised below.

Turbulent statistics, such as turbulent shear stress, radial turbulent heat flux, turbulent kinetic energy and its shear and buoyant production rates for flows with forced and mixed convection in upward and downward flows have been reported. The results showed that, in the case of forced convection the flow acceleration due to thermal expansion causes a reduction in turbulent kinetic energy (deteriorating turbulence), which causes the pipe wall temperature to increase in the downstream direction. Similar results were observed for upward mixed convection cases with small buoyancy, but with a higher reduction in turbulence and hence a further increase in wall temperature. Flow acceleration effects in the pipe flow are magnified due to the fact that the influence of buoyancy and thermal expansion, which causes these effects, both act in the direction of the flow and thereby reinforce each other. Increasing the buoyancy effects in upward flows to moderate values, the turbulence deterioration is followed by a recovery of turbulence towards the end of the pipe. The wall temperature shows an increase, which is higher than for the forced convection case in the deterioration region, whereas in the recovery region the wall temperature is lower than in the forced convection case. In the deterioration region, the Reynolds shear stress decreases (becoming negative) at locations slightly away from the wall. Recovery starts after the Reynolds shear stress is negative in most of the radial domain (except close to the wall). In the case of very high buoyancy in upward flows the heat transfer deterioration is followed by a recovery of turbulence. The deformation of the Reynolds shear stress profile to negative values starts much earlier as compared to moderate buoyancy cases and reaches values that are larger than the inlet. The role of structural and external effects of buoyancy on the heat transfer recovery is more pronounced than in cases with moderate buoyancy. For mixed downward convection with moderate buoyancy, the flow experiences an enhancement of heat transfer along the entire pipe, except for a small region near the inlet. In contrary to upward flows, buoyancy is in opposite direction to the flow and induces deceleration in the near-wall region and acceleration at core region. The buoyancy production (structural effect) in this case is always positive, which favours the turbulent kinetic energy.

We furthermore highlighted that higher order correlations with thermophysical properties (density, thermal conductivity and viscosity) contribute up to 31% of the total heat flux. This has been investigated by decomposing the wall heat flux into contributions from turbulent, molecular and correlations that involve the fluctuations of thermophysical properties. A smaller effect of property fluctuations on the mean momentum was observed. However, they might play a large role in the energy budgets of the Reynolds stresses.

We also derived two identities for the skin friction coefficient and the Nusselt number from the streamwise momentum and energy equations, respectively. Using these identities, we were able to investigate the componential contributions to skin friction coefficient and Nusselt number.

Another important finding of this work is that averaging highly non-linear functions of thermophysical properties leads to the Jensen inequality, which results in large deviations between $\overline{c_p}$ and $c_p(\tilde{h})$. The analysis of DNS data showed that this deviation has a direct relation with the enthalpy fluctuation; i.e. the higher the enthalpy fluctuations the larger difference between $\overline{c_p}$ and $c_p(\tilde{h})$.

To examine the effect of bulk viscosity μ_b on heated turbulent flow at supercritical pressures, a DNS of a forced convection case was performed by considering the temperature-dependent bulk viscosity. No significant differences compared to the case without $\mu_b = 0$ were observed.

The second part of this work was devoted to investigating the effect of thermal wall boundary conditions on the heat transfer rate. Two different wall boundary conditions were studied, namely a case with fluctuating and non-fluctuating wall enthalpy, which correspond to the upper and lower limit of thermal effusivity ratio K, respectively. To incorporate both thermal wall boundary conditions, first, a simulation with a constant heat flux boundary condition is performed. Then, for the other simulation, the mean wall enthalpy obtained from the first simulation is used as the thermal wall boundary condition. To compare the effects of different thermal boundary conditions on heat transfer to supercritical fluid cases, we also performed a DNS with a constant property fluid that has the same Reynolds number and Prandtl number as the supercritical fluid cases at the inlet of the pipe.

The results for constant property cases showed that differences in wall temperature fluctuations at the wall have very limited effects on the mean enthalpy and the Nusselt number for constant property cases. This finding is in agreement with existing literature, where it was shown that the Nusselt number is independent of the thermal boundary condition if $Pr \geq 1$. Unlike for the constant property cases, the heat transfer to supercritical fluids with $Pr \geq 1$ strongly depends on the thermal wall boundary condition. A significant increase in the Nusselt number and bulk enthalpy was observed when the thermal fluctuations are allowed at the wall. We found that large enthalpy fluctuations at- and close to the wall cause strong fluctuations in density, viscosity and thermal conductivity, and consequently promote mass and velocity fluctuations that increase turbulent shear stress and turbulent heat flux. These results are further confirmed using quadrant analysis and FIK identities, where they showed that the turbulent shear stress and turbulent heat flux are attenuated for the non-fluctuating wall temperature (isothermal wall) case.

5.2 Recommendations for future work

Based on the results obtained in this thesis, several further questions can be addressed, which are summarized in the following list:

- **Turbulence modelling.** Why turbulence models fail to predict the heat transfer to supercritical fluids?
- **Cooling under supercritical conditions.** What will be the effects of heat rejection (cooling) on turbulence statistics at supercritical pressures? Will the effects be the opposite of heating?
- **Bulk viscosity.** What will be the effects of bulk viscosity on turbulent heat transfer at pressures closer to the critical point?
- **Conjugate heat transfer.** How turbulence statistics will respond to changes in wall thickness and thermal effusivity ratios?

In the following a list of recommendations to answer these questions.

Current turbulence models are incapable to reliably predict heat transfer to supercritical fluids. Several effects will have to be taken into account if new models are to be developed. These are: large property fluctuations and their correlation with momentum and temperature, Jensen inequality and turbulent Prandtl number in case of upward flows with large buoyancy forces.

Throughout this thesis, the process of heat addition to turbulent flows at supercritical pressures has been investigated. However, the heat rejection is of the same importance from the application point of view. Therefore, a recommendation can be the simulations of turbulent heat transfer, where the flow at temperatures higher that pseudo-critical temperature enters the pipe with wall temperature lower pseudo-critical temperature.

A recommendation is to perform a study on the effects of bulk viscosity on turbulent flows at pressures near the critical point, say P_0 =76-79 bar for CO_2, where the magnitude and variation of bulk viscosity become significant.

One of the significant findings in this thesis is the effect of thermal wall boundary conditions (thermal effusivity ratio K) on turbulence and heat transfer. Two boundary conditions correspond to the upper and lower limit of thermal effusivity ratio ($K \rightarrow \infty$ and $K \rightarrow 0$) were investigated. This research can be elaborated by considering the conjugate heat transfer problem by specifying the thickness and property of the solid wall. Nonetheless, intermediate thermal effusivity ratios can be examined. Therefore, the recommendation is to develop an in-house code to simultaneously solve the flow domain and the unsteady heat conduction inside the solid walls and study different thermal effusivity ratios.

A

Derivation of the FIK identity

Here, we show how the FIK identity for the skin friction coefficient and the Nusselt number in spatially developing pipe flows can be derived. We use a similar mathematical methodology for derivation of the skin friction coefficient in a fully developed pipe flow derived by Fukagata *et al.* (2002). To derive the FIK identity for the skin friction coefficient we start from the mean streamwise momentum equation

$$\begin{aligned}&\frac{1}{r}\frac{\partial r\overline{\rho}\tilde{u}_r\tilde{u}_z}{\partial r}+\frac{1}{r}\frac{\partial r\overline{\rho u_r''u_z''}}{\partial r}+\frac{\partial\overline{\rho}\tilde{u}_z\tilde{u}_z}{\partial z}+\frac{\partial\overline{\rho u_z''u_z''}}{\partial z}+\frac{\partial\overline{p}}{\partial z}\\&\quad-\frac{1}{Re_{\tau 0}}\left(\frac{1}{r}\frac{\partial r\overline{\mu}\overline{S}_{rz}}{\partial r}+\frac{1}{r}\frac{\partial r\overline{\mu' S'_{rz}}}{\partial r}+\frac{\partial\overline{\mu}\overline{S}_{zz}}{\partial z}+\frac{\partial\overline{\mu' S'_{zz}}}{\partial z}\right)\pm Ri_{0z}\overline{\rho}=0.\end{aligned}\tag{A.1}$$

The integration of Eq. (A.1) over r gives the relation between the local wall shear stress τ_w and bulk quantities, i.e.,

$$\begin{aligned}&\frac{2}{R^2}\int_0^R\left(\frac{\partial\overline{\rho}\tilde{u}_z\tilde{u}_z}{\partial z}\right)rdr+\frac{2}{R^2}\int_0^R\left(\frac{\partial\overline{\rho u_z''u_z''}}{\partial z}\right)rdr+\frac{2}{R^2}\int_0^R\frac{\partial\overline{p}}{\partial z}rdr\\&\quad-\frac{2\tau_w}{R}-\frac{2}{R^2}\int_0^R\left(\frac{1}{Re_{\tau 0}}\frac{\partial\overline{\mu}\overline{S}_{zz}}{\partial z}+\frac{1}{Re_{\tau 0}}\frac{\partial\overline{\mu' S'_{zz}}}{\partial z}\right)rdr\pm\frac{2}{R^2}\int_0^R Ri_{0z}\overline{\rho}rdr=0.\end{aligned}\tag{A.2}$$

Next, we subtract Eq. (A.2) from Eq. (A.1),

$$\begin{aligned}&\frac{1}{r}\frac{\partial r\overline{\rho}\tilde{u}_r\tilde{u}_z}{\partial r}+\frac{1}{r}\frac{\partial r\overline{\rho u_r''u_z''}}{\partial r}+\frac{\partial\overline{\rho}\tilde{u}_z\tilde{u}_z}{\partial z}-\frac{2}{R^2}\int_0^R\left(\frac{\partial\overline{\rho}\tilde{u}_z\tilde{u}_z}{\partial z}\right)rdr\\&+\frac{\partial\overline{\rho u_z''u_z''}}{\partial z}-\frac{2}{R^2}\int_0^R\left(\frac{\partial\overline{\rho u_z''u_z''}}{\partial z}\right)rdr+\frac{\partial\overline{p}}{\partial z}-\frac{2}{R^2}\int_0^R\frac{\partial\overline{p}}{\partial z}rdr\\&-\frac{1}{Re_{\tau 0}}\left(\frac{1}{r}\frac{\partial r\overline{\mu}\overline{S}_{rz}}{\partial r}\right)-\frac{1}{Re_{\tau 0}}\left(\frac{1}{r}\frac{\partial r\overline{\mu' S'_{rz}}}{\partial r}\right)+\frac{2\tau_w}{R}\\&-\frac{1}{Re_{\tau 0}}\left(\frac{\partial\overline{\mu}\overline{S}_{zz}}{\partial z}-\frac{2}{R^2}\int_0^R\left(\frac{\partial\overline{\mu}\overline{S}_{zz}}{\partial z}\right)rdr\right)\\&-\frac{1}{Re_{\tau 0}}\left(\frac{\partial\overline{\mu' S'_{zz}}}{\partial z}-\frac{2}{R^2}\int_0^R\left(\frac{\partial\overline{\mu' S'_{zz}}}{\partial z}\right)rdr\right)\pm Ri_{0z}\left(\overline{\rho}-\frac{2}{R^2}\int_0^R\overline{\rho}rdr\right)=0.\end{aligned}\tag{A.3}$$

The relation for componential contributions to the local skin friction coefficient can be obtained by applying double integration, i.e., $\int_0^R rdr \int_0^r rdr$ to Eq. (A.3) as

$$
\begin{aligned}
C_{f,FIK} = &-\frac{2}{\rho_b U_b^2 Re_{\tau 0}} \int_0^R r\overline{\mu}\overline{S}_{rz} rdr + \frac{2}{\rho_b U_b^2} \int_0^R r\overline{\rho u_r'' u_z''} rdr \\
&+ \frac{1}{\rho_b U_b^2} \int_0^R (R^2 - r^2) \left\langle \frac{\partial \overline{p}}{\partial z} \right\rangle rdr + \frac{1}{\rho_b U_b^2} \int_0^R r\overline{\rho}\tilde{u}_r\tilde{u}_z rdr \\
&+ \frac{1}{\rho_b U_b^2} \int_0^R (R^2 - r^2) \left\langle \frac{\partial \overline{\rho}\tilde{u}_z\tilde{u}_z}{\partial z} \right\rangle rdr + \frac{1}{\rho_b U_b^2} \int_0^R (R^2 - r^2) \left\langle \frac{\partial \overline{\rho u_z'' u_z''}}{\partial z} \right\rangle rdr \\
&- \frac{1}{\rho_b U_b^2 Re_{\tau 0}} \int_0^R (R^2 - r^2) \left\langle \frac{1}{r} \frac{\partial r\overline{\mu' S'}_{rz}}{\partial r} \right\rangle rdr - \frac{1}{\rho_b U_b^2 Re_{\tau 0}} \int_0^R (R^2 - r^2) \left\langle \frac{\partial \overline{\mu}\overline{S}_{zz}}{\partial z} \right\rangle rdr \\
&- \frac{1}{\rho_b U_b^2 Re_{\tau 0}} \int_0^R (R^2 - r^2) \left\langle \frac{\partial \overline{\mu' S'}_{zz}}{\partial z} \right\rangle rdr \pm \frac{Ri_{0z}}{\rho_b U_b^2} \int_0^R (R^2 - r^2) \left\langle \overline{\rho} \right\rangle rdr,
\end{aligned}
\tag{A.4}
$$

where $C_{f,FIK} = 2\tau_w/\rho_b U_b^2$ and $\langle\ \rangle$ indicates the following operation

$$
\langle \Phi(r,z) \rangle = \Phi(r,z) - \frac{2}{R^2} \int_0^R \Phi(r,z) rdr. \tag{A.5}
$$

The same procedure can also be applied to decompose the Nusselt number Nu_{FIK}. In order to derive the FIK identity for the Nusselt number we start from the mean energy equation

$$
\begin{aligned}
&\frac{1}{r}\frac{\partial r\overline{\rho}\tilde{u}_r\tilde{h}}{\partial r} + \frac{1}{r}\frac{\partial r\overline{\rho u_r'' h''}}{\partial r} + \frac{\partial \overline{\rho}\tilde{u}_z\tilde{h}}{\partial z} + \frac{\partial \overline{\rho u_z'' h''}}{\partial z} \\
&- \frac{1}{Re_{\tau 0} Pr_0} \left(\frac{1}{r}\frac{\partial}{\partial r}\left(r\overline{\alpha}\frac{\partial \overline{h}}{\partial r} \right) + \frac{1}{r}\frac{\partial}{\partial r}\left(r\overline{\alpha' \frac{\partial h'}{\partial r}} \right) + \frac{\partial}{\partial z}\left(\overline{\alpha}\frac{\partial \overline{h}}{\partial z} \right) + \frac{\partial}{\partial z}\left(r\overline{\alpha' \frac{\partial h'}{\partial z}} \right) \right) = 0.
\end{aligned}
\tag{A.6}
$$

The integration of Eq. (A.6) over r gives the relation between the local wall heat flux Q and bulk quantities as follows,

$$\frac{2}{R^2}\int_0^R\left(\frac{\partial\bar{\rho}\tilde{u}_z\tilde{h}}{\partial z}\right)rdr+\frac{2}{R^2}\int_0^R\left(\frac{\partial\overline{\rho u_z''h''}}{\partial z}\right)rdr+\frac{2Q}{R}$$
$$-\frac{2}{R^2}\int_0^R\left(\frac{1}{Re_{\tau 0}Pr_0}\frac{\partial}{\partial z}\left(\bar{\alpha}\frac{\partial\bar{h}}{\partial z}\right)+\frac{1}{Re_{\tau 0}Pr_0}\frac{\partial}{\partial z}\left(\overline{\alpha'\frac{\partial h'}{\partial z}}\right)\right)rdr=0. \tag{A.7}$$

Next, we subtract Eq. (A.7) from Eq. (A.6),

$$\frac{1}{r}\frac{\partial r\bar{\rho}\tilde{u}_r\tilde{h}}{\partial r}+\frac{1}{r}\frac{\partial r\overline{\rho u_r''h''}}{\partial r}+\frac{\partial\bar{\rho}\tilde{u}_z\tilde{h}}{\partial z}-\frac{2}{R^2}\int_0^R\left(\frac{\partial\bar{\rho}\tilde{u}_z\tilde{h}}{\partial z}\right)rdr$$
$$+\frac{\partial\overline{\rho u_z''h''}}{\partial z}-\frac{2}{R^2}\int_0^R\left(\frac{\partial\overline{\rho u_z''h''}}{\partial z}\right)rdr$$
$$-\frac{1}{Re_{\tau 0}Pr_0}\frac{1}{r}\frac{\partial}{\partial r}\left(r\bar{\alpha}\frac{\partial\bar{h}}{\partial r}\right)-\frac{1}{Re_{\tau 0}Pr_0}\frac{1}{r}\frac{\partial}{\partial r}\left(r\overline{\alpha'\frac{\partial h'}{\partial r}}\right)-\frac{2Q}{R}$$
$$-\frac{1}{Re_{\tau 0}Pr_0}\left(\frac{\partial}{\partial z}\left(\bar{\alpha}\frac{\partial\bar{h}}{\partial z}\right)-\frac{2}{R^2}\int_0^R\frac{\partial}{\partial z}\left(\bar{\alpha}\frac{\partial\bar{h}}{\partial z}\right)rdr\right)$$
$$-\frac{1}{Re_{\tau 0}Pr_0}\left(\frac{\partial}{\partial z}\left(\overline{\alpha'\frac{\partial h'}{\partial z}}\right)-\frac{2}{R^2}\int_0^R\frac{\partial}{\partial z}\left(\overline{\alpha'\frac{\partial h'}{\partial z}}\right)rdr\right)=0. \tag{A.8}$$

By applying double integration to Eq. (A.8) the relation for componential contributions to the local Nusselt number is obtained as

$$\begin{aligned}
Nu_{FIK} = {} & \frac{32}{\alpha_b(\overline{h}_{wall} - h_b)} \int_0^R r\overline{\alpha}\frac{\partial \overline{h}}{\partial r} rdr - \frac{32Re_{\tau 0}Pr_0}{\alpha_b(\overline{h}_{wall} - h_b)} \int_0^R r\overline{\rho u_r'' h''} rdr \\
& - \frac{16Re_{\tau 0}Pr_0}{\alpha_b(\overline{h}_{wall} - h_b)} \int_0^R (R^2 - r^2) \left\langle \frac{1}{r}\frac{\partial r\overline{\rho}\tilde{u}_r\tilde{h}}{\partial r} \right\rangle rdr \\
& - \frac{16Re_{\tau 0}Pr_0}{\alpha_b(\overline{h}_{wall} - h_b)} \int_0^R (R^2 - r^2) \left\langle \frac{\partial \overline{\rho}\tilde{u}_z\tilde{h}}{\partial z} \right\rangle rdr \\
& - \frac{16Re_{\tau 0}Pr_0}{\alpha_b(\overline{h}_{wall} - h_b)} \int_0^R (R^2 - r^2) \left\langle \frac{\partial \overline{\rho u_z'' h''}}{\partial z} \right\rangle rdr \\
& + \frac{16}{\alpha_b(\overline{h}_{wall} - h_b)} \int_0^R (R^2 - r^2) \left\langle \frac{1}{r}\frac{\partial r}{\partial r}\overline{\alpha'\frac{\partial h'}{\partial r}} \right\rangle rdr \\
& + \frac{16}{\alpha_b(\overline{h}_{wall} - h_b)} \int_0^R (R^2 - r^2) \left\langle \frac{\partial}{\partial z}(\overline{\alpha}\frac{\partial \overline{h}}{\partial z}) \right\rangle rdr \\
& + \frac{16}{\alpha_b(\overline{h}_{wall} - h_b)} \int_0^R (R^2 - r^2) \left\langle \frac{\partial}{\partial z}(\overline{\alpha'\frac{\partial h'}{\partial z}}) \right\rangle rdr,
\end{aligned} \tag{A.9}$$

where $Nu_{FIK} = Q/\left(\alpha_b(\overline{h}_{wall} - h_b)\right)$.

References

ABE, K., KONDOH, T. & NAGANO, Y. 1994 A new turbulence model for predicting fluid flow and heat transfer in separating and reattaching flows-I. Flow field calculations. *International Journal of Heat and Mass Transfer* **37** (1), 139–151.

ACKERMAN, J. 1970 Pseudoboiling heat transfer to supercritical pressure water in smooth and ribbed tubes. *Journal of Heat Transfer* **92**, 490.

AKSELVOLL, K. & MOIN, P. 1995 Large eddy simulation of turbulent confined coannular jets and turbulent flow over a backward facing step.

ALEXANDER, L. V., ALLEN, S. K., BINDOFF, N. L., BREON, F.-M., CHURCH, J. A., CUBASCH, U., EMORI, S., FORSTER, P., FRIEDLINGSTEIN, P., GILLETT, N. *et al.* 2013 Summary for policymakers.

ANTONIA, R., TEITEL, M., KIM, J. & BROWNE, L. 1992 Low-Reynolds-number effects in a fully developed turbulent channel flow. *Journal of Fluid mechanics* **236**, 579–605.

BAE, J. H., YOO, J. Y. & CHOI, H. 2005 Direct numerical simulation of turbulent supercritical flows with heat transfer. *Physics of Fluids* **17**, 105104.

BAE, J. H., YOO, J. Y., CHOI, H. & MCELIGOT, D. M. 2006 Effects of large density variation on strongly heated internal air flows. *Physics of Fluids* **18** (7), 75102–75102.

BAE, J. H., YOO, J. Y. & MCELIGOT, D. M. 2008 Direct numerical simulation of heated CO_2 flows at supercritical pressure in a vertical annulus at Re= 8900. *Physics of Fluids* **20**, 055108.

BAE, Y. Y. & KIM, H. Y. 2009 Convective heat transfer to CO_2 at a supercritical pressure flowing vertically upward in tubes and an annular channel. *Experimental Thermal and Fluid Science* **33** (2), 329–339.

BAE, Y. Y., KIM, H. Y. & KANG, D. J. 2010 Forced and mixed convection heat transfer to supercritical CO_2 vertically flowing in a uniformly-heated circular tube. *Experimental Thermal and Fluid Science* **34** (8), 1295–1308.

BEHNIA, M., PARNEIX, S. & DURBIN, P. A. 1998 Prediction of heat transfer in an axisymmetric turbulent jet impinging on a flat plate. *International Journal of Heat and Mass Transfer* **41** (12), 1845–1855.

Bergman, T. L., Incropera, F. P., Lavine, A. S. & DeWitt, D. P. 2011 *Fundamentals of heat and mass transfer*. John Wiley & Sons.

Birken, P. & Meister, A. 2005 Stability of preconditioned finite volume schemes at low mach numbers. *BIT Numerical Mathematics* **45** (3), 463–480.

Bishop, A., Sandberg, R. & Tong, L. 1964 Forced-convection heat transfer to water at near-critical temperatures and supercritical pressures. *Tech. Rep.*. Westinghouse Electric Corp., Pittsburgh, Pa. Atomic Power Div.

Bradshaw, P. 1977 Compressible turbulent shear layers. *Annual Review of Fluid Mechanics* **9** (1), 33–52.

British Petroleum (BP) 2014 Statistical review of world energy June 2014 .

Canuto, V. 1997 Compressible turbulence. *The Astrophysical Journal* **482** (2), 827.

Carr, A., Connor, M. & Buhr, H. 1973 Velocity, temperature, and turbulence measurements in air for pipe flow with combined free and forced convection. *Journal of Heat Transfer* **95**, 445.

Carslaw, H. S. & Jaeger, J. C. 1959 *Conduction of heat in solids*. Oxford: Clarendon Press.

Chen, H., Goswami, D. Y. & Stefanakos, E. K. 2010 A review of thermodynamic cycles and working fluids for the conversion of low-grade heat. *Renewable and sustainable energy reviews* **14** (9), 3059–3067.

Chen, Y. 2006 Novel cycles using carbon dioxide as working fluid: new ways to utilize energy from low-grade heat sources. KTH.

Chen, Y., Lundqvist, P., Johansson, A. & Platell, P. 2006 A comparative study of the carbon dioxide transcritical power cycle compared with an organic Rankine cycle with r123 as working fluid in waste heat recovery. *Applied Thermal Engineering* **26** (17), 2142–2147.

Chikitkin, A., Rogov, B., Tirsky, G. & Utyuzhnikov, S. 2015 Effect of bulk viscosity in supersonic flow past spacecraft. *Applied Numerical Mathematics* **93**, 47–60.

Cook, A. W. & Riley, J. J. 1996 Direct numerical simulation of a turbulent reactive plume on a parallel computer. *Journal of Computational Physics* **129** (2), 263–283.

Cramer, S. & Bahmani, F. 2014 Effect of large bulk viscosity on large-Reynolds-number flows. *Journal of Fluid Mechanics* **751**, 142–163.

Das, S. B., Joughin, I., Behn, M. D., Howat, I. M., King, M. A., Lizarralde, D. & Bhatia, M. P. 2008 Fracture propagation to the base of the greenland ice sheet during supraglacial lake drainage. *Science* **320** (5877), 778–781.

Duan, L., Beekman, I. & Martin, M. 2010 Direct numerical simulation of hypersonic turbulent boundary layers. part 2. effect of wall temperature. *Journal of Fluid Mechanics* **655**, 419–445.

Duffey, R. B. & Pioro, I. L. 2005 Experimental heat transfer of supercritical carbon dioxide flowing inside channels (survey). *Nuclear Engineering and Design* **235** (8), 913–924.

Fenghour, A., Wakeham, W. A. & Vesovic, V. 1998 The viscosity of carbon dioxide. *Journal of Physical and Chemical Reference Data* **27** (1), 31–44.

Fewster, J. 1976 Mixed forced and free convective heat transfer to supercritical pressure fluids flowing in vertical pipes. PhD thesis, The University of Manchester.

Fukagata, K., Iwamoto, K. & Kasagi, N. 2002 Contribution of Reynolds stress distribution to the skin friction in wall-bounded flows. *Physics of Fluids (1994-present)* **14** (11), L73–L76.

Fukagata, K., Iwamoto, K. & Kasagi, N. 2005 Novel turbulence control strategy for simultaneously achieving friction drag reduction and heat transfer augmentation. In *Proceedings of the 4th International Symposium Turbulence and Shear Flow Phenomena, Williamsburg, VA, June*, pp. 27–29.

Fukagata, K. & Kasagi, N. 2003 Drag reduction in turbulent pipe flow with feedback control applied partially to wall. *International journal of heat and fluid flow* **24** (4), 480–490.

Gomez, T., Flutet, V. & Sagaut, P. 2009 Contribution of Reynolds stress distribution to the skin friction in compressible turbulent channel flows. *Physical Review E* **79** (3), 035301.

Govindarajan, R. & Sahu, K. C. 2014 Instabilities in viscosity-stratified flow. *Annual Review of Fluid Mechanics* **46**, 331–353.

Hall, W. B. 1971 Heat transfer near the critical point. *Advances in Heat Transfer* **7** (1), 86.

Hall, W. B. & Jackson, J. D. 1969 Laminarization of a turbulent pipe flow by buoyancy forces. In *ASME*.

Hall, W. B., Jackson, J. D. & Watson, A. 1968 A. review of forced convection heat transfer to fluids at super-critical pressures. *Heat Transfer and Fluid Dynamics of Near Critical Fluids. Proc. Inst. Mech. Eng* **182**.

Hansen, J., Nazarenko, L., Ruedy, R., Sato, M., Willis, J., Del Genio, A., Koch, D., Lacis, A., Lo, K., Menon, S. *et al.* 2005 Earth's energy imbalance: Confirmation and implications. *science* **308** (5727), 1431–1435.

Hasan, N. & Farouk, B. 2012 Buoyancy driven convection in near-critical and supercritical fluids. *International Journal of Heat and Mass Transfer* **55** (15), 4207–4216.

He, S., Jiang, P. X., Xu, Y. J., Shi, R. F., Kim, W. & Jackson, J. D. 2005 A computational study of convection heat transfer to CO_2 at supercritical pressures in a vertical mini tube. *International Journal of Thermal Sciences* **44** (6), 521–530.

He, S., Kim, W. S. & Bae, J. H. 2008*a* Assessment of performance of turbulence models in predicting supercritical pressure heat transfer in a vertical tube. *International Journal of Heat and Mass Transfer* **51** (19), 4659–4675.

He, S., Kim, W. S. & Jackson, J. D. 2008*b* A computational study of convective heat transfer to carbon dioxide at a pressure just above the critical value. *Applied Thermal Engineering* **28** (13), 1662–1675.

Hetsroni, G. & Rozenblit, R. 1994 Heat transfer to a liquid-solid mixture in a flume. *International Journal of Multiphase Flow* **20** (4), 671–689.

Houghton, J. T., Ding, Y., Griggs, D. J., Noguer, M., van der Linden, P. J., Dai, X., Maskell, K. & Johnson, C. 2001 Climate change 2001: the scientific basis. The Press Syndicate of the University of Cambridge.

Huang, P. G., Coleman, G. N. & Bradshaw, P. 1995 Compressible turbulent channel flows: DNS results and modelling. *Journal of Fluid Mechanics* **305** (1), 185–218.

Hung, T.-C. 2001 Waste heat recovery of organic Rankine cycle using dry fluids. *Energy Conversion and Management* **42** (5), 539–553.

Hung, T.-C., Shai, T. & Wang, S. 1997 A review of organic Rankine cycles (ORCs) for the recovery of low-grade waste heat. *Energy* **22** (7), 661–667.

Iritani, Y., Kasagi, N. & Hirata, M. 1985 Heat transfer mechanism and associated turbulence structure in the near-wall region of a turbulent boundary layer. In *Turbulent Shear Flows 4*, pp. 223–234. Springer.

Jackson, J., Lutterodt, E. & Weinberg, R. 2003 Experimental studies of buoyancy-influenced convective heat transfer in heated vertical tubes at pressures just above and just below the thermodynamic critical value. In *Proceedings of the Joint International Conference on Global Environment and Nuclear Energy System/Advanced Power Plants*, pp. 15–19.

Jackson, J. D. & Hall, W. B. 1979*a* Forced convection heat transfer to fluids at supercritical pressure. *Turbulent Forced Convection in Channels and Bundles* **2**, 563–611.

Jackson, J. D. & Hall, W. B. 1979*b* Influences of buoyancy on heat transfer to fluids flowing in vertical tubes under turbulent conditions. *Turbulent Forced Convection in Channels and Bundles* **2**, 613–640.

Jensen, J. L. W. V. 1906 Sur les fonctions convexes et les inégalités entre les valeurs moyennes. *Acta Mathematica* **30** (1), 175–193.

Jiang, P.-X., Xu, Y.-J., Lv, J., Shi, R.-F., He, S. & Jackson, J. 2004 Experimental investigation of convection heat transfer of CO_2 at super-critical pressures in vertical mini-tubes and in porous media. *Applied Thermal Engineering* **24** (8), 1255–1270.

Jiang, P. X., Zhang, Y. & Shi, R. F. 2008 Experimental and numerical investigation of convection heat transfer of CO_2 at supercritical pressures in a vertical mini-tube. *International Journal of Heat and Mass Transfer* **51** (11), 3052–3056.

Joughin, I., Das, S. B., King, M. A., Smith, B. E., Howat, I. M. & Moon, T. 2008 Seasonal speedup along the western flank of the Greenland Ice Sheet. *Science* **320** (5877), 781–783.

Kametani, Y. & Fukagata, K. 2011 Direct numerical simulation of spatially developing turbulent boundary layers with uniform blowing or suction. *Journal of Fluid Mechanics* **681**, 154–172.

Kasagi, N., Kuroda, A. & Hirata, M. 1989 Numerical investigation of near-wall turbulent heat transfer taking into account the unsteady heat conduction in the solid wall. *Journal of Heat Transfer* **111** (2), 385–392.

Kays, W. M. & Crawford, M. E. 1993 *Convective Heat and Mass Transfert*. McGraw-Hill.

Kim, H., Bae, Y. Y., Kim, H. Y., Song, J. H. & Cho, B. H. 2006 Experimental investigation on the heat transfer characteristics in a vertical upward flow of supercritical CO_2. *Tech. Rep.*. American Nuclear Society, 555 North Kensington Avenue, La Grange Park, IL 60526 (United States).

Kim, H., Kim, H. Y., Song, J. H. & Bae, Y. Y. 2008*a* Heat transfer to supercritical pressure carbon dioxide flowing upward through tubes and a narrow annulus passage. *Progress in Nuclear Energy* **50** (2), 518–525.

Kim, J. & Moin, P. 1985 Application of a fractional-step method to incompressible Navier-Stokes equations. *Journal of computational physics* **59** (2), 308–323.

Kim, J. K., Jeon, H. K. & Lee, J. S. 2007 Wall temperature measurement and heat transfer correlation of turbulent supercritical carbon dioxide flow in vertical circular/non-circular tubes. *Nuclear Engineering and Design* **237** (15), 1795–1802.

Kim, W. S., He, S. & Jackson, J. D. 2008*b* Assessment by comparison with DNS data of turbulence models used in simulations of mixed convection. *International Journal of Heat and Mass Transfer* **51** (5), 1293–1312.

Kirillov, P. 2000 Heat and mass transfer at supercritical parameters. the short review of researches in Russia. Theory and experiments. In *Proceedings of the first international symposium on supercritical water-cooled reactors, design and technology*.

Kline, S. J., Reynolds, W. C., Schraub, F. A. & Runstadler, P. W. 1967 The structure of turbulent boundary layers. *Journal of Fluid Mechanics* **30** (04), 741–773.

Kong, H., Choi, H. & Lee, J. S. 2000 Direct numerical simulation of turbulent thermal boundary layers. *Physics of Fluids (1994-present)* **12** (10), 2555–2568.

Koren, B. 1993 *A robust upwind discretization method for advection, diffusion and source terms*. Centrum voor Wiskunde en Informatica Amsterdam.

Koshizuka, S., Takano, N. & Oka, Y. 1995 Numerical analysis of deterioration phenomena in heat transfer to supercritical water. *International Journal of Heat and Mass Transfer* **38** (16), 3077–3084.

Kunz, O. & Wagner, W. 2012 The GERG-2008 Wide-Range Equation of State for Natural Gases and Other Mixtures: An Expansion of GERG-2004. *Journal of Chemical & Engineering Data* **57** (11), 3032–3091.

Kurganov, V. A. & Kaptilnyi, A. G. 1993 Flow structure and turbulent transport of a supercritical pressure fluid in a vertical heated tube under the conditions of mixed convection. experimental data. *International Journal of Heat and Mass Transfer* **36** (13), 3383–3392.

Kyselỳ, J. 2010 Recent severe heat waves in central europe: how to view them in a long-term prospect? *International Journal of Climatology* **30** (1), 89–109.

Lee, J., Yoon Jung, S., Jin Sung, H. & Zaki, T. A. 2013 Effect of wall heating on turbulent boundary layers with temperature-dependent viscosity. *Journal of Fluid Mechanics* **726**, 196–225.

Lele, S. K. 1994 Compressibility effects on turbulence. *Annual review of fluid mechanics* **26** (1), 211–254.

Lemmon, E. W., Huber, M. L. & McLinden, M. O. 2002 NIST reference fluid thermodynamic and transport properties–refprop.

Li, N. & Laizet, S. 2010 2DECOMP&FFT–a highly scalable 2d decomposition library and FFT interface. In *Cray User Group 2010 conference*, pp. 1–13.

Li, Q., Schlatter, P., Brandt, L. & Henningson, D. S. 2009 DNS of a spatially developing turbulent boundary layer with passive scalar transport. *International Journal of Heat and Fluid Flow* **30** (5), 916–929.

Licht, J., Anderson, M. & Corradini, M. 2008 Heat transfer to water at supercritical pressures in a circular and square annular flow geometry. *International Journal of Heat and Fluid Flow* **29** (1), 156–166.

Licht, J., Anderson, M. & Corradini, M. 2009 Heat transfer and fluid flow characteristics in supercritical pressure water. *Journal of Heat Transfer* **131** (7).

Majda, A. & Sethian, J. 1985 The derivation and numerical solution of the equations for zero mach number combustion. *Combustion Science and Technology* **42**, 185–205.

Mak, P. C.-N. 1988 Thermodynamic properties from cubic equations of state .

Masi, E., Bellan, J., Harstad, K. G. & Okong'o, N. A. 2013 Multi-species turbulent mixing under supercritical-pressure conditions: modelling, direct numerical simulation and analysis revealing species spinodal decomposition. *Journal of Fluid Mechanics* **721**, 578–626.

Mathiesen, B. V., Lund, H., Connolly, D., Wenzel, H., Østergaard, P., Möller, B., Nielsen, S., Ridjan, I., Karnøe, P., Sperling, K. *et al.* 2015 Smart energy systems for coherent 100% renewable energy and transport solutions. *Applied Energy* **145**, 139–154.

Meehl, G. A. & Tebaldi, C. 2004 More intense, more frequent, and longer lasting heat waves in the 21st century. *Science* **305** (5686), 994–997.

Millat, J., Dymond, J. & de Castro, C. N. 1996 *Transport properties of fluids*.

Miropolskii, L. & Shitsman, M. 1957 Heat transfer to water and steam at variable specific heat (in near-critical region). *Soviet Physics-Technical Physics* **2** (10), 2196–2208.

Moin, P. & Kim, J. 1985 The structure of the vorticity field in turbulent channel flow. Part 1. analysis of instantaneous fields and statistical correlations. *Journal of Fluid Mechanics* **155**, 441–464.

Moran, M. J., Shapiro, H. N., Boettner, D. D. & Bailey, M. B. 2010 *Fundamentals of engineering thermodynamics*. John Wiley & Sons.

Morkovin, M. V. 1962 Effects of compressibility on turbulent flows. *Mécanique de la Turbulence* pp. 367–380.

Mosyak, A., Pogrebnyak, E. & Hetsroni, G. 2001 Effect of constant heat flux boundary condition on wall temperature fluctuations. *Journal of heat transfer* **123** (2), 213–218.

Najm, H. N., Wyckoff, P. S. & Knio, O. M. 1998 A semi-implicit numerical scheme for reacting flow: I. stiff chemistry. *Journal of Computational Physics* **143** (2), 381–402.

Nemati, H., Patel, A., Boersma, B. J. & Pecnik, R. 2015 Mean statistics of a heated turbulent pipe flow at supercritical pressure. *International journal of heat and mass transfer* **83**, 741–752.

Ničeno, B. & Sharabi, M. 2013 Large eddy simulation of turbulent heat transfer at supercritical pressures. *Nuclear Engineering and Design* **261**, 44–55.

Nicoud, F. 1998 Numerical study of a channel flow with variable properties. *Center for Turbulent Research, Annual Research Briefs* pp. 289–309.

Nicoud, F. 2000 Conservative high-order finite-difference schemes for low-mach number flows. *Journal of Computational Physics* **158** (1), 71–97.

Nolan, K., Walsh, E. & McEligot, D. 2010 Quadrant analysis of a transitional boundary layer subject to free-stream turbulence. *Journal of Fluid Mechanics* **658**, 310–335.

OECD 2015*a India energy outlook*. www.iea.org.

OECD 2015*b World energy outlook*. www.iea.org.

Onuki, A. 2002 *Phase transition dynamics*. Cambridge University Press.

Perkins, K. & McEligot, D. 1975 Mean temperature profiles in heated laminarizing air flows. *Journal of Heat Transfer* **97**, 589.

Petukhov, B. 1968 Heat transfer in a single-phase medium under supercritical conditions (heat transfer in single phase medium at near critical state parameters). *High Temperature* **6**, 696–709.

Petukhov, B., Krasnoshchekov, E. & Protopopov, V. 1961 An investigation of heat transfer to fluids flowing in pipes under supercritical conditions. *ASME International Developments in Heat Transfer Part* **3**, 569–578.

Petukhov, B. S., Polyakov, A. F. & Launder, B. E. 1988 Heat transfer in turbulent mixed convection. Hemisphere Publishing, New York, NY.

Pioro, I. L., Duffey, R. B. & Dumouchel, T. J. 2004*a* Hydraulic resistance of fluids flowing in channels at supercritical pressures (survey). *Nuclear Engineering and Design* **231** (2), 187–197.

Pioro, I. L., Khartabil, H. F. & Duffey, R. B. 2004*b* Heat transfer to supercritical fluids flowing in channels-empirical correlations (survey). *Nuclear Engineering and Design* **230** (1), 69–91.

Pis'menny, E. N., Razumovskiy, V. G., Maevskiy, E. M., Koloskov, A. E. & Pioro, I. L. 2006 Heat transfer to supercritical water in gaseous state or affected by mixed convection in vertical tubes. *Proceedings of the ICONE14, Miami, USA, July* pp. 17–20.

Pitla, S. S., Robinson, D. M., Groll, E. A. & Ramadhyani, S. 1998 Heat transfer from supercritical carbon dioxide in tube flow: a critical review. *Hvac&R Research* **4** (3), 281–301.

Polyakov, A. F. 1991 Heat transfer under supercritical pressures. *Advances in Heat Transfer* **21**, 1–53.

PROPATH Group 1999 PROPATH: a program package for thermophysical properties of fluids version 11.1.

Rahmstorf, S., Cazenave, A., Church, J. A., Hansen, J. E., Keeling, R. F., Parker, D. E. & Somerville, R. C. 2007 Recent climate observations compared to projections. *Science* **316** (5825), 709–709.

Robinson, S. K. 1991 Coherent motions in the turbulent boundary layer. *Annual Review of Fluid Mechanics* **23** (1), 601–639.

Sawin, J. L., Sverrisson, F., Chawla, K., Lins, C., Adib, R., Hullin, M., Leitner, S., Mazzaccaro, S., Murdock, H., Williamson, L. E. *et al.* 2014 Renewables 2014. Global status report 2014 .

Sharabi, M. & Ambrosini, W. 2009 Discussion of heat transfer phenomena in fluids at supercritical pressure with the aid of CFD models. *Annals of Nuclear Energy* **36** (1), 60–71.

Sharabi, M., Ambrosini, W., He, S. & Jackson, J. D. 2008 Prediction of turbulent convective heat transfer to a fluid at supercritical pressure in square and triangular channels. *Annals of Nuclear Energy* **35** (6), 993–1005.

Shehata, A. M. & McEligot, D. M. 1998 Mean structure in the viscous layer of strongly-heated internal gas flows. measurements. *International journal of heat and mass transfer* **41** (24), 4297–4313.

Shen, B. & Zhang, P. 2013 An overview of heat transfer near the liquid–gas critical point under the influence of the piston effect: Phenomena and theory. *International Journal of Thermal Sciences* **71**, 1–19.

Shepherd, A., Ivins, E. R., Geruo, A., Barletta, V. R., Bentley, M. J., Bettadpur, S., Briggs, K. H., Bromwich, D. H., Forsberg, R., Galin, N. *et al.* 2012 A reconciled estimate of ice-sheet mass balance. *Science* **338** (6111), 1183–1189.

Shitsman, M. E. 1963 Impairment of the heat transmission at supercritical pressures (heat transfer process examined during forced motion of water at supercritical pressures). *High Temperature* **1**, 237–244.

Smith Jr, R., Inomata, H. & Peters, C. 2013 *Introduction to Supercritical Fluids: A Spreadsheet-based Approach*. Newnes.

Soave, G. 1972 Equilibrium constants from a modified Redlich-Kwong equation of state. *Chemical Engineering Science* **27** (6), 1197–1203.

Song, J. H., Kim, H. Y., Kim, H. & Bae, Y. Y. 2008 Heat transfer characteristics of a supercritical fluid flow in a vertical pipe. *The Journal of Supercritical Fluids* **44** (2), 164–171.

Span, R. 2000 *Multiparameter equations of state: an accurate source of thermodynamic property data*. Springer Science & Business Media.

SPAN, R. & WAGNER, W. 2003*a* Equations of state for technical applications. I. Simultaneously optimized functional forms for nonpolar and polar fluids. *International Journal of Thermophysics* **24**, 287–342.

SPAN, R. & WAGNER, W. 2003*b* Equations of state for technical applications. II. Results for nonpolar fluids. *International Journal of Thermophysics* **24**, 41–109.

STOKES, G. G. 1849 On the theories of the internal friction of fluids in motion and of the equilibrium and motion of elastic solids. *Trans. Cambridge. Philos. Soc.* **8** (22), 287–342.

SWENSON, H., CARVER, J. & KAKARALA, C. D. 1965 Heat transfer to supercritical water in smooth-bore tubes. *Journal of Heat Transfer* **87** (4), 477–483.

TABOR, G. & BABA-AHMADI, M. 2010 Inlet conditions for large eddy simulation: a review. *Computers & Fluids* **39** (4), 553–567.

TASKINOGLU, E. S. & BELLAN, J. 2010 A posteriori study using a dns database describing fluid disintegration and binary-species mixing under supercritical pressure: heptane and nitrogen. *Journal of Fluid Mechanics* **645**, 211–254.

TENNEKES, H. & LUMLEY, J. 1972 *A first course in turbulence*. The MIT press.

TISELJ, I., BERGANT, R., MAVKO, B., BAJSIC, I. & HETSRONI, G. 2001*a* DNS of turbulent heat transfer in channel flow with heat conduction in the solid wall. *Journal of heat transfer* **123** (5), 849–857.

TISELJ, I., POGREBNYAK, E., LI, C., MOSYAK, A. & HETSRONI, G. 2001*b* Effect of wall boundary condition on scalar transfer in a fully developed turbulent flume. *Physics of Fluids (1994-present)* **13** (4), 1028–1039.

VERZICCO, R. & SREENIVASAN, K. 2008 A comparison of turbulent thermal convection between conditions of constant temperature and constant heat flux. *Journal of fluid mechanics* **595**, 203–219.

VESOVIC, V., WAKEHAM, W., OLCHOWY, G., SENGERS, J., WATSON, J. & MILLAT, J. 1990 The transport properties of carbon dioxide. *Journal of Physical and Chemical Reference Data* **19** (3), 763–808.

WALLACE, J. M., ECKELMANN, H. & BRODKEY, R. S. 1972 The wall region in turbulent shear flow. *Journal of Fluid Mechanics* **54** (1), 39–48.

WEN, Q. L. & GU, H. Y. 2010 Numerical simulation of heat transfer deterioration phenomenon in supercritical water through vertical tube. *Annals of Nuclear Energy* **37** (10), 1272–1280.

WILLMARTH, W. & LU, S. 1972 Structure of the Reynolds stress near the wall. *Journal of Fluid Mechanics* **55** (01), 65–92.

Wu, X. & Moin, P. 2008 A direct numerical simulation study on the mean velocity characteristics in turbulent pipe flow. *Journal of Fluid Mechanics* **608**, 81–112.

Yamagata, K., Nishikawa, K., Hasegawa, S., Fujii, T. & Yoshida, S. 1972 Forced convective heat transfer to supercritical water flowing in tubes. *International Journal of Heat and Mass Transfer* **15** (12), 2575–2593.

Yoo, J. Y. 2013 The turbulent flows of supercritical fluids with heat transfer. *Annual Review of Fluid Mechanics* **45**, 495–525.

Zeinali, H., Toma, P. & Kuru, E. 2012 Effect of near-wall turbulence on selective removal of particles from sand beds deposited in pipelines. *Journal of Energy Resources Technology* **134** (2), 021003.

Zhang, G., Zhang, H., Gu, H., Yang, Y. & Cheng, X. 2012 Experimental and numerical investigation of turbulent convective heat transfer deterioration of supercritical water in vertical tube. *Nuclear Engineering and Design* **248**, 226–237.

Zhang, X., Yamaguchi, H., Fujima, K., Enomoto, M. & Sawada, N. 2006 Study of solar energy powered transcritical cycle using supercritical carbon dioxide. *International Journal of Energy Research* **30** (14), 1117–1129.

Zhang, X., Yamaguchi, H., Fujima, K., Enomoto, M. & Sawada, N. 2007*a* Theoretical analysis of a thermodynamic cycle for power and heat production using supercritical carbon dioxide. *Energy* **32** (4), 591–599.

Zhang, X.-R., Yamaguchi, H. & Uneno, D. 2007*b* Experimental study on the performance of solar Rankine system using supercritical CO_2. *Renewable Energy* **32** (15), 2617–2628.

Zonta, F., Marchioli, C. & Soldati, A. 2012 Modulation of turbulence in forced convection by temperature-dependent viscosity. *Journal of Fluid Mechanics* **697**, 150–174.

Acknowledgments

First and foremost I would like to express my special appreciation and thanks to my daily supervisor *Dipl.-Ing. Dr.techn. R. Pecnik.* He provided me with every bit of guidance, assistance and expertise that I needed during my PhD. I appreciate all his contributions to my research and for allowing me to grow as a research scientist.

I am very grateful to *Prof. dr. ir. B.J. Boersma*, my promoter, for all his help, advice, encouragement and kindness. The thesis would not have come to a successful completion, without the help that I received from him. Wherever I am, I will always admire him as a person and will also remember his contribution to my work.

I also want to thank my dissertation committee, *Prof. Dr.-Ing. S. Hickel*, *Prof. Dr.-Ing. E. Laurien*, *Prof. dr. D.J.E.M. Roekaerts*, *Prof. dr. ir. T.H. van der Meer* and *Dr. ir. J.A. van Oijen* for their academic support, inputs and personal encouragement.

To my friends, thank you for listening, offering me advice, and supporting me through the entire of this journey. To my friends scattered around the world, thank you for your well-wishes, phone calls, emails, texts and visits. My greatest gratitude goes to my friends *Marloes Anne Reus*, *Jurriaan Peeters* and *Uttiya Sengupta* who patiently helped me in writing and revising some part of this thesis.

I would also like to acknowledge that the simulations in this thesis were carried out on the PRACE research infrastructure resources and Dutch national e-infrastructure with the support of SURF Cooperative.

I am deeply thankful to my family for their love, support and patience. I dedicate this thesis to the memory of my father *Alireza*, who was and is my hero and whose role in my life was, and remains immense. I have saved the last words of acknowledgement for my dear wife *Ameneh*, who has been with me all these years and has made them the best years of my life. Her support and encouragement was in the end what made this thesis possible.

List of publications

Journal papers

Nemati, H., Patel, A., Boersma, B.J., Pecnik, R., 2015. "Mean statistics of a heated turbulent pipe flow at supercritical pressure". *International Journal of Heat and Mass Transfer*, **83**, pp. 741–752.

Gallo, M., Nemati, H., Boersma, B.J., Pecnik, R., Attrotto, P., Colonna, P., 2015. "Magnetic-ribs in fully developed laminar liquid–metal channel flow". *International Journal of Heat and Fluid Flow*, **56**, pp. 198–208.

Nemati, H., Patel, A., Boersma, B.J., Pecnik, R., 2016. "The effect of thermal boundary conditions on forced convection heat transfer to fluids at supercritical pressure". *Journal of Fluid Mechanics*, **800**, pp. 531–556.

Conference papers

Nemati, H., Patel, A., Boersma, B.J., Pecnik, R., 2013. "Direct numerical simulation of a turbulent flow with a supercritical fluid in a heated pipe". *Proceedings of the 8rd International Symposium on Turbulence and Shear Flow Phenomena*, Poitiers - France.

Nemati, H., Patel, A., Boersma, B.J., Pecnik, R., 2013. "The effects of thermal boundary condition on turbulent statistics in flow with supercritical CO_2". *Proceedings of the 8rd International Symposium on Turbulence and Shear Flow Phenomena*, Limassol - Cyprus.

About the author

Hassan Nemati was born in Bojnord, Iran, on March, 21st, 1985.

After qualifying the national examinations, known as "Konkoor", he started his Bachelor studies in Shahrood University of Technology in 2003. He completed his undergraduate program in Mechanical Engineering and successfully graduated in 2007 with the cumulative GPA of 16.65/20. He achieved the 2nd rank among 50 students.

Passing through another Konkoor in 2007, he was admitted to University of Mazandaran. He carried out a Master project titled "*Numerical simulation of heat transfer and fluid flow past rotating cylinders using the Lattice Boltzmann Method*", and in April 2010 he received his MSc degree. He achieved a cumulative GPA of 18.29/20 in M.Sc. studies that placed him as first ranked among 80 students of Mechanical Engineering faculty. During his master study, he had the chance to have extracurricular research on nanofluid and magnetohydrodynamics. During this time he published 5 papers in highly-ranked international peer-reviewed scientific journals.

The master level was a great stimulus in his will to pursue a graduate program at a doctorate level. In March 2012, he moved to Delft, The Netherlands, to start an exciting 4-year journey at the Process & Energy department of the Delft University of Technology under the supervision of *Dipl.-Ing. Dr.techn. R. Pecnik* and *Prof. dr. ir. B.J. Boersma*. For the PhD project, Hassan studied the effect of large thermophysical property variations on turbulent heat transfer with fluids at supercritical pressures using direct numerical simulation. He presented his results at several international conferences and published his work in the International Journal of Heat and Mass Transfer, International Journal of Heat and Fluid Flow, and Journal of Fluid Mechanics.